UNIVERSIDADE DE LISBOA
FACULDADE DE CIÊNCIAS
DEPARTAMENTO DE FÍSICA


# Design and testing of a rear wing for a Formula Student car

João Pedro Luís Morgado

**Mestrado Integrado em Engenharia Física**

Dissertação orientada por:
Prof. Dr. Luís Rego da Cunha Eça
Prof. Dr. Manuel Adler Sanchez de Abreu

2022

## Acknowledgments

During my academic life I had help of a countless number of people whom this work would probably be impossible without, this small section will be used to express my gratitude to them.

Firstly, I would like to thank professor Guiomar Evans for the general guidance she gave and the dedication she has to her students. I also owe a huge amount of gratitude to professors André Marta, Luís Eça and Manuel Abreu for their guidance as my advisors as their insight and analysis was one of the major factors behind the successful accomplishment of this project.

To my colleagues at FST Lisboa, I am extremely grateful for giving me the resources I needed to make this work possible. I would specifically like to thank Diana Sanchez for her help with 3D printing the parts I needed and Rúben Alves for his contribution in some of the wind tunnel measurements and its calibration. Of course I cannot forget the help, motivation and unforgettable moments given to me by the members of the FST10e and FST11 aerodynamic department José Luciano, João Perdigão, Gonçalo Biltes, Luís Afonso, Francisco Vital, Carlos Monteiro, Diogo Jerónimo, Paulo Clemente, João Ferreira, Diogo Viegas, Filipa Nunes and Alexandre Trindade. A special thanks also goes to Miguel Carreira and Jaime Pacheco as this thesis follows much of the ground work that they made. This year gave us a taste of success in Formula Student with various overall podiums and wins which would not have been possible without the remarkable effort put in by the team, I hope these were just the first ones.

I would also like to mention my friends Rui Parreira, Romeu Abreu, André Sistelo and Diogo Sucena for their support during these years.

To my girlfriend, Matilde Santos, there is not enough space to express everything you have done for me. So I will keep it short and say thank you for everything and I love you.

Lastly, to my mother, father and grandmother, thank you for always supporting me and allowing me to have this opportunity, as without you, none of this would have been possible.

## Abstract

Formula Student teams go to extreme lengths to develop their aerodynamic packages, as it is a key factor to enhance car performance. The yearly objectives for the aerodynamic department are usually supplied by the vehicle dynamics department through lap time simulations. However, these usually are not capable of relating car attitude to aerodynamic performance and do not assume any relation between the aerodynamic coefficients.

A simple aerodynamic model relating the lift coefficient to the drag coefficient and mass was added to the point mass simulator from the FST Lisboa vehicle dynamics department, to estimate the ideal aerodynamic coefficients and maximize vehicle performance for the current car design.

By applying the results from the upgraded point mass simulator, a maximum theoretical lift, drag and mass were obtained. Through these results, a new rear wing concept, based on using airfoils as endplates was adopted, in order to create a design that would suit the new aerodynamic targets. Initially a low drag design was tested, however, preliminary results showed that due to high car mass it was not a viable design choice to follow. The final choice was to develop a high downforce rear wing.

The resulting design was then validated using IST's aeroacoustic wind tunnel, to assess its on-track performance. During this test, the aerodynamic forces applied on the whole vehicle were measured. A qualitative analysis of the results showed that the numerical simulations captured the experimental trends. Wool tufts were used as a flow visualization technique, these showed some discrepancies between the CFD simulations and experimental results, which were attributed to the simplifications made in both the numerical and experimental models.

The implementation of the new aerodynamic model proved effective, as a design which yielded increase performance was obtained. Correlation between the CFD and on-track results is still limited due to modelling limitations in both experimental and numerical domains.



**Keywords:** Formula Student, Aerodynamic performance, CFD, Wind tunnel, Validation

# Resumo

O desenvolvimento de um pacote aerodinâmico de alto desempenho é um dos maiores focos das equipas de Formula Student. Este é utilizado para gerar maior carga vertical, sustentação, que por sua vez permite ao carro atingir velocidades superiores em curva, diminuindo os tempos por volta. De modo a escolher qual a configuração aerodinâmica ideal, as equipas recorrem a simuladores de corrida, normalmente criados pelo seu departamento de dinâmica de veículo. Contudo, apesar de extremamente complexos, a maior parte destes simuladores não relaciona o desempenho aerodinâmico com a variação da atitude do carro durante uma volta, nem assume nenhuma relação entre os coeficientes aerodinâmicos.

Este trabalho tem como intuito adicionar a relação entre resistência e sustentação ao simulador de massa pontual criado pelo departamento de dinâmica de veículo da equipa de Formula Student da ULisboa, a FST Lisboa. Para além desta relação, uma relação empírica entre massa do pacote aerodinâmico e coeficiente de sustentação do mesmo também foi criada, de modo a se obter um teto para os valores de coeficiente de sustentação, coeficiente de arrasto e massa que um pacote aerodinâmico pode ter para não afetar o desempenho do veículo. O veículo em questão para este estudo foi o FST10e, o segundo protótipo elétrico mais recente da equipa de Lisboa. Não foram utilizado os resultados do protótipo mais recente, pois este ainda se encontrava em construção durante o desenvolvimento deste trabalho.

Para criar a relação entre os coeficientes aerodinâmicos e a massa, utilizaram-se resultados numéricos existentes de dois protótipos da FST Lisboa, o FST10e e o FST09e. Baseado nestes resultados utilizou-se uma polar para estimar a dependência do arrasto no aumento da sustentação. Foi utilizada uma relação quadrática entre os dois coeficientes. A relação da massa com sustentação foi feita através do cálculo do quociente entre a massa e o valor do coeficiente de sustentação do FST10e combinada com a relação entre área e coeficiente de sustentação dos pacotes aerodinâmicos dos dois veículos.

Foi realizado um curto estudo à convergência do simulador de massa pontual de forma a reduzir o erro numérico que provém deste. Seguidamente a este estudo, estimou-se qual seria a diferença de pontuação esperada entre cada um dos casos simulados com a nova relação entre os parâmetros do pacote aerodinâmico e o FST10e. Chegou-se a um teto máximo de $-C_L A = 5.75$ $m^2$, $C_D A = 2.73$ $m^2$ e $m = 32.58$ $kg$ e verificou-se que o parâmetro aerodinâmico dominante no desempenho do veículo é o coeficiente de sustentação.

De forma a avaliar a veracidade destes resultados, desenvolveu-se uma nova asa traseira cujo desempenho fosse de acordo com os resultados dados pelo simulador. Esta asa teria como foco de desenvolvimento, placas finais com formato de perfil aerodinâmico, de forma a maximizar a sustentação em curva. Inicialmente foi testado um conceito de baixo arrasto, contudo os seus resultados não foram positivos devido à alta massa do veículo, $233kg$. Este conceito apenas deve voltar a ser considerado para uma massa do veículo muito inferior, pois apenas nessas condições as perdas causadas pela resistência aerodinâmica são significativas. Seguiu-se então para um conceito de alta sustentação, de forma a maximizar o desempenho deste componente.

Para maximizar a sustentação foram escolhidas três principais frentes de desenvolvimento: o formato das placas finais, como mencionado anteriormente; a mudança para um elemento principal da asa curvo, de modo a desviar a esteira do piloto da cascata; aumento do tamanho das placas finais, de forma melhor isolar a zona de baixa pressão gerada pelos aerofólios. Foram executadas várias simulações com configurações diferentes da asa com o intuito de otimizar

cada um dos parâmetros, convergindo para um *design* final que maximizasse a sustentação. Foram alterados parâmetros tais como corda, espaçamento vertical e horizontal entre os vários elementos e ângulo de ataque de modo a permitir o alcance deste objetivo.

Deste processo de *design*, obteve-se uma nova asa traseira que gera mais 20% de sustentação do que o caso base, aumentando assim a força vertical total gerada pelo pacote aerodinâmico em 8%. Verificou-se ainda um aumento de 16% no arrasto do veículo. Foi ainda possível de observar através dos resultados numéricos que com esta asa as perdas de sustentação verificadas em curva eram reduzidas. Estima-se, através do simulador de corrida, que esta nova configuração do veículo cause um aumento de 6 pontos na classificação final de uma competição de Formula Student.

De modo a validar o desempenho desta nova configuração do carro, recorreu-se ao túnel aeroacústico presente no laboratório de Engenharia Aeroespacial do Instituto Superior Técnico. Para executar este estudo foi utilizado um modelo á escala de 1/3 do FST10e, previamente construído. Colocou-se no túnel de vento uma balança aerodinâmica de 6 braços, de modo a permitir a medição dos vários coeficientes aerodinâmicos: $C_LA$, $C_DA$, $CY_A$, $CM_X$, $CM_Y$, $CM_Z$. Antes das medições, executou-se um processo de calibração da balança através de pesos conhecidos, de forma a reduzir a incerteza nas medições feitas com a balança.

Obtiveram-se resultados dos coeficientes aerodinâmicos para o FST10e na sua configuração base e com a nova asa traseira. De modo a simular condições em curva estas foram feitas a vários ângulos de guinada, entre 0° e 10°. Verificou-se que os resultados numéricos capturavam corretamente as tendências experimentais em quase todos as grandezas, existindo apenas alguns padrões erráticos nas medições do $CM_Z$ e $CM_X$ na configuração base do veículo. Estas inconsistências foram atribuídas a possíveis falhas na calibração ou posicionamento do veículo sobre a balança. Não foi possível comparar estes resultados com as estimativas numéricas da configuração em pista, devido a limitações de modelação tanto numéricas como experimentais.

Foram ainda colocados fios de lã nas superfícies da nova asa para tentar identificar zonas de separação e possíveis incongruências entre os resultados numéricos e experimentais. Na cascata não se verificaram diferenças significativas, contudo nas placas finais verificou-se uma zona de separação muito maior do que a esperada na sua zona exterior. Esta diferença muito provavelmente advém da maior intensidade de turbulência que é verificada no jato do túnel de vento e difícil de replicar nos resultados numéricos devido á sua dissipação. Este método provou-se inconclusivo a analisar os suportes da asa tal como a zona interior das placas finais devido há existência de zonas de separação ou transversais ou tridimensionais, que os fios de lã não permitem observar.

Através destes resultados conclui-se que as modificações feitas ao simulador de massa pontual foram bem sucedidas. A nova configuração da asa trouxe mais desempenho ao carro, subindo a pontuação esperada nas competições de Formula Student. Contudo, é ainda necessário um simulador mais complexo de modo a realmente se conseguir identificar melhor as fraquezas do pacote aerodinâmico em várias atitudes do carro de modo a corrigi-las. Verificou-se a mesma tendência entre os resultados numéricos e experimentais no túnel de vento, contudo ainda é necessário melhorar a sua modelação. No caso experimental, deveria-se tentar colocar um tapete rolante e rodas a rodar de modo a melhor simular o movimento do carro, pois esta mudança nas condições de fronteira traz alterações significativas no escoamento à volta do veículo. Para se obterem melhores resultados no regime numérico é necessária uma malha mais fina de modo a capturar detalhes do escoamento com maior exatidão. Com estas mudanças nos métodos de

estudo utilizados pela FST Lisboa será possível obter uma melhor correlação entre os resultados obtidos em pista e numéricos.

**Palavras-chave:** Formula Student, Performance Aerodinâmica, CFD, Túnel de Vento, Validação

# Contents

# List of Tables

# List of Figures

# List of Abbreviations

**AoA** Angle of Attack

**CAD** Computer Aided Design

**CFD** Computational Fluid Dynamics

**DRS** Drag Reduction System

**EFD** Experimental Fluid Dynamics

**FRH** Front ride height

**FS** Formula Student

**FSG** Formula Student Germany

**IST** Instituto Superior Técnico

**LES** Large Eddy Simulations

**QSS** Quasi-Steady-State

**RANS** Reynolds-Averaged Navier-Stokes

**RRH** Rear ride height

# Nomenclature

**Greek symbols**

| | |
|---|---|
| $\alpha$ | Angle of attack (°) |
| $\eta$ | Dynamic viscosity (Pa s) |
| $\mu$ | Adhesion coefficient |
| $\rho$ | Density (kg m$^{-3}$) |
| $\tau$ | Torque (N m) |

**Roman symbols**

| | |
|---|---|
| $A$ | Area (m$^2$) |
| $a$ | Acceleration (m s$^{-2}$) |
| $C_D$ | Coefficient of drag |
| $C_f$ | Coefficient of friction |
| $C_L$ | Coefficient of lift |
| $C_M$ | Coefficient of moment |
| $C_Y$ | Coefficient of lateral force |
| $df_{ft}$ | Front downforce distribution |
| $df_{rr}$ | Rear downforce distribution |
| $F$ | Force (N) |
| $g$ | Gravitational acceleration (m s$^{-2}$) |
| $h$ | Height (m) |
| $M$ | Mass (kg) |
| $M_{eq}$ | Equivalent mass (kg) |
| $N$ | Normal force (N) |
| $p$ | Pressure (Pa) |

| | |
|---|---|
| $r$ | Radius (m) |
| $Re$ | Reynolds Number |
| $t$ | Time (s) |
| $v$ | Velocity (m $s^{-1}$) |
| $W$ | Weight (N) |
| $w_{ft}$ | Front weight distribution |
| $w_{lr}$ | Left weight distribution |
| $w_{rr}$ | Rear weight distribution |
| $w_{rt}$ | Right weight distribution |
| $WB$ | Vehicle wheelbase (m) |

**Subscripts**

| | |
|---|---|
| $CoG$ | Center of Gravity |
| $i$ | Time step |
| $x, y, z$ | Cartesian components |

# Chapter 1

# Introduction

The first chapter of this thesis intends to give a brief summary of the reasoning behind this work, as well as its intended results.

## 1.1 Impact of aerodynamics on car performance

Since the automotive industry has started producing faster and faster vehicles, aerodynamics have become an extremely important role in its growth and development. Vehicle geometries are usually complex, which means that the airflow surrounding it has three-dimensional characteristics, leading to turbulent boundary layers due to the creation of strong pressure gradients. Separation zones and large wake regions are also commonly observed. These factors combined lead to high drag coefficients, $C_D$. High amounts of drag can severely impair the vehicle's mobility, as acceleration, top speed, stability and fuel efficiency will suffer negatively. As such, the study and optimisation of a road vehicle's $C_D$ has played a critical role in its design, especially since the 1980's as seen in Fig. 1.1.

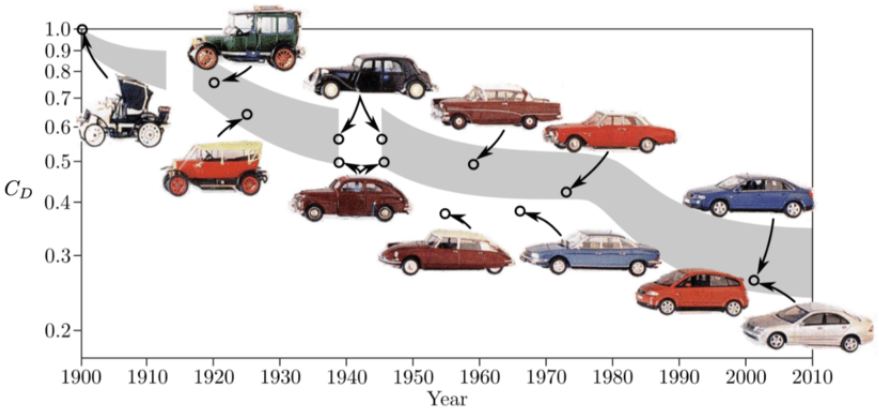


Figure 1.1: Evolution of the drag coefficient of road vehicles [1].

However, when considering race car performance, the $C_D$ value is not the most influential aerodynamic parameter. Instead, this type of vehicle is focused on generating downforce, negative lift, and, as such, their lift coefficient, $C_L$, value is critical. This paradigm change happens due to the ability of downforce to increase a vehicle's cornering capabilities by increasing the load on the tyres, which leads to a sharp decrease in lap times, as demonstrated in Fig. 1.2.

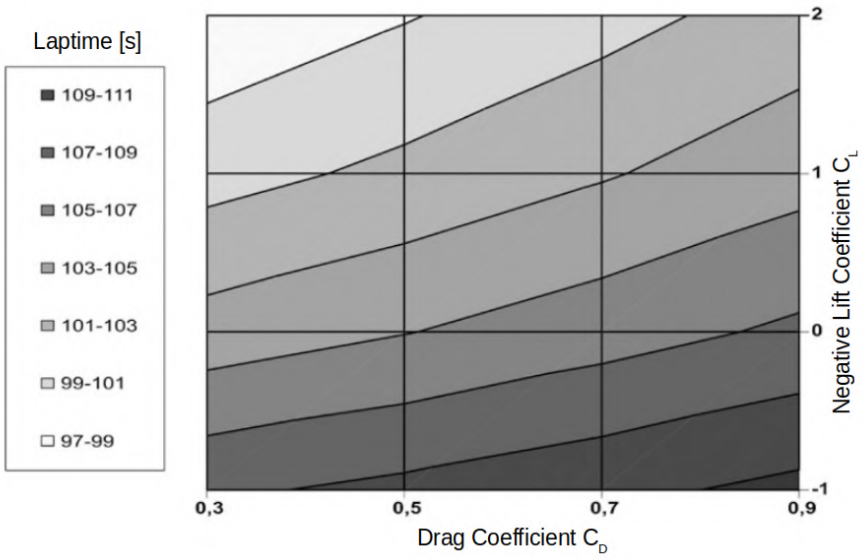


Figure 1.2: Relationship between laptime, $C_L$ and $C_D$ of a generic race car around the Hockenheimring [2].

## 1.2 Formula Student

Formula Student is an international engineering competition in which university students are tasked with the concept, design and development of a formula type racecar. On each competition, the cars take part in two event categories:

- Static Events - where the operational and engineering aspects are evaluated. These events are divided into three disciplines:
  - Business Plan Presentation - where the teams present their vehicle as if it was a product that they wanted to bring to market, focusing on its sale and profitability;
  - Cost and Manufacturing - where the team's understanding of the manufacturing processes and the costs associated with the development of a prototype are evaluated;
  - Engineering Design - where the design and engineering processes behind the development of the car are assessed.
- Dynamic Events - where the vehicle's on-track performance is assessed. There are five of these events:
  - Acceleration - a 75 $m$ straight line sprint where longitudinal acceleration is of utmost importance;
  - Skidpad - a timed lap of an 8-shaped track, where the vehicle's lateral acceleration is tested;
  - Autocross - a 1 $km$ sprint intended to test all of the car's peak dynamic capabilities;
  - Endurance - the main event, where the reliability and performance of the vehicle are put to test over a 22 $km$ distance.
  - Efficiency - the fuel or energy consumption of the vehicle during the Endurance event is measured to evaluate the relation between performance and fuel/energy economy.

Each event awards the team points, which are calculated based on the team's score and the best score, according to Tab. 1.1.

Table 1.1: Maximum points awarded at a Formula Student competition.

| **Static events** | Points |
|---|---|
| Business plan presentation | 75 |
| Cost and manufacturing | 100 |
| Engineering design | 150 |
| **Dynamic events** | |
| Acceleration | 75 |
| Skidpad | 75 |
| Autocross | 100 |
| Endurance | 325 |
| Efficiency | 100 |
| **Total** | 1000 |

Even though the speeds achieved in a Formula Student competition are low due to sinuous track layouts, with small radii corners, slaloms, short straights and hairpins, these are still high enough so that aerodynamic forces play a major role in the vehicle's performance [3].

As mentioned in Sec. 1.1, a Formula Student race car aerodynamic performance is mostly influenced by its lift coefficient. Teams develop highly complex aerodynamic packages consisting of multi-element front and rear wings, undertrays, diffusers and side-mounted wings, as illustrated in Fig. 1.3. The wing size is, however, limited by design boxes imposed by the regulation's chapter T8 [4], which are shown in Fig. 1.4. This leads to short wingspans compared to the total wing chord, generating low aspect ratio and thus creating a large drag coefficient.


(a) FST Lisboa (Lisbon, Portugal) ©FSG - Mosch

(b) Ecurie Aix (Germany, Aachen) [5]

Figure 1.3: Example of some Formula Student cars with their aerodynamic packages installed.

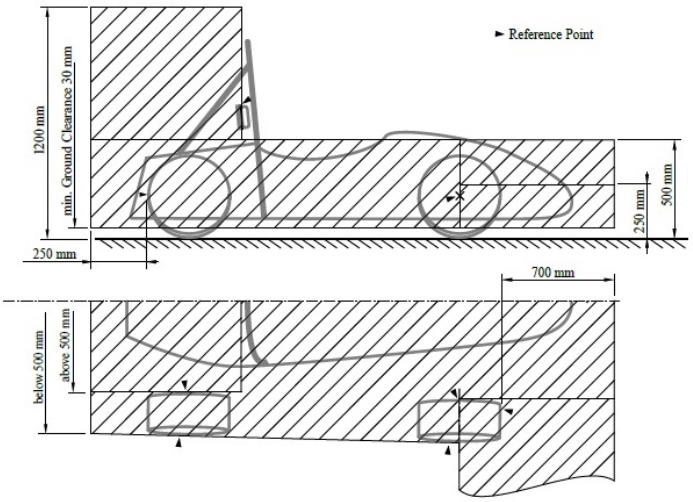


Figure 1.4: Design boxes imposed on aerodynamic devices [4].

## 1.3 Motivation

Currently at FST Lisboa, the yearly objectives for the aerodynamics department are supplied by the vehicle dynamics department through their lap time simulator. These simulations consider that the vehicle is a single point mass moving through a prescribed track layout. The simulation parameters are static and do not vary with the vehicle attitude or whichever track portion is being simulated. Even though this simulator is a powerful tool, some of these approximations are too simplistic, such being the case of the aerodynamic parameters, $C_L$ and $C_D$, as they are considered completely independent of each other. This simplification is obviously nonsensical as $C_L$ generates induced drag $C_{Di}$, which makes these coefficients highly dependent on each other. There is also no relation between the aerodynamic parameters and vehicle mass, which further worsens the ability to define proper objectives.

Due to the lack of these dependencies, the model currently estimates that as the $C_L$ increases the car's performance will always increase, as seen in Fig. 1.5 where Formula Student's Germany 2019 autocross track was simulated.

By creating more complex models that better describe the relation between the aerodynamic parameters, mass and general vehicle behaviour, vehicle objectives can be better defined. With clearer objectives, the aerodynamic development process can be much faster and more streamlined. Furthermore, these models could also be introduced in more complex simulators to increase the quality of the obtained data using the analysis tools developed by the team.

## 1.4 Objectives and deliverables

This thesis intends to build on the results obtained from previous work [6], higher aerodynamic efficiency values could be obtained, by correctly using the vortices created by the rear wing endplates, an example of a wind tunnel tested design is shown in Fig. 1.6. By using the additional suction effect provided by the wingtip vortices, more downforce can be generated through the wing cascade, allowing the use of simpler designs with less flaps, which reduces drag.

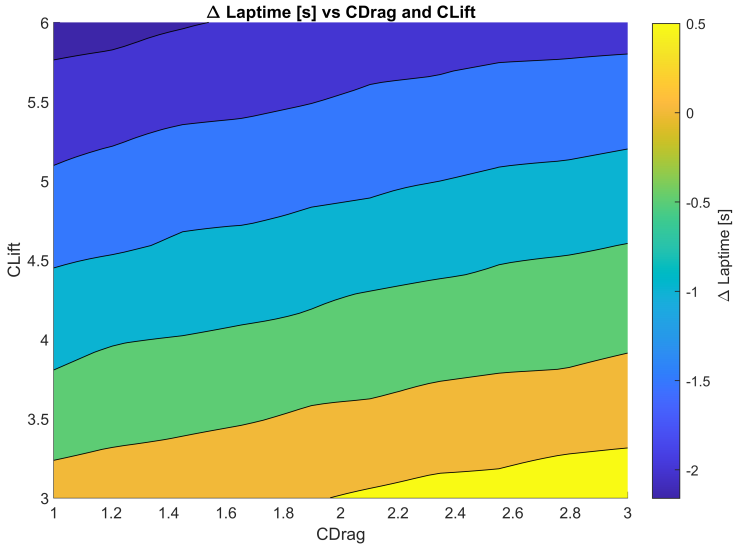


Figure 1.5: Example of results of a point mass simulation executed by the vehicle dynamics department of FST Lisboa.

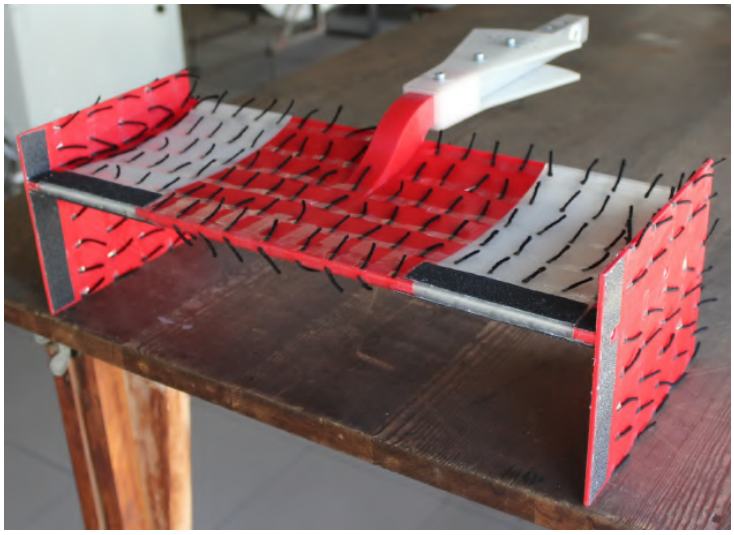

Figure 1.6: 3D printed model of a rear wing design studied in [6].

A more realistic aerodynamic model will be implemented into the currently existing point mass simulator to allow a better definition of aerodynamic targets. This model relates the $C_L$, $C_D$ and aerodynamic package mass to allow the prediction of an optimal aerodynamic kit for the current car design.

By combining these two development fronts, it is expected that this work will deliver a new rear wing, which better suits the revised aerodynamic targets and the car concept.

## 1.5 Thesis outline

This thesis is divided into seven chapters.

**Chapter One** introduces the work, as well as its objectives and deliverables.

**Chapter Two** contains the theoretical background behind the aerodynamics of formula vehicles, as well as an explanation of the tools used to study aerodynamics in the industry and

the FST Lisboa team.

**Chapter Three** refers to the point mass simulator, its design and capabilities and the modifications made to implement an aerodynamic model.

In **Chapter Four** the base design of the FST10e is analysed as well as its shortcomings, having a greater focus on its rear wing design.

**Chapter Five** illustrates the design process and decisions behind the new rear wing geometry.

**Chapter Six** presents the wind tunnel testing campaign of the new rear wind design, as well as its results.

**Chapter Seven** concludes the work by presenting its achievements, alongside some suggestions for future work based on the obtained results.

# Chapter 2

# Aerodynamics of Formula vehicles

This section elaborates on some of the concepts mentioned in this thesis, as well as some previous work already made in this development area.

## 2.1 Impact of aerodynamics in race car performance

### 2.1.1 Tyre performance

The forces [7] necessary to drive a car are generated by the contact patch between the tyres and the road. In order to generate these forces, the tyres must deform, which leads to slip, the difference between the velocity of the road and the tyre. These forces are highly dependent on the ratio between the applied vertical load $F_z$ and a force parallel to the ground $F_\xi$, named the adhesion coefficient $\mu$,

$$\mu = \frac{F_\xi}{F_z}. \tag{2.1}$$

If the $\xi$ direction is aligned with the longitudinal axis of the vehicle then $\xi = x$ and $\mu$ is called the braking coefficient, whereas if it is perpendicular, then $\xi = y$ and $\mu$ is called the cornering coefficient or lateral adhesion. As seen in fig 2.1(a), in the braking coefficient (a), the wheel slip is defined as a percentage, while in the cornering coefficient (b) it is defined by the slip angle $\beta$.

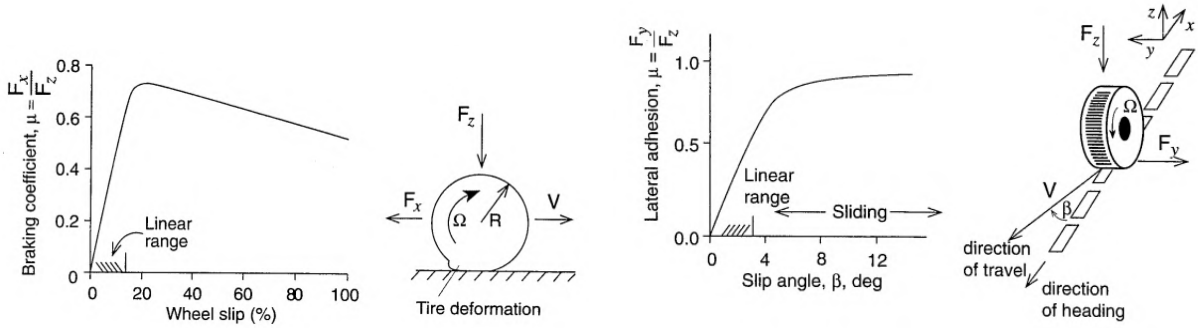


(a) Braking coefficient

(b) Cornering coefficient

Figure 2.1: Adhesion coefficient as a function of slip for braking and cornering cases [7].

From this definition of the adhesion coefficient, it is shown that, for a larger vertical load, the same horizontal force can be generated at a lower slip angle. This means that by increasing

the normal load on the tyres, the lateral forces generated by them will also be increased, which leads to greater cornering speeds. Furthermore, this increase in vertical load allows a greater braking force to be applied, which also leads to faster lap times as the vehicle does not have to spend as much time reducing its speed before corners.

These definitions allow the establishment of a concept called the tyre performance envelope, which defines the maximum acceleration a tyre with a certain applied vertical load allows in each direction without sliding, as illustrated in Fig. 2.2.

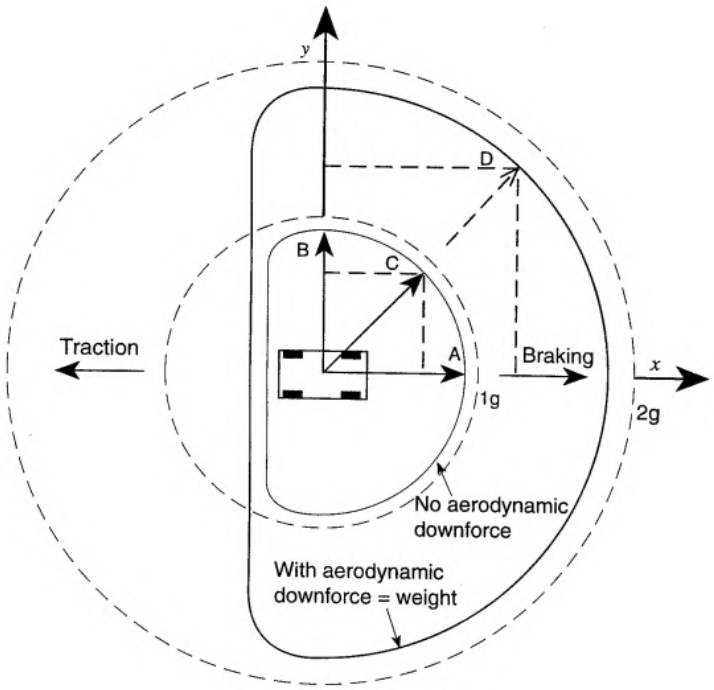


Figure 2.2: Polar representation of a tyre's performance envelope [7].

There are two main methods of creating additional vertical forces on a vehicle. The first one is to add weight. This method, however simple, is highly inefficient as a vehicle with more mass requires more energy to both accelerate and turn, reducing its top speed and cornering capabilities. The second method is to generate downforce with aerodynamic components. This is a much more desirable mean as it produces higher vertical loads while not adding a significant amount of weight to the vehicle. The effect of adding downforce can be seen in Fig. 2.2, where a car with an aerodynamic package has much higher cornering, braking and tractive capabilities.

### 2.1.2 Vehicle dynamics

Even though, as aforementioned, tyres create the driving forces of the vehicle, it is how these forces impact the vehicle that matters the most. A balance of these loads is necessary to preserve vehicle control and stability in any driving condition. Taking cornering as an example: if the vehicle turns less than intended by the turning angle (Ackermann angle) it has an understeer. If the opposite happens, it has an oversteer. Shown in Fig. 2.3 are how these behaviours impact a car's trajectory through a constant radius corner [7].

In order to avoid both these phenomena the load applied on each tyre has to be the same to guarantee that each tyre has the same side slip angle. However, due to vehicle mass distributions

and aerodynamic downforce, this rarely happens. If a vehicle has a higher load on the front tyres than the rear tyres, it will lead to oversteer, since the front will rotate more, causing the rear tyres to slide. The opposite also applies, an understeer is created if the load on the rear tyres is higher, leading to a front slide. In order to strike a balance between oversteer and understeer, there are two main methods: tweaking the suspension setup and modifying the aerodynamic load distribution on the vehicle (aerodynamic balance) [8].

Aerodynamic balance is one of the most important parameters to take into account while developing an aerodynamic package as it will heavily define vehicle behaviour through corners. There is no consensus in what is the correct aerodynamic balance or if understeer or oversteer is better as this is usually driver dependent and different drivers prefer distinct configurations for each race track.

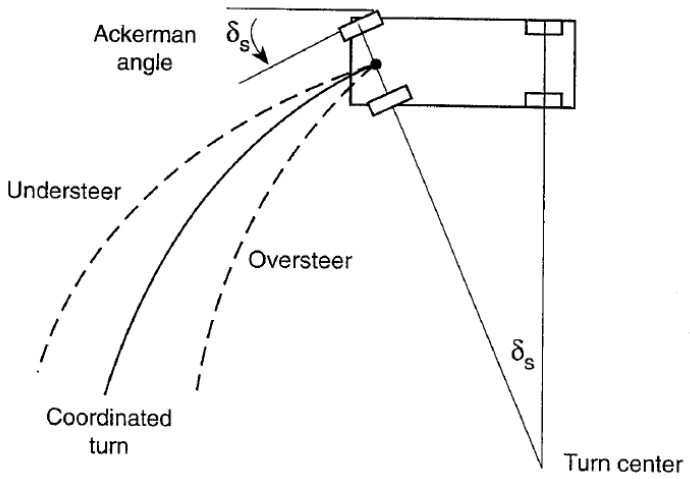


Figure 2.3: Schematic of a car's trajectory when it suffers oversteer and understeer [7].

## 2.2 Main aerodynamic devices

The most common aerodynamic devices in formula-style cars are the front wing, side pods, undertray and rear wing. Their function varies slightly depending on the vehicle's aerodynamic concept, however they are all critical to preserve the aerodynamic balance.

Front wings, such as the one shown in Fig. 2.4, have two main functions: front-end downforce generation and tyre wake control. These are composed of multiple winglets in a cascade, which help mostly with the first function. Tyre wake control is mostly done by vortices generated in the endplates and their various appendices. Due to its forward placement the interaction between its elements and the chassis is key.

The side pods, seen in Fig. 2.5, are found on the side of formula race cars. Though their main function is to provide clean air into the cooling inlets, they also prevent flow separation on the side of the vehicle due to its airfoil-like shape. Side pods also are used to guide the airflow into the rear wing and over the rear diffuser, allowing for greater aerodynamic efficiency.

The undertray of a formula car is its most important aerodynamic component as it is used to generate most of a vehicle's downforce. Through the use of ground effect, the underside of the vehicle generates large low pressure zones, which in turn allow the generation of significant

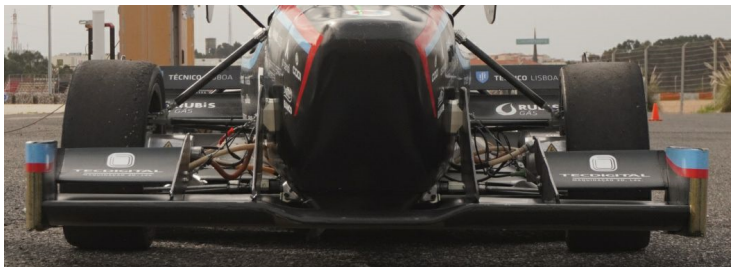

Figure 2.4: Front Wing of the FST10e.


Figure 2.5: Side pod of the Formula One Red Bull Racing's RB18 [9].

vertical loads. Due to its importance this component has very intricate geometries, including multiple vortex generators, strakes and diffusers, as seen in Fig. 2.6.

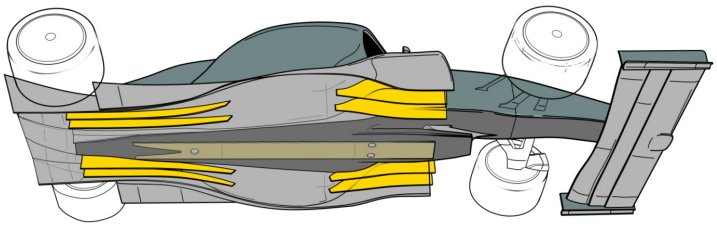

Figure 2.6: Schematic of a 2022 Formula One car underbody [10].

The rear wing is a staple of race car aerodynamic design, being present in almost all competition vehicles. Its positioning allows for the creation of downforce in the rear of the car, which, as most race cars are rear-wheel driven, grants them better traction. However, rear wings are usually the least aerodynamically efficient component of a race car. This occurs mainly due to its positioning, far from the ground and downstream of the vehicle.

Being distant from the ground does not allow the wing to suffer from ground effect, severely hindering its downforce generating capabilities, as such high angles of attack are necessary to compensate this loss. This necessity, however, also comes with a significant drag penalty which significantly reduces the vehicle's acceleration, top speed and further reduces the wing's efficiency. To mitigate this issue, the Drag Reduction System (DRS) was developed. This mechanism allows the temporary reduction of the wing's angle of attack, reducing the vehicle's drag but thus increasing top speed and acceleration. An example of an implementation of this system is shown in Fig. 2.7.

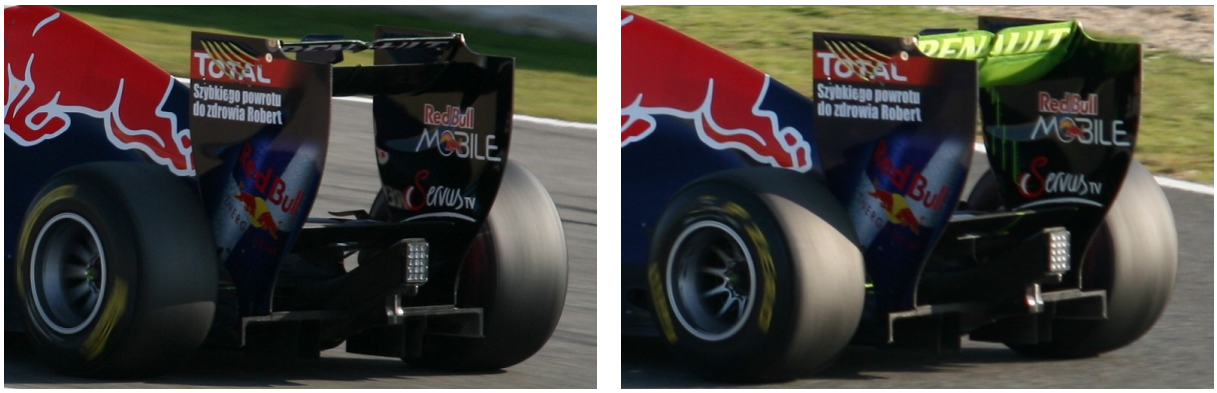


(a) DRS open

(b) DRS closed

Figure 2.7: DRS mechanism of the Formula One Red Bull Racing's RB7 [11].

As the wing is positioned rearwards of every other component of the car it usually operates in turbulent flow and with large separation regions preceding it. These operating conditions also contribute to the low aerodynamic efficiency, as the aerofoils composing the rear wing will be working in non-ideal situations, reducing their downforce generating capabilities and, in some cases, leading to the formation of flow separation regions.

In Formula Student (FS), rear wings commonly have more than three elements and large endplates [12] due to the aforementioned issues that are common in rear wing design, placement and incoming turbulent air. The wing is generally placed at a height of 0.8 m, due to regulation constraints,which leads to multiple wing elements being required to generate a significant enough load that preserves the correct aerodynamic balance. Being so close to the driver's head and rear wheels means that the wing's performance is negatively influenced by the turbulent air surrounding it [13]. Larger rear wing endplates usually help to mitigate this issue as they create a physical barrier between the tyre wake and the wing elements. They can also be used to generate additional downforce by creating vortices, and consequently a lower static pressure zone, on the endplate's lower edge [13]. An example of a Formula Student rear wing design is shown in Fig. 2.8.


Figure 2.8: Rear wing of the AMZ race car (Zurich, Switzerland) [14].

Formula One rear wings on the other hand are highly restricted by regulations, leading to extremely similar designs between the various cars. Teams tend to develop specific wing configurations for each track. These wings are not the main generator of downforce of a Formula

One race car, typically creating only between 10% and 20% of the total downforce [15]. As the F1 cars tend to be highly sensitive to drag, some of the bigger developments on the rear winds are centered around the endplates and how they can be used to reduce the intensity of the wingtip vortices generated by this component. One such example is shown in Fig. 2.9, where the endplate has various slots and cuts that help increase the component's aerodynamic efficiency [15].


Figure 2.9: Rear wing endplate of the McLaren MP4-31 [16].

## 2.3 Aerodynamics study tools

There are three main ways of studying the fluid flow around a vehicle: Computational Fluid Dynamics (CFD), wind tunnel tests, also named Experimental Fluid Dynamics (EFD) and on-track testing. All of these tools have their advantages and disadvantages depending on the use case.

### 2.3.1 Computational fluid dynamics

Computational fluid dynamics studies are a key tool in current aerodynamic analysis, as they are currently the cheapest method of modelling flow structures.

Navier-Stokes are a set of partial differential equations that describe the motion of viscous fluids. They are necessary for aerodynamic modelling as they allow the prediction of how air will flow around an object. However, analytical solutions of these equations for an arbitrary geometry are impossible to obtain, due to their non-linearity. As such, numerical methods are necessary in order to obtain approximate solutions. In order to obtain relevant data in engineering flows, a numerical model of the Navier-Stokes equations must be able to capture viscous effects and turbulence, as these are the two main flow features that influence aerodynamic performance. The most used modelling methods for aerodynamic problems are Large Eddy Simulations (LES) and Reynolds-Averaged Navier-Stokes (RANS) as they are able to capture the desired effects, with some modelling simplifications.

When used in race car development, CFD allows the production of much better performing aerodynamic parts as they can be constantly improved without requiring on-track time and resources to build them [17]. The biggest drawbacks of the usage of CFD in engineering are the

modelling and numerical errors, caused by simplifications done to the Navier-Stokes equations and simulation domain.

#### Large eddy simulations

Large eddy simulations use some simplifications in the Navier-Stokes equations to reduce the necessary computational resources. This approach computes the large scale turbulence (large eddies) while modelling the small scale [18]. This simplifications still allows a reasonable approximation to turbulence modelling as large eddies contain most of the turbulent energy and are responsible for most of the momentum transfer. However, LES is computationally expensive as long simulations times are required to converge the mean and fluctuating components of the flow field.

The use of LES simulations on engineering flows has been steadily increasing as more computing power becomes easily accessible. It has seen use in jet flows and gas turbines [19] as it yields results similar to experimental data, proving how suited this method is for these applications.

#### Reynolds-averaged Navier-Stokes

RANS is the most used CFD approach [20]. Its relatively low computational requirements make it the primary choice in engineering flows as it allows almost any geometry to be analysed. It is, however, less accurate as turbulence is completely modelled and only the averaged quantities are solved.

Instead of solving turbulence itself, RANS models solve the Reynolds stresses that result from the flow averaging process to account for the turbulent fluctuations in the fluid's momentum. There are various turbulence models that attempt to model this phenomenon, some of the more widely used are the $k-\omega$ [21] and $k-\epsilon$ [22] based models, where $k$ is the turbulent kinetic energy, $\omega$ the specific rate of dissipation of $k$ and $\epsilon$ the rate of dissipation of $k$. These models mainly differ in their second transport variables, $\omega$ and $\epsilon$, yielding slightly different results depending on the region being analysed, the first one tends to give more accurate results near walls while the second one yields better results far away from walls.

RANS turbulence models-based simulations, due to their modelling limitations [23], perform the best while analysing trends and not absolute values. These modelling errors have recently started being actively tackled with more application specific models, such as the $k-\epsilon-C_{as}$ [24], a turbulence model intended to better describe the airflow in motorsport applications.

### 2.3.2 Experimental fluid dynamics

EFD usually consists of analysing the airflow around or inside a component in a wind tunnel. This method allows for a much better analysis of a part's performance as opposed to CFD as the physics are the exact same. The scale however, is not, causing the flow to not have the exact same Reynolds and Mach numbers as its full scale counterpart. In low-speed wind tunnels, this leads to scale-effects, discrepancies between full-scale and model data created by differences in the Reynolds number [25]. Small items often tend to be ignored in the production of the scale models, as even when they can be produced, the Reynolds effects are too great for these small geometries to produce comparable results.

As wind tunnels test sections are bounded by walls, blockage, represented in Fig. 2.10, is created. This phenomenon causes the flow to move faster near between the model and the walls,

leading to higher force readings [7]. Larger test sections do help improve this problem, however, as the wind tunnel size increases, so do building and upkeep costs as larger fans are also required.

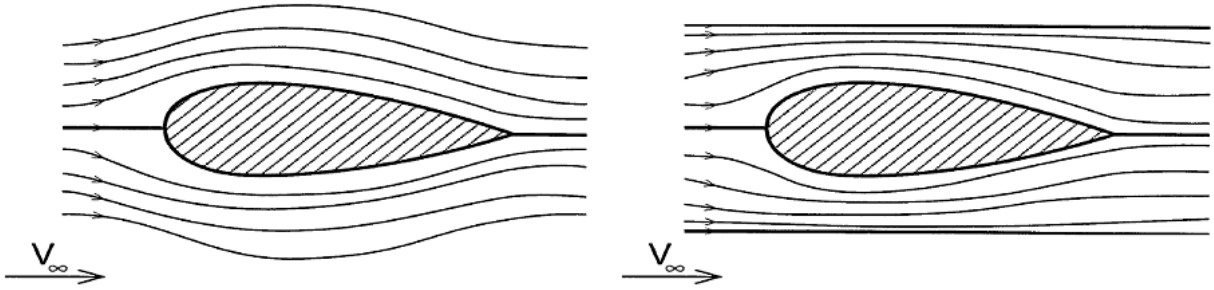


(a) Free Stream (b) Constrained by walls

Figure 2.10: Streamlines near a body [7].

Model production is also one of the downsides of wind tunnel testing as it usually requires high precision equipment to correctly detail the necessary geometries.

Even with these limitations, the wind tunnel is still one of the most powerful tools available in aerodynamics, as it allows a better understanding of the flow phenomena around a vehicle than what CFD simulations can currently provide [25].

### 2.3.3 On-track tests

On-track testing has the biggest advantage of using the full scale race car under the exact same conditions it will actually compete in [7].

The main measurements done on-track are: force, surface pressure and flow visualisation. The scope of these measurements is limited mainly by the ability to carry the testing equipment, as these tests usually involve adding instrumentation to the vehicle. The lack of control of the environmental conditions might also be an issue as the accuracy of the obtained data can be affected [7].

Downforce measurements in a race car are done by measuring the suspension travel at speed due to the aerodynamic load. Strain gauges are some of the most common sensors used for these measurements [26]. In open-wheeled vehicles, the lift of each wheel cannot be measured through this method since it does not directly affect the suspension travel.

Aerodynamic drag can be obtained by various methods, being the most commonly used in Formula Student the coast-down test. Which consists of bringing the vehicle to a certain speed and letting it decelerate until it stops [27]. Based on the distance travelled, the drag coefficient can be estimated. This method usually needs various repetitions as it is more sensitive to disturbances than other methods.

Surface pressure measurements intend to measure the surface static pressure with a transducer. By measuring various points, the pressure distribution over the vehicle or a certain component can be obtained [7]. The main drawback of this method is that individual tubes need to be connected to each surface pressure tap, making its integration difficult.

Flow visualisation techniques, even though simple, are extremely effective tools to analyse the airflow around the vehicle. They allow engineers to clearly see where separation zones are created [28]. Viscous liquids or taped wool tufts are placed on the car's surface, these are then recorded and later analysed. Some examples of these methods are shown in Fig. 2.11.

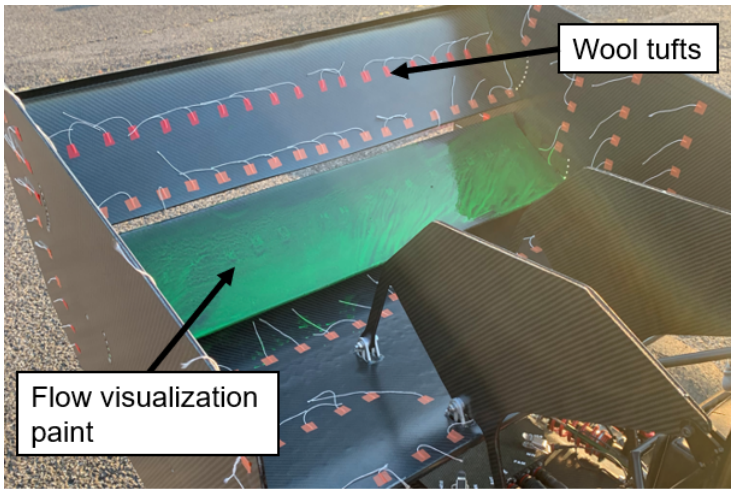


Figure 2.11: Examples of flow visualisation methods applied on the FST10e.

In order for any of these methods to be accurate, additional data is usually required. Dynamic pressure $\frac{1}{2}\rho v^2$, obtained through velocity, is usually the most important as it is needed to calculate aerodynamic forces and surface static pressure [7]. Car attitude data can also be valuable as it allows a further insight into how each variable changes as the car travels through different sections.

On-track testing is still the best method to assess aerodynamic performance, however having to build the necessary components each time they have to be tested can be a deterrent to its further use. This is especially true in Formula Student due to tight budgets.

## 2.4 Previous studies

Some initial aerodynamic validation work on FST Lisboa's cars has been done in [29] and [30]. In the first study, a 3D printed model of the FST10e was built and its aerodynamic coefficients were estimated in one of the wind tunnels from Instituto Superior Técnico (IST). The second study analysed the car's on track performance in order to estimate the generated downforce, drag and aerodynamic balance.

### 2.4.1 Wind tunnel validation

The first attempt from FST Lisboa to validate CFD results was conducted during the development cycle of the FST06e. A 40% scale model of the vehicle's rear wing was built and tested in one of IST's open section wind tunnels, as shown in Fig. 2.12. These experiments, however, did not yield useful results as no dynamic similarity was achieved due to the model Reynolds' number being four times lower than the expected full scale value.

In [29] a second attempt at taking wind tunnel measurements was made, this time using IST's closed-section aeroacoustic wind tunnel. In this work, a fully automated CFD setup and parametric Computer Aided Design (CAD) were created to allow an effortless study of various car configurations in the wind tunnel. This setup also grants the user the ability to easily change the aerodynamic devices to accommodate components in future vehicle designs. In order to allow accurate measurements to be taken, firstly the turbulent intensity of the wind tunnel was measured using hot film anemometry. Then, an aerodynamic balance frame support was built. A

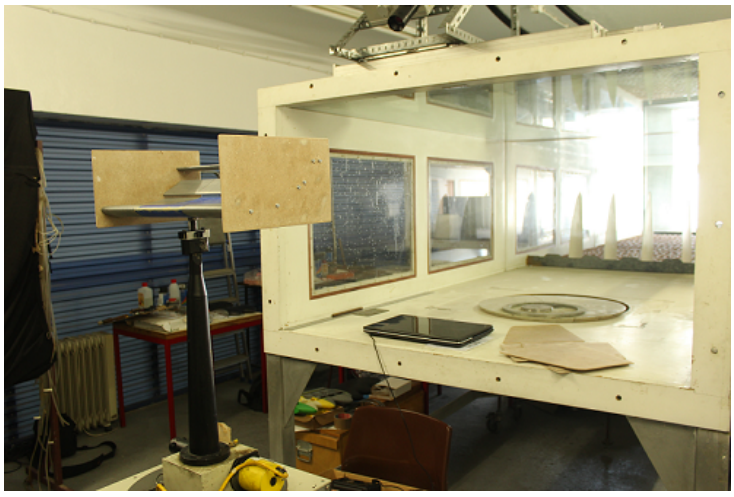

Figure 2.12: FST06e wind tunnel testing [29].

1/3 scale model of the FST10e, shown in Fig. 2.13, was built and tested in the aforementioned wind tunnel. From the measured data, it was possible to observe that the numerical results captured the experimental tendencies. A quantitative evaluation of the results was, however, not possible due both to high measurement and numerical uncertainties.

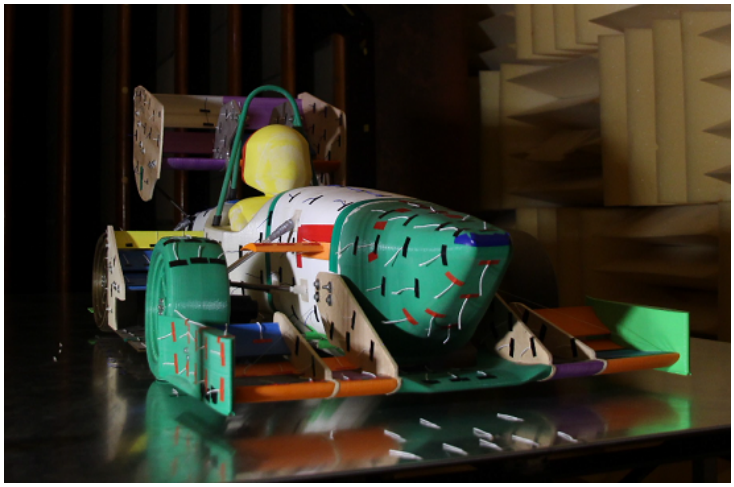

Figure 2.13: FST10e wind tunnel testing [29].

### 2.4.2 On-track validation

The work done in [30] was FST Lisboa's first attempt at aerodynamic on-track testing. Measurements of the $C_L$, $C_D$ and aerodynamic balance were made in order to validate the aerodynamic performance.

A nearly fully automatic CFD workflow was created in order to facilitate the interaction between CAD modelling and CFD, this also allows an easy method of consecutively running multiple simulations. A data set of 114 simulations of various car configurations was then created, to allow the setup of a surrogate model relating the various aerodynamic parameters with car attitude. This model was generated to estimate the on-track performance of all car attitudes without having to run all the possible simulation configurations. The car was then run

on track where two main tests were conducted at three different ride heights: first, a constant velocity test to estimate downforce; then, a coast down test where drag was measured. The final results, which are represented in Fig. 2.14, showed that the numerical results followed the tendency of the experimental results, however, as was the case in the wind tunnel, quantitative comparisons are not viable due to high numerical and experimental uncertainties.

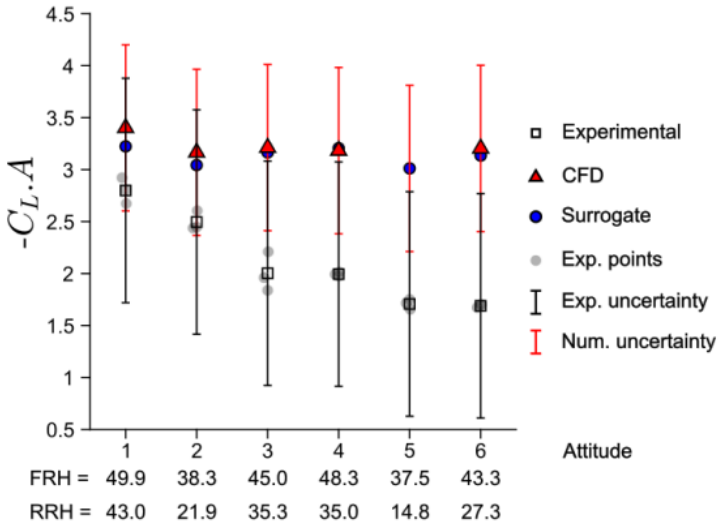


Figure 2.14: $C_L A$ results from constant speed testing shown in [30].

# Chapter 3

# Race simulator

This section briefly presents the point mass simulator supplied by the FST Lisboa's vehicle dynamics department and the modifications made to better describe the aerodynamic influence in these prototype vehicles. Its usage allows the definition of the aerodynamic design strategy to be followed.

## 3.1 Dynamic model

The simulator currently in use is a Quasi-Steady-State (QSS) lap time simulator which considers the vehicle as a single point mass moving through a predefined track layout. It takes as inputs several parameters, such as lift and drag coefficients, vehicle mass, tyre and motor characteristics. The track is composed of a series of elements which contain information about the section length and its curvature radius. The QSS approach considers that each manoeuvre (acceleration, braking and cornering) is smooth and therefore can be approximated assuming steady-state. By joining together these behaviours, an approximation of a car's velocity and position throughout the track can be obtained [31].

The vehicle's motion is described by Newton's equations. This allows a simple but effective way of modelling the vehicle's performance throughout the track, as they can represent the car in three axis and three rotational degrees of freedom [32]. In order to complete a lap, the simulator follows a simple loop where the car's velocity is constantly being checked. Then, the simulator proceeds to compare the velocity to the section's limit before accordingly adjusting the car's motion, as shown in the flowchart represented in Fig. 3.1, and recalculating its velocity and position.

Each section is simulated through the successive solution of the differential equation, that represents the dynamics in the tangential direction,

$$a_i = \frac{\mathrm{d}v(t_i)}{\mathrm{d}t_i} = \frac{F(v(t_i))}{M_{eq}(v(t_i))}, \tag{3.1}$$

where $a_i$ is the vehicle's acceleration, $v$ is the velocity and $M_{eq}$ the equivalent mass of the car, the sum of the static mass and the equivalent mass of the rotating parts. The integration of Eq. (3.1),

$$\int_{v_i}^{v_{i+1}} dv = \int_{t_i}^{t_{i+1}} a(t)dt, \tag{3.2}$$

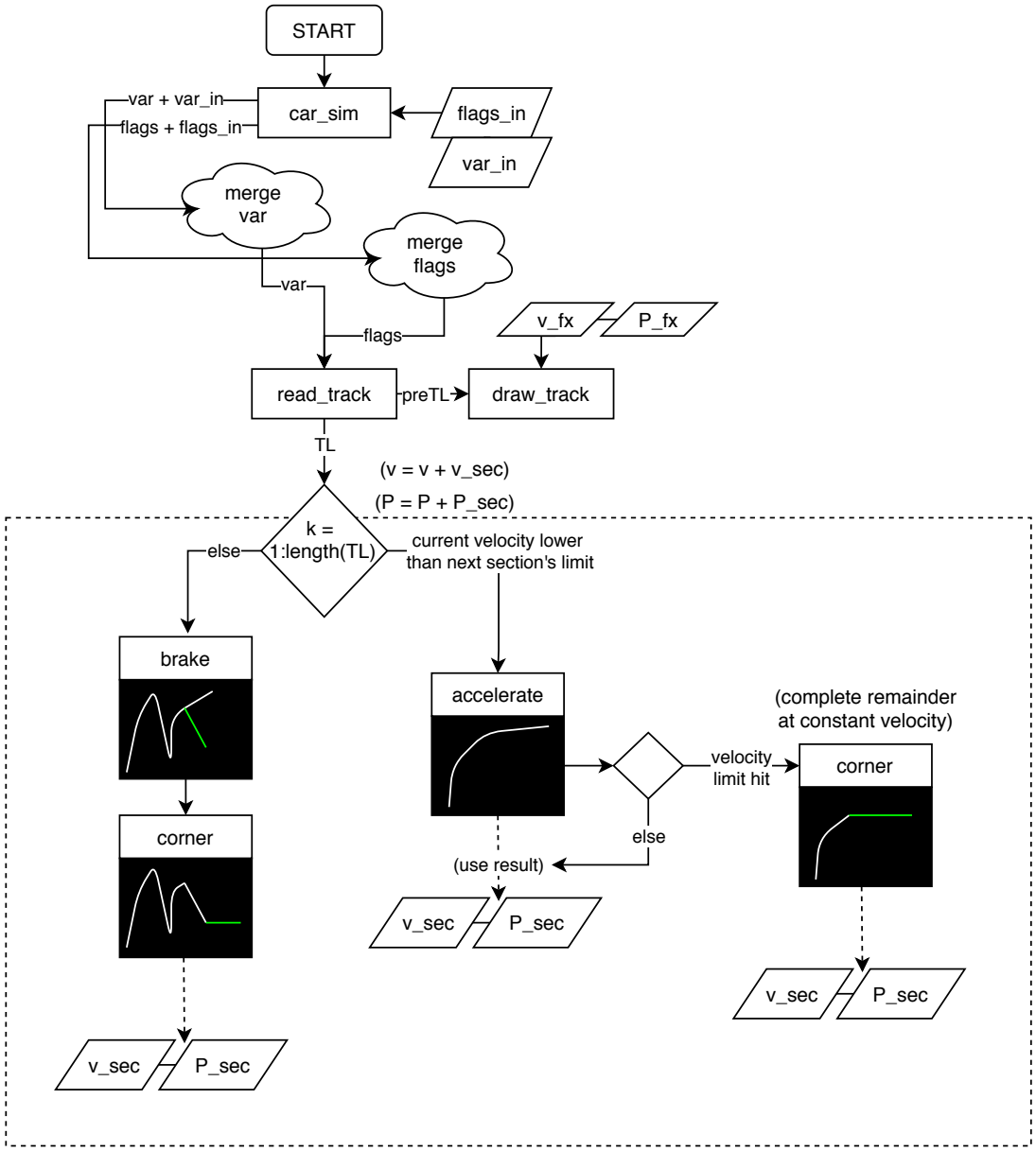


Figure 3.1: QSS Laptime simulation flowchart.

can be converted through trapezoidal integration to

$$v_{i+1} - v_i = \frac{1}{2}(a_{i+1} + a_i)(t_{i+1} - t_i), \tag{3.3}$$

which represents the relation between the vehicle's velocity and its acceleration in a section. The interval $t_{i+1} - t_i$ is defined as the simulation time step.

Consequently, the vehicle's acceleration in each section can be described by

$$a_{i+1} = \frac{F_{driving}(t_i) - F_{braking}(t_i) - F_{drag}(t_i) - F^{rolling}_{resistance}(t_i)}{M_{eq}(t_i)}, \tag{3.4}$$

where $F_{driving}$ is the vehicle's tractive force, $F_{braking}$ the vehicle's braking force, $F_{drag}$ the vehicle's aerodynamic drag and $F^{rolling}_{resistance}$ the vehicle's rolling resistance. In a straight acceleration, $F_{braking}(t_i) = 0$ whereas in braking $F_{driving}(t_i) = 0$. If the instant velocity is higher than the

track section's maximum allowed velocity during a constant velocity corner, then $F_{driving}(t_i) = 0$.

$F_{driving}(t_i)$ is calculated through the function min{Traction, Motor Force} where both Traction and Motor force are $4 \times 1$ vectors containing the forces applied on each wheel. The motor force is obtained through the motor curve that relates motor torque, motor speed in RPM and motor power. The curve of each motor used in the FST10e when they are at maximum power is shown in Fig. 3.2.

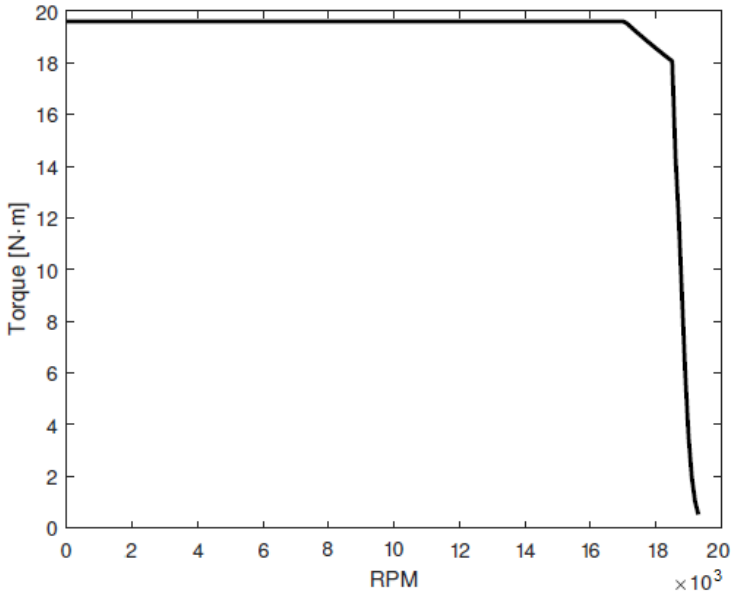


Figure 3.2: Motor curve of the FST10e when powered with 35kW.

From this relation, motor force can be obtained from

$$F_{motor} = \frac{\tau_{motor}}{r_{wheel}}, \tag{3.5}$$

where $F_{motor}$ is the applied force on each motor, $\tau_{motor}$ the motor torque and $r_{wheel}$ the wheel radius.

The traction at each instant is calculated through a linear, load sensitive, tyre model [33],

$$\text{Traction}(t_i) = \begin{bmatrix} N_{RR} & {N_{RR}}^2 \\ N_{RL} & {N_{RL}}^2 \\ N_{FR} & {N_{FR}}^2 \\ N_{FL} & {N_{FL}}^2 \end{bmatrix} (t_i) \cdot \begin{bmatrix} {\mu_x}^o \\ {\mu_x}' \end{bmatrix}, \tag{3.6}$$

where $N_i$ are the normal forces for each wheel, with the subscripts Rear Right (RR), Rear Left (RL), Front Right (FR) and Front Left (FL) wheel. The longitudinal tyre load sensitivity coefficients include ${\mu_x}^o$, representing the zero intercept, and ${\mu_x}'$ the slope of the function $\mu(F_z)$. The vertical load, $F_z$, and the longitudinal load, $F_x$, on each tyre are related by

$$F_x(t_i) = F_z(t_i)\mu(F_z) = F_z(t_i)({\mu_x}^o + {\mu_x}' F_z(t_i)), \quad {\mu_x}' < 0. \tag{3.7}$$

To calculate the loads on each wheel, the longitudinal weight transfer is first calculated as

$$Tf_{Long}(t_i) = \frac{h_{CoG} \cdot a_x(t_i)}{WB \cdot g}, \tag{3.8}$$

with $h_{CoG}$ being the height of the car's centre of gravity, $a_x(t_i)$ the instantaneous longitudinal acceleration, $WB$ the vehicle's wheelbase and $g$ the gravity constant. Then, the loads are given by

$$\begin{bmatrix} N_{RR} \\ N_{RL} \\ N_{FR} \\ N_{FL} \end{bmatrix} (t_i) = W \cdot \begin{bmatrix} w_{rr} \cdot w_{rt} & w_{rr} \cdot w_{rt} \\ w_{rr} \cdot w_{lf} & w_{rr} \cdot w_{lf} \\ w_{ft} \cdot w_{rt} & -w_{ft} \cdot w_{rt} \\ w_{ft} \cdot w_{lf} & -w_{ft} \cdot w_{lf} \end{bmatrix} \cdot \begin{bmatrix} 1 \\ Tf_{Long}(t_i) \end{bmatrix} + \frac{1}{2} F_L(t_i) \cdot \begin{bmatrix} df_{ft} \\ df_{ft} \\ df_{rr} \\ df_{rr} \end{bmatrix}, \tag{3.9}$$

where W is the vehicle's static weight, $w_{rr}$ and $w_{ft} = 1 - w_{rr}$ are the weight distributions, respectively, on the rear and front axles and $w_{rt}$ and $w_{lf} = 1 - w_{rt}$ the lateral weight distributions, which are assumed $w_{rt} = w_{lf} = \frac{1}{2}$ for a laterally symmetric car. If the aerodynamic parameters are considered, $df_{ft}$ and $df_{rr}$ are the downforce distribution on the front and rear axle, respectively, and $F_L(t_i)$ the downforce at instant $t_i$.

This model has some limitations due to the simplifications made: the vehicle spends most of its time accelerating, as such it is highly biased towards a front-heavy downforce distribution as downforce in the frontal part of the vehicle counteracts the loss of grip from reduced front tyre load during acceleration. However, even though there is a force distribution between the wheels, concepts such as understeer and oversteer, which are also associated with the aerodynamic balance, are not included.

Currently, both $C_LA$ and $C_DA$ values are input as two separate variables, leading to no relation between the two aerodynamic parameters. This creates a poor aerodynamic model, as an increase in $C_LA$ will not lead to a consequent increase in $C_DA$. As such, analysis of the impact of the aerodynamic parameters in the vehicle performance leads to a data set where most of the final results are unrealistic.

## 3.2 New aerodynamic model

To better assess the influence of having an aerodynamic package, a relationship must be established between the lift coefficient, the drag coefficient, the total area of the aerodynamic package and the aerodynamic package mass. To achieve this, the following steps were made:

1. Analysis of the time step numerical error;
2. Drag polar calculated based on simulation data from [30];
3. Relation between area of the aerodynamic package of the FST10e and its mass established;
4. Lift coefficient dependency on aerodynamic package area created to relate $C_L$ and mass.

### 3.2.1 Time step analysis

As a mean to estimate the numerical error and convergence of the race simulator, a series of simulations of the expected team score on the dynamic events were made, using various time steps, as summarized in Fig. 3.3. High numerical errors in this type of race simulators are undesirable as they create biases in the results due to some track sections being poorly solved.

A time step value of 1 ms was chosen since reducing the time step value showed a score variation lower than 1%, meeting the set error threshold. Lower time step intervals are too computationally expensive, as simulation time increased by several orders of magnitude.

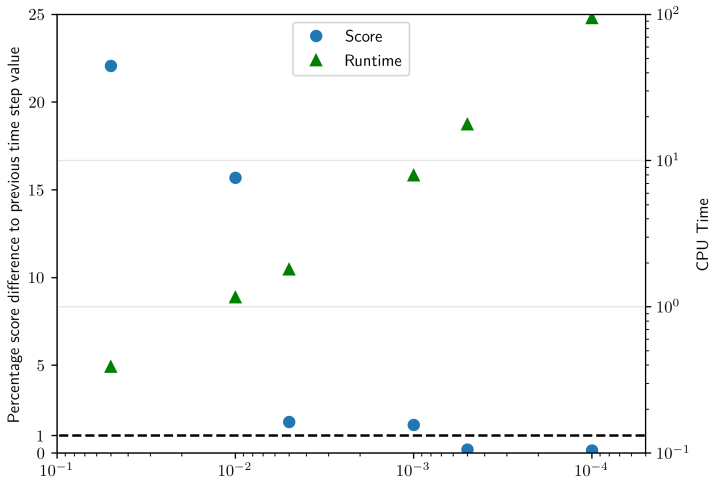


Figure 3.3: Percentage score difference between a time step value and its predecessor.

### 3.2.2 Drag polar

Based on the simulation data obtained in [30], where aerodynamic performance at different car attitudes was studied, a drag polar was estimated. Additionally, a simulation result with no aerodynamic package was added to obtain the $C_{L0}$ and $C_{D0}$ values. A parabolic regression was used as it is commonly employed in subsonic aerodynamics [34] and race cars [7]. This approach allows an estimation the induced drag caused by the increase in downforce.

From Fig. 3.4, the resulting polar equation can be obtained

$$C_D A = 0.0244 C_L A^2 + 0.2616 C_L A + 0.4232, \tag{3.10}$$

the regression curve successfully fits the results with $R^2 = 0.934$, having only one major outlier at $C_L A = 2.15 m^2$. A data set with more evenly spread simulation results would have been more desirable, however, a race car aerodynamic package is designed to not be very sensitive to car attitude changes.

### 3.2.3 Relation between mass and lift coefficient

Using data from both mass and aerodynamic package area of FST Lisboa's two previous vehicles, the FST 09e and FST 10e, summarized in Tab. 3.1, a relation between the $C_L A$ and area was first established through a linear regression: $A = 3.48 C_L A + 2.16$. Then, the coefficient

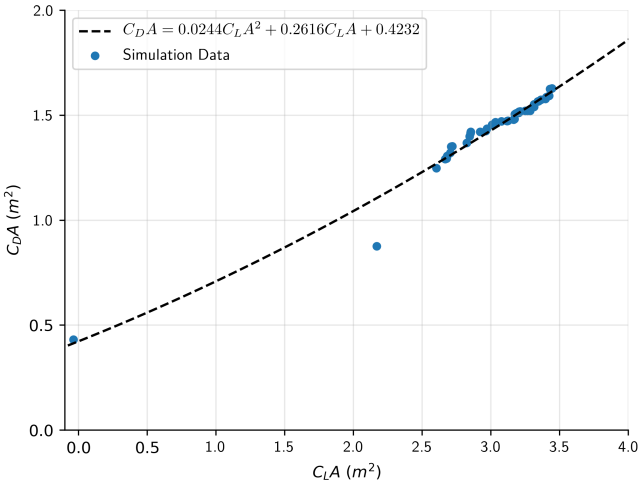


Figure 3.4: Drag polar data and its corresponding parabolic regression.

between the mass and area of the FST10e was calculated: $\frac{m}{A} = 1.47kgm^{-2}$. Using these two relations, the mass can be related to $C_LA$ as

$$m = (3.48C_LA + 2.16) \times 1.47. \tag{3.11}$$

This approach, even though simplistic due to the relation between all these coefficients being clearly non-linear, is effective as it creates a model simple enough to implement in the simulator. This method will also enforce an upper bound to $C_LA$ as the successive increase in mass as this coefficient rises will rapidly penalise the car's acceleration.

A better approximation of this relation could possibly be obtained with more data from even older cars. However, since different composite materials were used and there is almost no simulation data from previous cars, it was decided against this approach.

| Vehicle | $C_LA\ (m^2)$ | Mass (kg) | Total Area $(m^2)$ |
|---|---|---|---|
| FST 09e | 2.80 | 20.0 | 11.9 |
| FST 10e | 3.42 | 20.7 | 14.1 |

Table 3.1: Aerodynamic package weight and area data from FST Lisboa's two previous vehicles.

## 3.3 Revised aerodynamic targets

Using the modelling data presented in the previous section, a new study was made using the race simulator. The $C_LA$ values were analysed in the interval $[2, 8]$ as it the includes most of the lift coefficient values obtained in Formula Student. The resulting analysis yielded the data shown in Fig. 3.5. The reference case used to calculate the $\Delta Score$ was the default configuration of the FST10e.

It is clear that there is a maximum score value for the $C_LA$ of the vehicle at $C_LA = 5.75$. Further analysis was done to evaluate how each event was affected by the changes in the various

parameters.

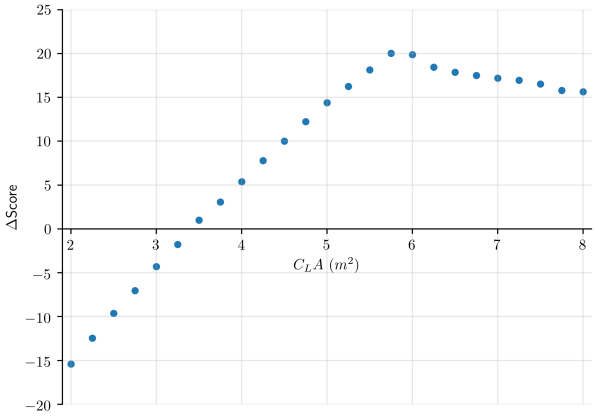


Figure 3.5: Total competition score variation.

The data was divided into three groups, according to the previously thought aerodynamic targets: skidpad and autocross, events where $C_LA$ was thought to have a significant impact; acceleration, where only mass and $C_DA$ should impact the results; endurance and efficiency where aerodynamic efficiency should be of utmost importance.

From Fig. 3.6(a), the previously held assumption was correct, as the score on the skidpad and autocross increase with $C_LA$.

The skidpad event focuses on the car's ability of producing lateral acceleration, as such, the peak longitudinal velocities are usually not significant enough to lead to a scenario where the vehicle's acceleration or top speed are drag limited. Therefore, a high downforce package is ideal for this event, as an increase in vertical load being applied on the tires will allow greater lateral acceleration.

In the autocross event peak performance is evaluated, therefore a balance between longitudinal and lateral acceleration needs to be struck. Since energy consumption is not counted towards the final score, high drag values can be overcome by supplying more power to the electric motors. This creates a scenario where high $C_LA$ is desirable in order to increase performance, but, as seen in Fig. 3.6(b), there is a limit on how high the lift coefficient should go, as the increase in drag and mass will eventually hinder the performance of the vehicle.

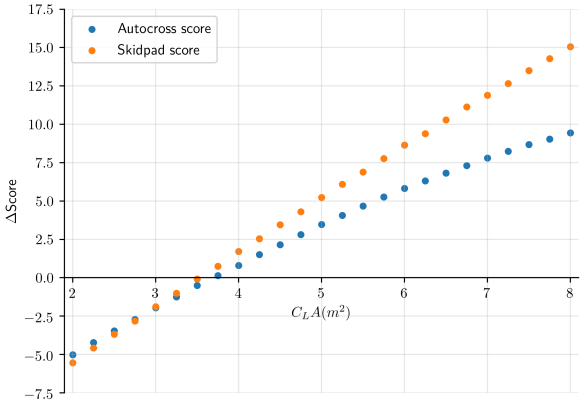


(a) Skidpad and Autocross

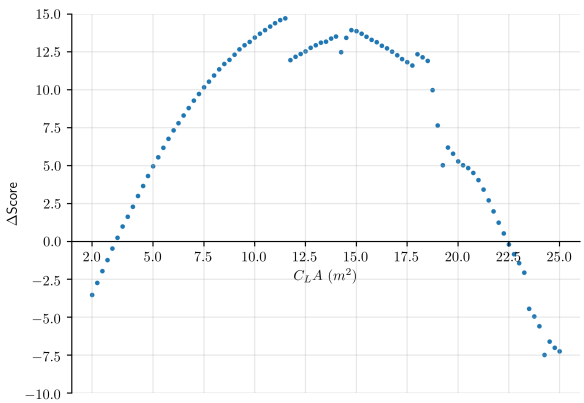


(b) Larger autocross interval

Figure 3.6: Score variation on the events where $C_LA$ has the most importance.

Regarding the acceleration data, Fig. 3.7, the results are also as expected, with the increase of $C_LA$, $C_DA$ and mass, the score diminishes. This event focuses in longitudinal acceleration, which is most impacted by $C_DA$ and mass. The increase in traction caused by the higher $C_LA$ is not significant enough to increase the vehicle's performance. Therefore, in this event the aerodynamic package should be configured in a way to reduce drag as much as possible.

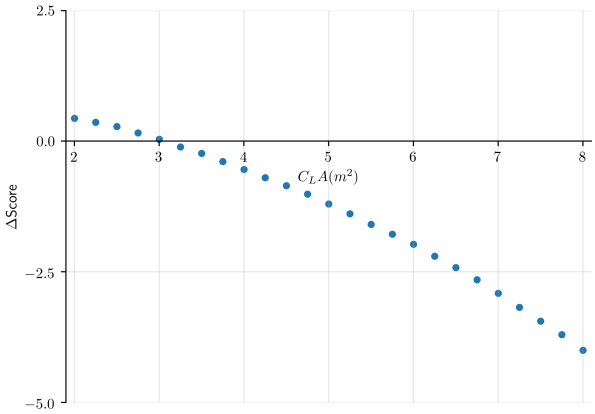


Figure 3.7: Score variation depending on the lift coefficient for the acceleration event.

As the relation between performance and energy consumption is the focus of the endurance and efficiency events, an aerodynamic package with high efficiency is desirable. A car with decent cornering capabilities is, however, still necessary to achieve a good level of performance, thus the higher $C_LA$ requirement for this event, as seen in Fig. 3.8.

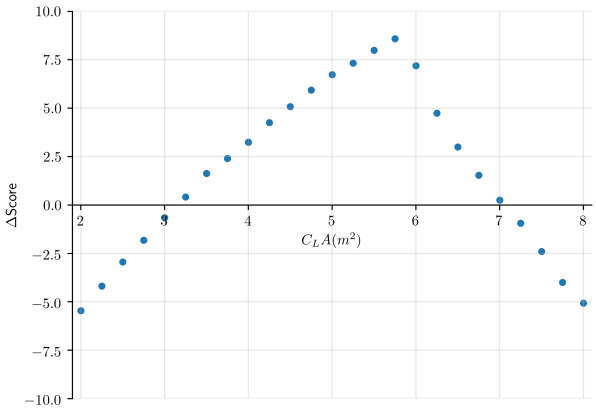


Figure 3.8: Competition score variation for the endurance and efficiency events.

The focus of this study is the vehicle performance in the Endurance and Efficiency events, the ideal properties for the aerodynamic package are

- $\mathrm{C_LA} = 5.75\,\mathrm{m}^2$ (from Fig. 3.8);
- $\mathrm{C_DA} = 2.73\,\mathrm{m}^2$ (from Eq. (3.10));
- $m = 32.58$ kg (from Eq. (3.11)).

Higher $C_LA$ and lower $C_DA$ configurations should also be made available for the skidpad, autocross and acceleration respectively. Ideally, the car's $C_LA$ will be increased without significantly increasing the mass and $C_DA$, which is the goal this work.

# Chapter 4

# Base geometry analysis

This chapter elaborates on the CAD and CFD tools used in this work. An analysis of the baseline simulation was also done to evaluate where the current rear wing could be improved.

## 4.1 Simulation setup

The simulation setup is based on [30], where a fully adjustable model of the FST10e was created using *Siemens NX™* in order to speed up the interaction between the CAD and CFD. This model allows the user to easily change features such as ride height, front wing and rear wing flap angles, front wing height and roll angle using the *Expressions* window from *NX*, an example of this change can be seen in Fig 4.1. An ISO 8855 coordinate system [35], where x is positive forward, y is pointed left and z upwards was used, as shown in Fig. 4.2.

| **Parameters** |
|---|
| Front ride height (FRH) |
| Rear ride height (RRH) |
| Wheel steering angle |
| Roll |
| Yaw |
| Pitch |

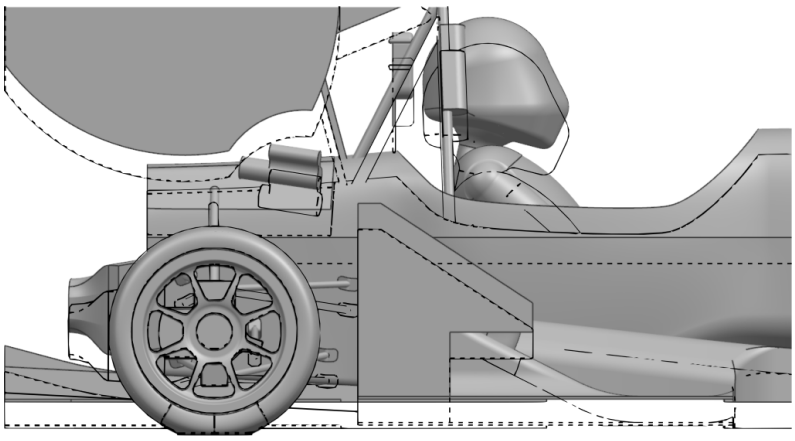

Figure 4.1: Adjustability of the FST10e *Siemens NX™* CAD.

In order to simulate the desired car attitudes and configurations, *Simcenter STAR-CCM+* was used as a CFD simulation tool. Using the supplied macro from [30], all the steps from pre-processing to post-processing are completely automated. Furthermore, in [30] a mesh convergence study was also made where the numerical error was estimated, leading to a final mesh size value of 6.7 million elements for the half car simulation and 14 million elements on a full car simulation.

The following options were used in the simulations:

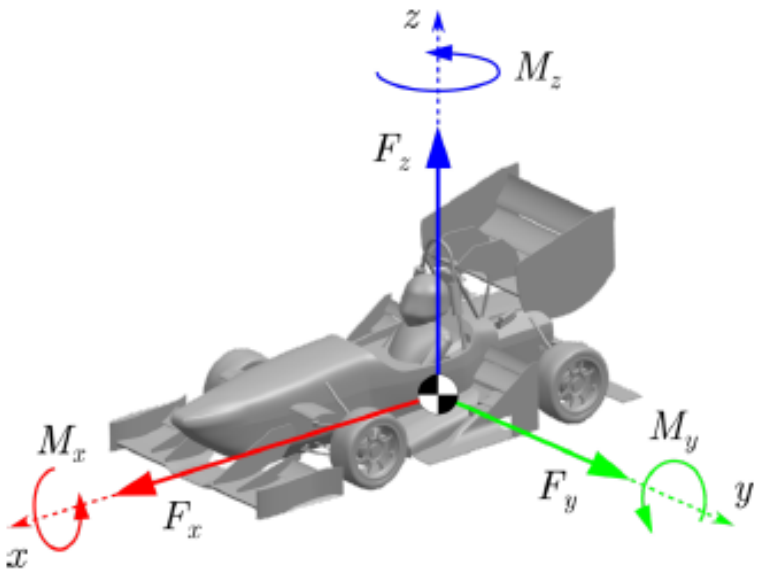


Figure 4.2: Axis system with the origin at the center of gravity [30].

- **Mathematical models -** Reynolds-Averaged Navier-Stokes time-averaging equations , k-$\omega$ SST turbulence, Gamma transition;
- **Solution techniques -** Segregated flow, Steady;
- **Discretization techniques -** Three dimensional, second-order;
- **Fluid properties -** Constant air density and viscosity ($\rho = 1.225\ kg\ m^{-3}$ and $\eta = 1.8 \times 10^{-5}\ Pa \cdot s$).

## 4.2 Baseline analysis

The FST10e, seen in Fig. 4.3 has an aerodynamic package composed of a front wing, rear wing, side diffuser, rear diffuser, side cascade and bullhorns. These elements allow it to generate a $C_LA$ of 3.202 $m^2$ and a $C_DA$ of 1.510 $m^2$ in a straight line configuration. These values were obtained using the following car setup: $FRH = RRH = 40\ mm$, $Roll = Yaw = Inner\ wheel\ steering\ angle = Outer\ wheel\ steering\ angle = 0°$. As this is the expected car configuration while moving at a constant velocity of 11 $m/s$ it was used as a baseline in this work and in [30].

Table 4.1 represents the downforce distribution of the major aerodynamic components of the FST10e. From these values an aerodynamic balance of 31% can be calculated, leading to most of the aerodynamic forces being applied in the rear wheels, causing understeer. It can also be seen that the rear wing is the least aerodynamically efficient component, having a $C_LA/C_DA = 1.8$ due to its high drag value while the diffusers have the highest efficiency at 6.5 and 10, respectively.

The side and rear aerodynamic concept of the FST10e was based on the usage of ground effect on the diffusers and to outwash the low energy air and tyre wake away from the vehicle. To achieve this, the front wing endplate was designed so as to create a vortex that would direct the tyre wake away from the car, as seen in Fig. 4.4. This allows the diffusers to work in a mostly undisturbed flow, increasing their efficiency.

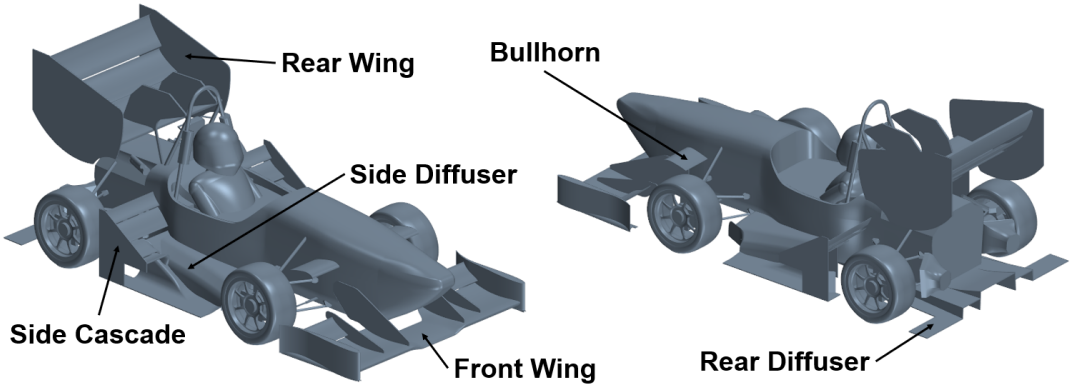


Figure 4.3: Base geometry of the FST10e

Table 4.1: Contribution of each major component to the aerodynamic forces applied on the FST10e.

| **Component** | $-C_L A$ $(m^2)$ | **% Total Downforce** | $C_D A$ $(m^2)$ | **% Total Drag** | **Efficiency** |
|---|---|---|---|---|---|
| Front Wing | 0.73 | 22.7 | 0.10 | 6.7 | 7.3 |
| Rear Wing | 1.02 | 31.9 | 0.57 | 38.0 | 1.8 |
| Side Diffuser | 0.78 | 24.3 | 0.12 | 8.2 | 6.5 |
| Rear Diffuser | 0.39 | 12.2 | 0.04 | 2.6 | 10 |
| Side Cascade | 0.35 | 10.9 | 0.20 | 13.3 | 1.8 |

During the FST10e's development cycle, it was noticed that large vortices were being created near the front wing's supports. These vortices were then being directed into the rear wing, reducing its downforce generation by 30%. To fix this issue, an inverted airfoil, the bullhorn, was placed slightly upstream of the front wing's support in order to generate downwash to prevent these vortices from hitting the rear wing. Since it is placed with the suction side pointing upwards, this airfoil generates lift, which is undesirable in a race car. Directing these vortices into the side cascade also reduces its efficiency, however, the downforce gains on the rear wing were deemed to be much greater than the induced losses.

One of the major shortcomings of the aerodynamic design of the FST10e is the large flow separation region created below the side diffusers at low ride heights, as can be seen in Fig. 4.5. The cause of this phenomenon was deemed to be its flat bottom geometry, instead of a more streamlined one akin to an airfoil. The sudden change in curvature aided by the adverse pressure gradient induce flow separation, reducing significantly the component's efficiency.

The aforementioned low rear wing efficiency can be attributed to both the wing's geometry itself, as it has wing elements with a small aspect ratio, leading to high induced drag, high angle of attack on the flaps, causing an increase in the pressure drag and its positioning rearwards of the car, where most of the car's wake will propagate, further reducing its efficiency. From Fig. 4.7 and 4.8, it can be seen that the first rear wing element is placed directly downstream of the driver's head restraint, causing lower energy air to reach the wing.

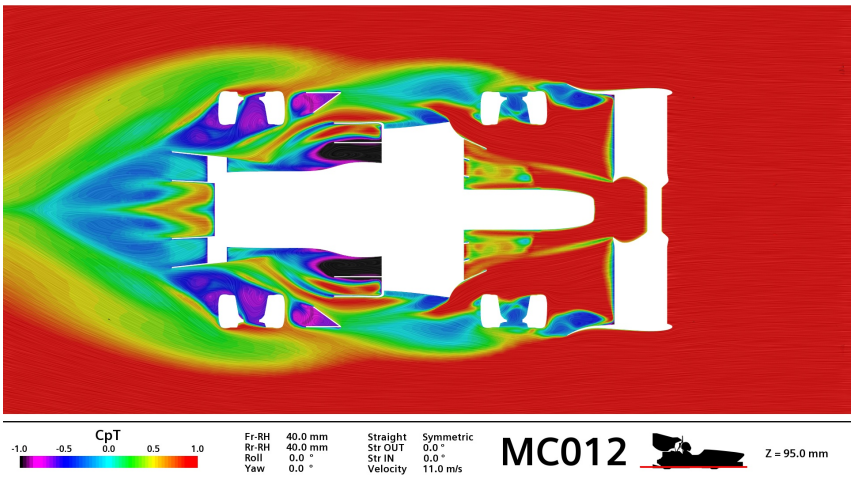


Figure 4.4: Total pressure coefficient of the FST10e at $z = 95mm$

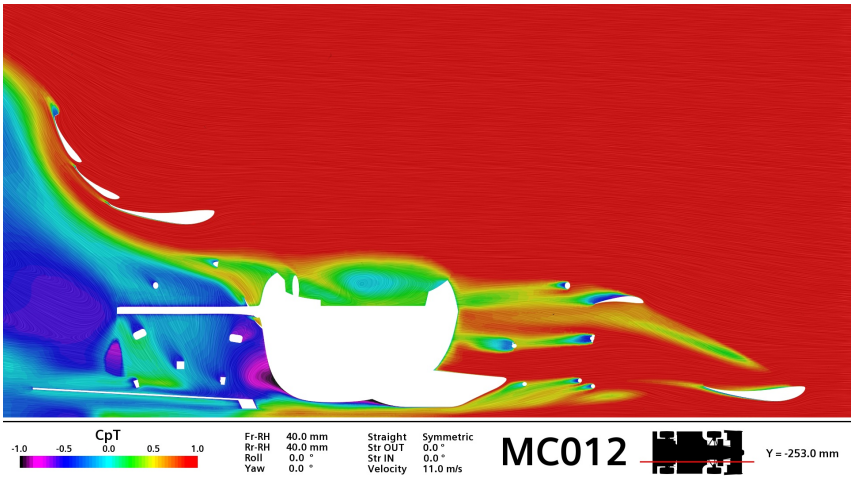


Figure 4.5: Total pressure coefficient of the FST10e at $y = 253mm$

## 4.3 Identified shortfalls and mitigation development plan

To compensate for the previous design shortcomings, the following suggestions were thought, to improve the efficiency of the rear wing:

- Raise the main plane, to reduce losses caused by the driver's head and head restraint wake;
- Restructure the wing cascade, low energy regions are visible downstream of the airfoils though the $C_PT$ plots, these could be reduced through better flap placement:
- Usage of cambered endplates to increase wing efficiency while cornering and increase the suction peak, leading to greater vertical loads.

These changes were tested and implemented in Chap. 5.

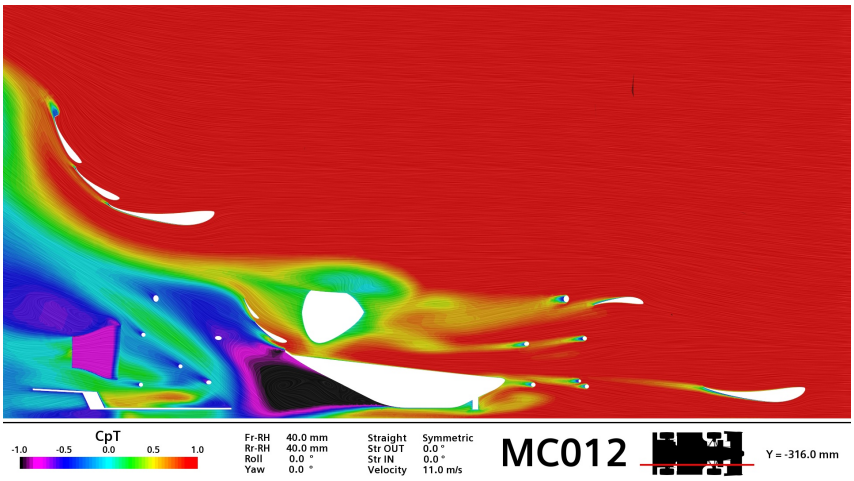


Figure 4.6: Total pressure coefficient of the FST10e at $y = 316mm$

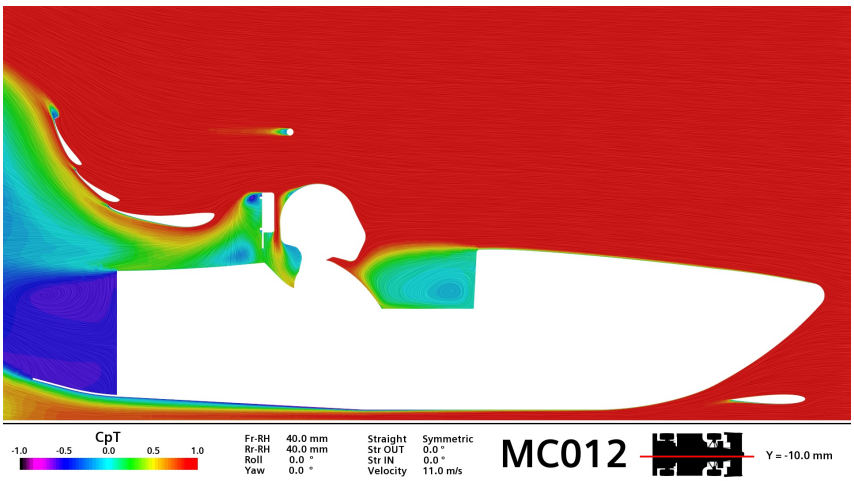


Figure 4.7: Total pressure coefficient of the FST10e at $y = 10mm$

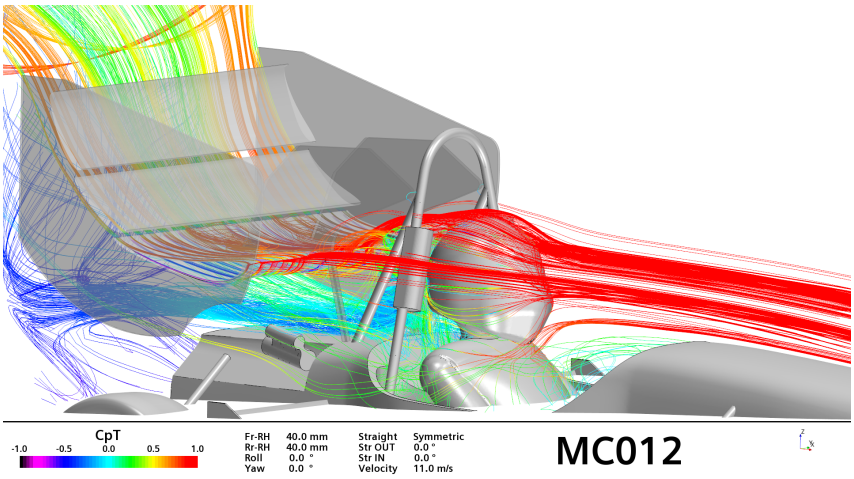


Figure 4.8: Streamlines near the FST10e rear wing.

# Chapter 5

# New rear wing concept

In this chapter, various rear wing concepts were tested, in order to identify the best. Further iterations of that concept were to choose the design to be later tested in the wind tunnel.

## 5.1 Low drag concept

As mentioned in Chap. 1, this work intended to build on the conclusions drawn from [6]. A design based on this rear wing would reduce the vehicle's aerodynamic drag significantly while also slightly reducing its downforce. A smaller rear wing concept such as this one could be placed higher, diminishing the losses induced by the driver's wake region. The baseline rear wing geometry can be seen in Fig. 5.1(a).

### 5.1.1 Geometries

In order to achieve the above goal, the rear wing design shown in Fig. 5.1(b) was tested both in straight line and curve configurations. This design uses two wing elements with 400 $mm$ and 150 $mm$ chord and a curved endplate using the inverted NACA 2402 airfoil, as was studied [6]. As one of the constraints of this design was to maintain the car's current $C_LA = 3.2\ m^2$, a second wing element had to be added, as a single one could not produce the necessary amount of downforce. The rear wing supports were removed to not introduce more variables to each design.

The following iteration consisted of increasing the endplate's span, as, based in the data from [6], increasing the distance between the wing's suction side and the endplate lower edge tends to increase its downforce. This iteration can be seen in Fig. 5.1(c).

### 5.1.2 Results

Using the data from Tab. 5.1 to compare the results from this simulation with the baseline it can be seen that on a straight line the $C_LA$ losses are significant, lowering the vehicle's downforce by 10%. The $C_DA$ however is cut by an even larger amount of 25%, as was intended by this design, showing its potential.

While this concept did not yield the expected results while on a straight line, the curve configuration shows that significant gains are achievable. While on a skidpad configuration, the FST10e loses 8% of its downforce, the improved wing however does not show any cornering losses, compensating its lack of straight line performance.

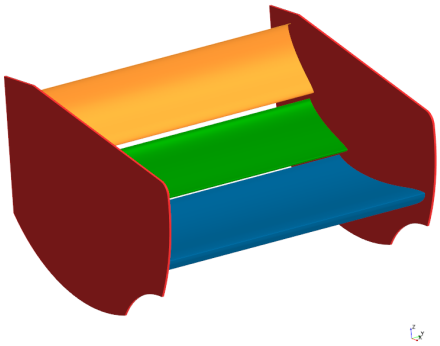

(a) Baseline geometry

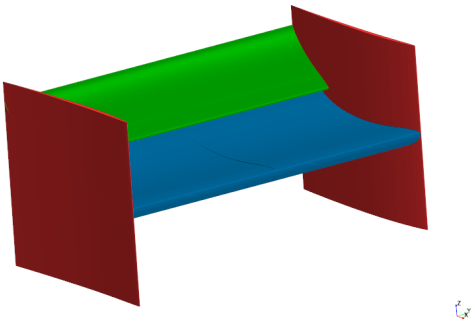

(b) Low drag wing

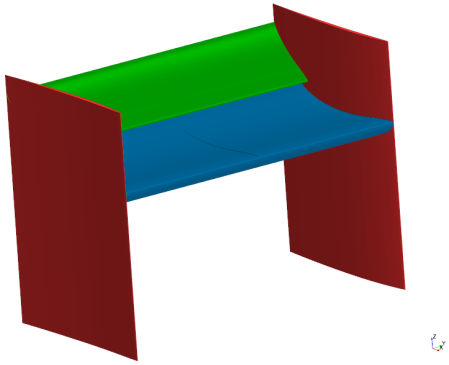

(c) Low drag wing with larger endplate

Figure 5.1: Various low drag iterations.

Fig. 5.2 shows a more precise comparison of the reason behind these changes. The low drag design yields lower pressure values due to its placement higher up, away from the driver's wake. However, the increase in the pressure differential is not enough to compensate the lack of a third wing element. While cornering, the bigger endplate span reduces the downforce losses, as it reduces the wing's sensitivity to yaw.

Following these initial simulations, an analysis into what possible weight reduction could be done to the vehicle by having lower drag was made. This proposal intended to evaluate how much weight could be reduced on both the battery and the aerodynamic package. Table 5.2 shows the influence in both energy consumption, weight and score that this design could give. No meaningful changes in weight were able to be achieved as the reduction in aerodynamic drag only lowered the energy consumption by 1.2%, which, considering a constant battery energy density, only yields a 1.2% reduction in battery weight. This concept also does not give any improvement to the vehicle score over the competition, questioning its value even further.

A small sensitivity analysis was also made, shown in table 5.2, in order to evaluate why this concept did not show any improvements. The large vehicle mass was deemed as the most likely cause. The FST10e was one of the heaviest cars at Formula Student Germany (FSG) 2021 and this limitation makes further developments of a low drag concept fruitless as no meaningful energy consumption gains can be made if a car is this heavy.

Table 5.1: Performance comparison of a low drag rear wing concept in different operating conditions.

| Operating Condition | Straight Line | | | Curve | | |
|---|---|---|---|---|---|---|
| | $C_LA$ ($m^2$) | $C_DA$ ($m^2$) | $-C_LA/C_DA$ | $C_LA$ ($m^2$) | $C_DA$ ($m^2$) | $-C_LA/C_DA$ |
| Baseline rear wing | 3.20 | 1.51 | 2.12 | 3.08 | 1.46 | 2.11 |
| Low drag rear wing | 2.90 (-9%) | 1.20 (-21%) | 2.43 (+15%) | 2.93 (-5%) | 1.17 (-20%) | 2.50 (+18%) |
| Low drag rear wing w/ larger endplate | 2.92 (-9%) | 1.20 (-21%) | 2.44 (+15%) | 2.95 (-4%) | 1.17 (-20%) | 2.51 (+19%) |

Table 5.2: Expected energy loss from various car configurations.

| Configuration | **Car mass (kg)** | | $-C_LA$ ($m^2$) | | $C_DA$ ($m^2$) | | **Endurance energy consumption (kWh)** | |
|---|---|---|---|---|---|---|---|---|
| Baseline | 233 | | 3.20 | | 1.51 | | 7.04 | |
| Low drag | 233 | (-0%) | 2.90 | (-9%) | 1.20 | (-21%) | 6.96 | (-1%) |
| Baseline -10kg | 223 | (-4%) | 3.20 | (-0%) | 1.51 | (-0%) | 6.91 | (-2%) |
| Low drag -10kg | 223 | (-4%) | 2.90 | (-9%) | 1.20 | (-21%) | 6.80 | (-4%) |
| Baseline -20kg | 213 | (-9%) | 3.20 | (-0%) | 1.51 | (-0%) | 6.77 | (-4%) |
| Low drag -20kg | 213 | (-9%) | 2.90 | (-9%) | 1.20 | (-21%) | 6.65 | (-6%) |

## 5.2 High downforce concept

Following the results found in Chap. 3, a high downforce concept was explored. The goal of this design was to maximize the vehicle downforce while having a maximum of $C_DA = 2.0$, so as not to reduce the vehicle's acceleration significantly.

In order to achieve this, the following improvements were made:

- Usage of a curved rear wing main plane profile;
- Wing cascade optimization;
- Increase in the endplate size;
- Changed the endplate geometry from flat to curved;

### 5.2.1 Geometries

Figures 5.3, 5.4, 5.5 and 5.6 illustrate the various geometries that were simulated. They can be subdivided in two sets: the first one, where only the curved main plane and wing cascade were iterated, Figs. 5.3(a) to 5.4(f); and the second one, where the endplate size and curvature were changed, as well as some final cascade optimizations, Figs. 5.5(a) to 5.6(b). The changes in the first set were focused on maximizing the wing's downforce generating capabilities by both

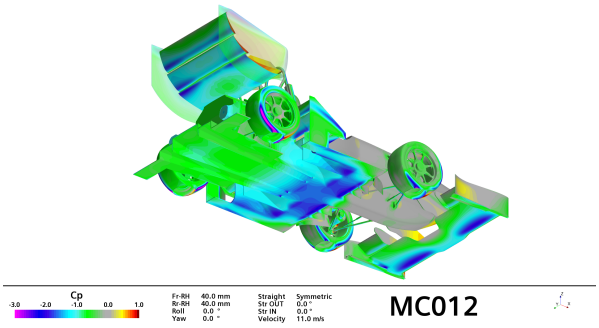


(a) Baseline rear wing

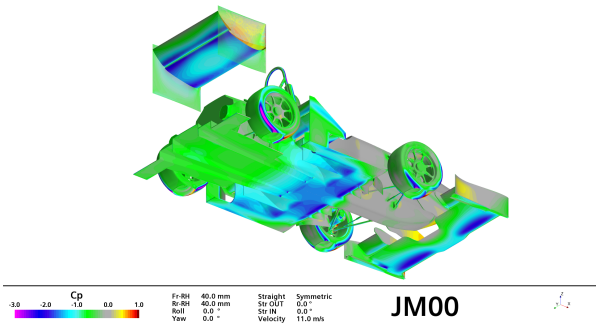


(b) Low drag rear wing

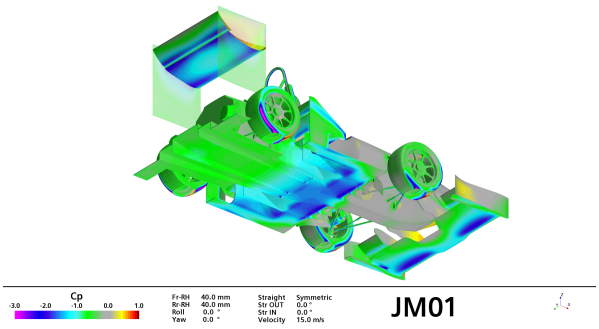


(c) Low drag rear wing with larger endplate

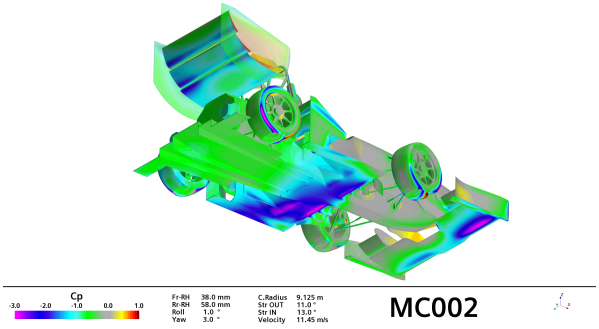


(d) Skidpad

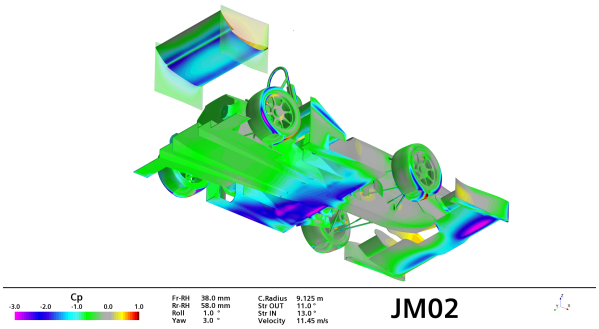


(e) Skidpad configuration with low drag rear wing

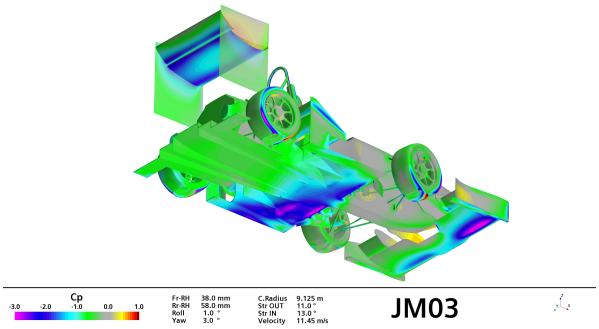


(f) Skidpad configuration with low drag rear wing and larger endplate endplate

Figure 5.2: Surface pressure coefficient distribution of the initial simulation batch.

increasing its chord, using all the available space allowed by the regulations, and changing its placement in order to avoid the low energy air and wake region caused by the pilot and head restraint. All the rear wing flap configurations can be seen in Fig. 5.7.

Geometries 1 and 2, Figs. 5.3(a) and 5.3(b) respectively, were the first attempts at the curved main plane design, in these designs the total wing chord was preserved, however the curvature was slightly increased, due to the usage of the MSHD airfoil in the main plane as opposed to the S1223 airfoil in the old design. From there on, geometries 3 to 10, Figs. 5.3(c) to 5.4(f), the focal point was optimizing the rear wing cascade by changing the flap gap, overlap and Angle of Attack (AoA).

Geometry 11, Fig. 5.5(a) focused on increasing the endplate size and shape, according to the results obtained in [6], so as to maximize the pressure gradient between the wing's upper and lower surfaces. This concept was then followed up by geometry 12, Fig. 5.5(b), where a rearward section of the endplate was cut in order to reduce the tip vortex intensity, thus lowering

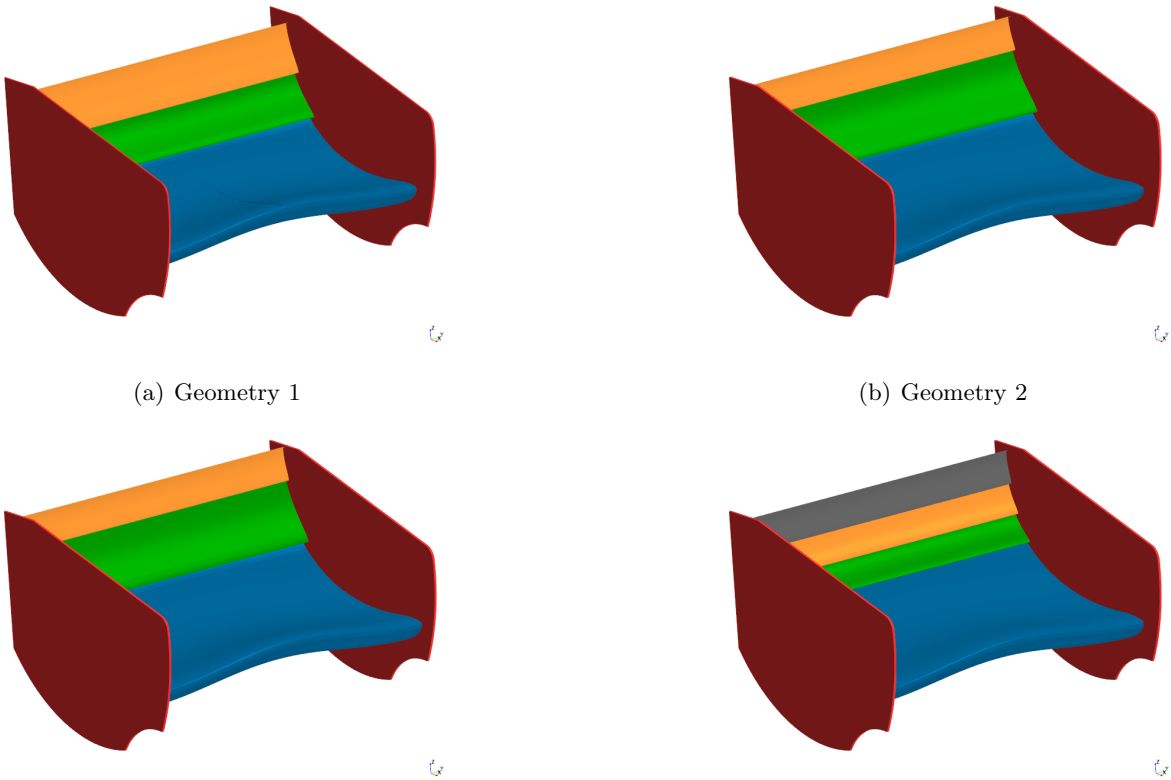

(a) Geometry 1

(b) Geometry 2

(c) Geometry 3

(d) Geometry 4

Figure 5.3: Different curved main planes and flap configurations.

the drag.

The last set of geometries, Figs. 5.5(c) to 5.6(b), a final main plane camber change was made to reduce flow separation in its middle section, then airfoil-like endplates were tested to further increase the low pressure region in the wing's suction side. Geometry 14's endplates were based on the NACA 4405 airfoil, while geometries 15 to 17 used the NACA 6402 airfoil, finally a smoother leading edge was used on the last two geometries to prevent flow separation on the outer section of endplate.

### 5.2.2 Results

Tables 5.3 to 5.6 as well as Figs. 5.8 to 5.14 show the major data points that were analysed in order to make the wing design decisions.

From the first set of iterations onwards, it was clear that the curved wing design yielded greater downforce values than the current one. A 4% increase in the vertical load was immediately verified, mostly due to the change in the main plane's profile, as the MSHD airfoil created a significantly lower pressure area in the wing's suction side. The increase in the rear wing curvature due to the new airfoil and flap placement was also created a 6% increase in total drag.

The addition of a third rear wing flap, placed almost vertically was also one of the biggest factors that led to the increase in the aerodynamic loads generated by the wing and the car itself. As previously mentioned in Sec. 2.2, due to the rear wing being placed at least 70cm above the road, no meaningful aerodynamic gains are able to be obtained through ground effect, thus, large wing curvatures are necessary to generate significant enough loads. The inclusion of

this new flap accomplished this exact goal, with the penalty of some added drag.

Figs. 5.8(a) to 5.8(g), as well as, 5.8(b) to 5.8(h) illustrate these points clearly. When observing the wing's pressure side, the increase in incidence had the consequence of increasing the surface $C_P$ in the pressure side, creating a greater horizontal pressure differential, therefore increasing drag. Although, when observing the suction side, it is also visible that larger and much lower pressure zones were created. This increase in pressure in the upper side combined with the decrease in the lower side, are the sources of the added vertical aerodynamic loads.

Table 5.3: Full car and rear wing aerodynamic loads from the first set of geometries.

| **Simulation** | Baseline | 1 | | 2 | | 3 | | **4** | |
|---|---|---|---|---|---|---|---|---|---|
| $-C_LA$ Total ($m^2$) | 3.20 | 3.26 | (+2%) | 3.32 | (+4%) | 3.30 | (+3%) | **3.36** | **(+5%)** |
| $C_DA$ Total ($m^2$) | 1.51 | 1.55 | (+2%) | 1.61 | (+7%) | 1.59 | (+5%) | **1.62** | **(+7%)** |
| $-C_LA$ RW ($m^2$) | 1.02 | 1.09 | (+7%) | 1.12 | (+10%) | 1.08 | (+6%) | **1.14** | **(+12%)** |
| $C_DA$ RW ($m^2$) | 0.57 | 0.60 | (+5%) | 0.64 | (+12%) | 0.63 | (+11%) | **0.63** | **(+11%)** |

Proceeding to the next set of geometries, 5 to 10, where the wing cascade was optimized through changes in the flap gap and overlap, no meaningful changes were observed. As can be seen in figures 5.9(b) to 5.10(f), most of the modifications that were made just shifted the pressure distribution slightly forwards or rearwards, depending on what change was made. From these iterations, only geometry 7, illustrated in Figs. 5.9(e) and 5.9(f) stands out. In this geometry all the flap overlap and gap values were slightly reduced in order to better align the flap suction peak with the previous' element takeoff angle. This idea proved to be slightly less effective than initially thought, yielding a less than 1% increase in downforce and a 3% increment in the drag. Even though the performance increase was not significant, this cascade was still chosen as a baseline for the changes in the endplates, as its pressure distribution was deemed to be the most favourable for such changes, due to its lower pressure region at the edges of its span.

Table 5.4: Full car and rear wing aerodynamic loads from the second set of geometries.

| **Simulation** | New Baseline | 5 | 6 | **7** | 8 | 9 | 10 |
|---|---|---|---|---|---|---|---|
| $-C_LA$ Total ($m^2$) | 3.36 | 3.36 (+0%) | 3.34 (-1%) | **3.38 (+1%)** | 3.36 (+0%) | 3.34 (-1%) | 3.33 (-1%) |
| $C_DA$ Total ($m^2$) | 1.62 | 1.64 (+1%) | 1.61 (-1%) | **1.66 (+2%)** | 1.65 (+2%) | 1.62 (-1%) | 1.59 (-2%) |
| $-C_LA$ RW ($m^2$) | 1.14 | 1.15 (+%) | 1.13 (-1%) | **1.16 (+2%)** | 1.14 (+0%) | 1.10 (-4%) | 1.10 (-4%) |
| $C_DA$ RW ($m^2$) | 0.63 | 0.67 (+6%) | 0.65 (+3%) | **0.66 (+5%)** | 0.69 (+10%) | 0.66 (+5%) | 0.63 (+0%) |

The first attempt at a better endplate design is illustrated in Fig. 5.12(b) and 5.12(a). The goal of this design was to better isolate the low pressure zone created in the wing's suction side by increasing the endplate span. This proved ineffective as the low pressure region was not large enough to benefit from this change, however due to the slight increase in $-C_LA$, the endplate size was kept, as its potential increase in performance could be found when changing to a cambered endplate design. Design 12 also did not show any increase in performance, as the vortex structures that were supposed to form did not have enough space to do so, ruining

any potential gains. The thirteenth iteration also showed marginal downforce gains, however it had a slightly more favourable pressure distribution, due to curvature changes in the central area of the main plane, allowing a reduction of the separation region created in the fourth wing element. This improved pressure distribution focused an even larger portion of the wing load near its endplates, which would be benefitial when changing to a curved endplate design, as the additional suction would enhance both components' performance.

Finally, design 14 was incorporated with curved endplates. The increase in the low pressure area was immediate, as well as the increase in rear wing performance. A downforce increase of 4% was generated, as well as a 4% increase in drag. The significant increase in drag was attributed to the increase in the frontal area of the endplate from 40 $cm^2$ to 320 $cm^2$. This design, however, still had some issues due to the thin endplate leading edge, significant flow separation was observed in the outer sections of the endplates, increasing drag, thus lowering the wing's efficiency. The increase in camber from the change in endplate airfoil from NACA 4405 to NACA 6402 was immediately beneficial to geometry 15, as seen in Fig. 5.13(d) where the lower pressure region was further expanded, increasing the wing's efficiency.

The last two geometries were focused on reducing the aforementioned flow separation near the endplate's leading edge. As seen in Fig. 5.11(a), a significant low energy region was being formed due to the misalignment of the leading edge and the incoming airflow. To fix this issue, a smoother leading edge was developed. This would allow the endplate to work at a larger range of incidence and reduce its form drag. This change can be seen in Fig. 5.6(a), even though the endplate tip is pointed outwards, its roundness reduced the separation region significantly, as can be seen in Fig. 5.11(b). This also increased the wing's downforce by 3%, while reducing its drag marginally, a significant improvement over previous major design changes, where each increase in vertical load was also accompanied by a proportional increase in the drag force. The last geometry intended to further refine the leading edge alignment. A 6% reduction in drag was achieved, however the previous downforce gains were lost.

Geometry 16 was deemed to be the best performing one and as such it would be the one built and tested in the wind tunnel. The wind tunnel testing campaigns intend to assess both the wing's straight line and curve performance, as the biggest gains against a flat endplate design are expected to happen during cornering.

Using the new $-C_LA$ and $C_DA$ values in the point mass simulator, a $\Delta Score = 6$ would be expected with this new car configuration.

Table 5.5: Full car and rear wing aerodynamic loads from the third set of geometries.

| Simulation | New Baseline | 11 | | 12 | | 13 | | 14 | | 15 | |
|---|---|---|---|---|---|---|---|---|---|---|---|
| $-C_LA$ Total ($m^2$) | 3.38 | 3.38 | (+0%) | 3.36 | (-1%) | 3.39 | (+0%) | 3.41 | (+1%) | 3.43 | (+1%) |
| $C_DA$ Total ($m^2$) | 1.66 | 1.67 | (+1%) | 1.66 | (+0%) | 1.68 | (+1%) | 1.72 | (+4%) | 1.74 | (+5%) |
| $-C_LA$ RW ($m^2$) | 1.16 | 1.16 | (+0%) | 1.15 | (-1%) | 1.15 | (-1%) | 1.19 | (+3%) | 1.18 | (+2%) |
| $C_DA$ RW ($m^2$) | 0.66 | 0.70 | (+6%) | 0.69 | (+5%) | 0.70 | (+6%) | 0.74 | (+12%) | 0.73 | (+11%) |

Table 5.6: Full car and rear wing aerodynamic loads from the final set of geometries.

| Simulation | New Baseline | **16** | | 17 | |
|---|---|---|---|---|---|
| $-C_LA$ Total ($m^2$) | 3.38 | **3.47** | **(+3%)** | 3.43 | (+1%) |
| $C_DA$ Total ($m^2$) | 1.66 | **1.75** | **(+5%)** | 1.71 | (+3%) |
| $-C_LA$ RW ($m^2$) | 1.16 | **1.22** | **(+5%)** | 1.17 | (+1%) |
| $C_DA$ RW ($m^2$) | 0.66 | **0.73** | **(+11%)** | 0.69 | (+5%) |

### 5.2.3 Yaw angle simulation analysis

An analysis of the rear wing and car performance while the oncoming flow was at an angle with the vehicle was made in order to estimate the cornering performance. As can be seen in Tab. 5.7, the new rear wing concept reduces the wing downforce losses at higher yaw angles from 25% to 18%, while slight increasing to 3% the loss of load at lower yaw angles.

This characteristic should cause a slight increase in the vehicle cornering performance as a larger amount of downforce is preserved during these conditions.

A larger amount of vehicle drag is also shed while in cornering, going from 9% to 11%, although the rear wing does not seem to be the cause of this reduction as the overall reduction in rear wing drag was approximately 0.05 $C_DA$ in both cases.

Table 5.7: Comparison of the yaw angle results between the baseline and new concept cases.

| **Baseline** | | | | | | |
|---|---|---|---|---|---|---|
| **Yaw Angle (°)** | 0 | 2 | 4 | 6 | 8 | 10 |
| $-C_LA$ Total ($m^2$) | 3.20 | 3.12 | 3.07 | 2.98 | 2.89 | 2.83 |
| $C_DA$ Total ($m^2$) | 1.51 | 1.53 | 1.50 | 1.48 | 1.43 | 1.38 |
| $-C_LA$ RW ($m^2$) | 1.02 | 1.02 | 1.00 | 0.93 | 0.87 | 0.81 |
| $C_DA$ RW ($m^2$) | 0.57 | 0.58 | 0.57 | 0.55 | 0.54 | 0.51 |
| **New Concept** | | | | | | |
| **Yaw Angle (°)** | 0 | 2 | 4 | 6 | 8 | 10 |
| $-C_LA$ Total ($m^2$) | 3.47 (+8%) | 3.34 (+7%) | 3.28 (+7%) | 3.19 (+7%) | 3.11 (+8%) | 3.06 (+8%) |
| $C_DA$ Total ($m^2$) | 1.75 (+16%) | 1.68 (+10%) | 1.67 (+11%) | 1.65 (+12%) | 1.62 (+13%) | 1.57 (+14%) |
| $-C_LA$ RW ($m^2$) | 1.22 (+20%) | 1.19 (+17%) | 1.14 (+14%) | 1.16 (+25%) | 1.10 (+26%) | 1.03 (+27%) |
| $C_DA$ RW ($m^2$) | 0.73 (+28%) | 0.73 (+26%) | 0.71 (+25%) | 0.73 (+33%) | 0.70 (+30%) | 0.68 (+33%) |

## 5.3 Final Design

As aforementioned, the best performing design was geometry 16, shown in Figs. 5.14(a) and 5.14(b). This geometry is composed of: a 550 $mm$ chord main plane based on a custom-made

airfoil with 16° outer AoA and 11° inner AoA; Three 100 *mm* chord, S1223 airfoil-based flaps, at 50°, 68°, 83° of AoA respectivelly. A NACA 6402-based endplate with a smooth leading edge was also used to enhance the wing cascade performance. This design yielded a significantly lower suction peak and larger low pressure area than any other iteration, which in turn generated the largest amount of downforce. One of the key advantages of the curved main plane design can be clearly seen when observing this design's lower side, the middle section showed a significant increase suction, leading to increased vertical load. The endplate design was key for the increase in both straight line and curve scenarios, yielding a total vehicle downforce gain of (8%).

This design was then built and tested in a wind tunnel, the results of this testing campaign are shown in Chap. 6.

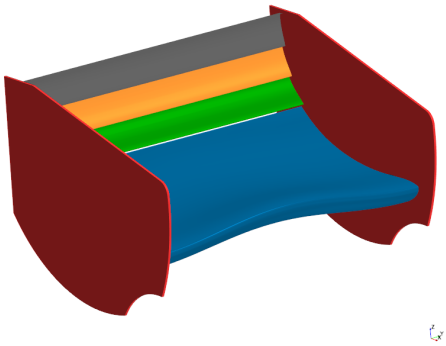

(a) Geometry 5

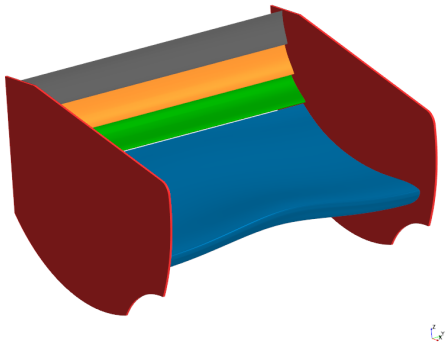

(b) Geometry 6

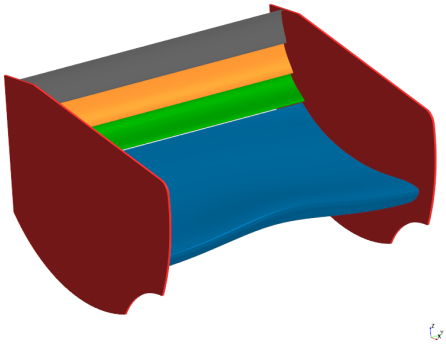

(c) Geometry 7

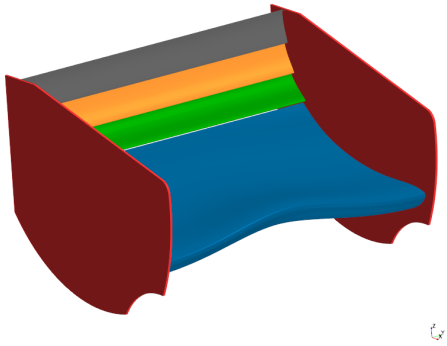

(d) Geometry 8

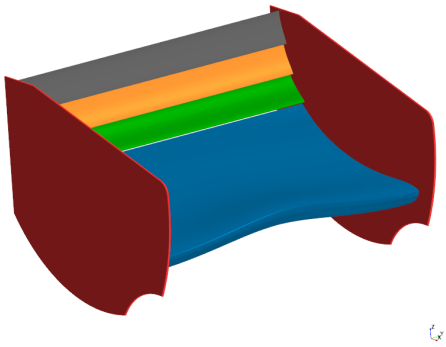

(e) Geometry 9

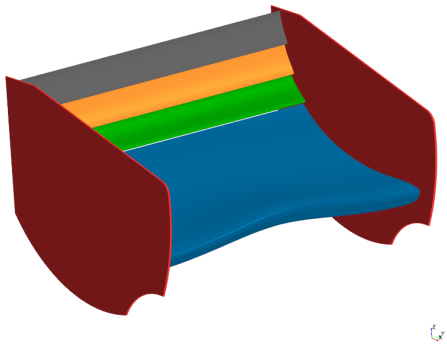

(f) Geometry 10

Figure 5.4: Different cascade gap, overlap and main plane optimizations.

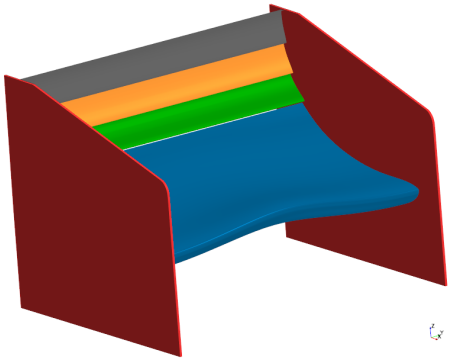

(a) Geometry 11

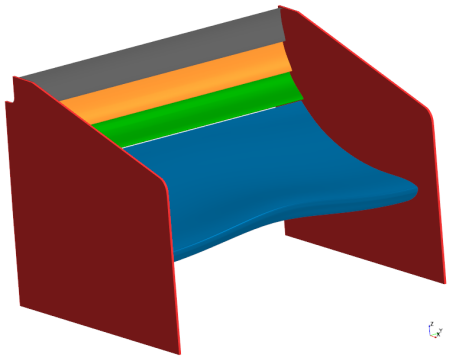

(b) Geometry 12

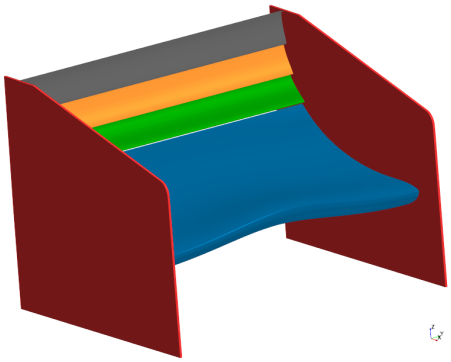

(c) Geometry 13

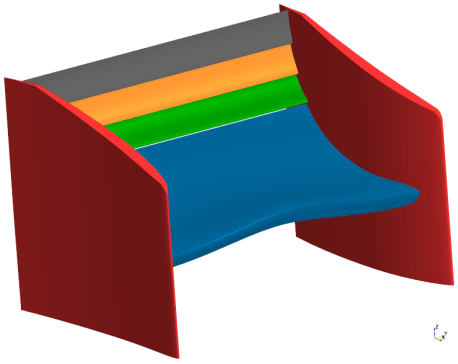

(d) Geometry 14

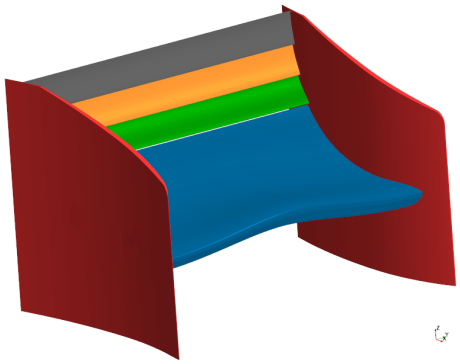

(e) Geometry 15

Figure 5.5: Different endplate sizes and shapes.

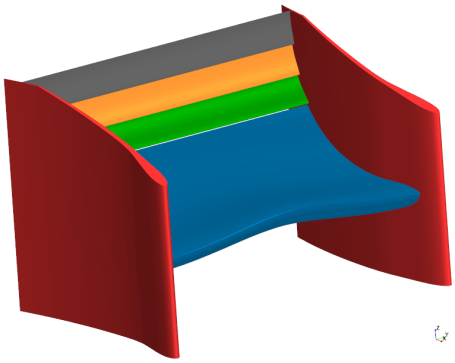

(a) Geometry 16

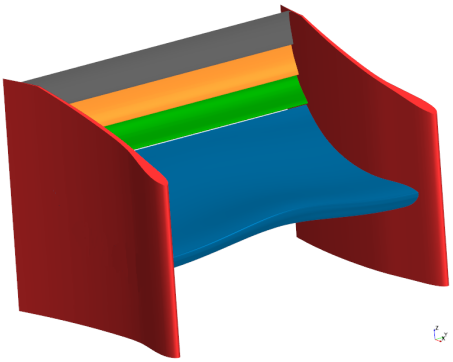

(b) Geometry 17

Figure 5.6: Final rear wing designs.

| Geometry | Main Plane | | | | 1st Flap | | | 2nd Flap | | | 3rd Flap | | | Endplate Format |
|---|---|---|---|---|---|---|---|---|---|---|---|---|---|---|
| | Chord (mm) | AoA outer section (°) | AoA middle section (°) | Airfoil | Chord (mm) | AoA (°) | Gap (mm) | Overlap (m) | Chord (mm) | AoA (°) | Gap (mm) | Overlap (m) | Chord (mm) | AoA (°) | Gap (mm) | Overlap (m) | |
| Baseline | 400 | 6 | 6 | S1223 | 200 | 36 | 20 | 40 | 200 | 61 | 20 | 20 | - | - | - | - | Flat |
| 1 | 500 | 15 | 5 | MSHD | 150 | 55 | 2 | 20 | 200 | 50 | 10 | 10 | - | - | - | - | Flat |
| 2 | 525 | 14 | 9 | MSHD | 200 | 59 | 0 | 25 | 100 | 77 | 0 | 13 | - | - | - | - | Flat |
| 3 | 560 | 14 | 9 | MSHD | 200 | 63 | 2 | 27 | 100 | 81 | 5 | 14 | - | - | - | - | Flat |
| 4 | 550 | 14 | 9 | MSHD | 100 | 50 | 1 | 16 | 100 | 68 | 0 | 14 | 100 | 83 | 0 | 13 | Flat |
| 5 | 550 | 14 | 9 | MSHD | 100 | 50 | 7 | 10 | 100 | 68 | 0 | 14 | 100 | 83 | 0 | 14 | Flat |
| 6 | 550 | 16 | 11 | MSHD | 100 | 50 | 6 | 11 | 100 | 68 | 0 | 15 | 100 | 83 | 0 | 14 | Flat |
| 7 | 550 | 16 | 11 | MSHD | 100 | 50 | 6 | 11 | 100 | 68 | 0 | 15 | 100 | 83 | -5 | 14 | Flat |
| 8 | 575 | 16 | 11 | MSHD | 100 | 52 | 6 | 11 | 100 | 70 | 0 | 15 | 100 | 85 | -5 | 14 | Flat |
| 9 | 550 | 16 | 13 | MSHD | 100 | 50 | 6 | 11 | 100 | 68 | 0 | 15 | 100 | 83 | -5 | 14 | Flat |
| 10 | 550 | 16 | 12 | MSHD | 100 | 50 | 6 | 11 | 100 | 68 | 0 | 15 | 100 | 83 | -5 | 14 | Flat |
| 11 | 550 | 16 | 11 | MSHD | 100 | 50 | 6 | 11 | 100 | 68 | 0 | 15 | 100 | 83 | -5 | 14 | Flat, Large |
| 12 | 550 | 16 | 11 | MSHD | 100 | 50 | 6 | 11 | 100 | 68 | 0 | 15 | 100 | 83 | -5 | 14 | Flat, Large, Small top cut |
| 13 | 550 | 16 | 11 | Custom-made | 100 | 50 | 6 | 11 | 100 | 68 | 0 | 15 | 100 | 83 | -5 | 14 | Flat and Large |
| 14 | 550 | 16 | 11 | Custom-made | 100 | 50 | 6 | 11 | 100 | 68 | 0 | 15 | 100 | 83 | -5 | 14 | NACA 4405 |
| 15 | 550 | 16 | 11 | Custom-made | 100 | 50 | 6 | 11 | 100 | 68 | 0 | 15 | 100 | 83 | -5 | 14 | NACA 6402 |
| 16 | 550 | 16 | 11 | Custom-made | 100 | 50 | 6 | 11 | 100 | 68 | 0 | 15 | 100 | 83 | -5 | 14 | NACA 6402, Smooth leading edge |
| 17 | 550 | 16 | 11 | Custom-made | 100 | 50 | 6 | 11 | 100 | 68 | 0 | 15 | 100 | 83 | -5 | 14 | NACA 6402, Smooth Forward-facing leading edge |

Figure 5.7: Rear wing design configurations

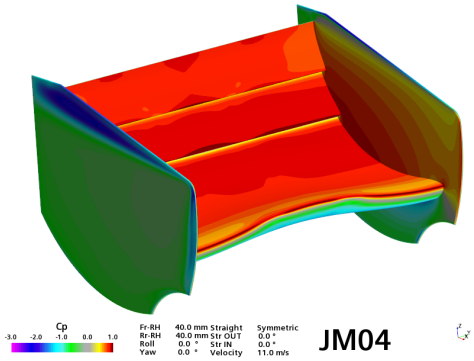


(a) Geometry 1 pressure side

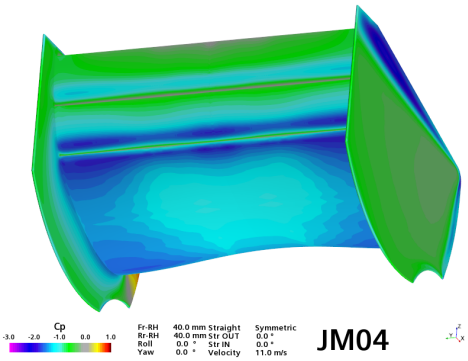


(b) Geometry 1 suction side

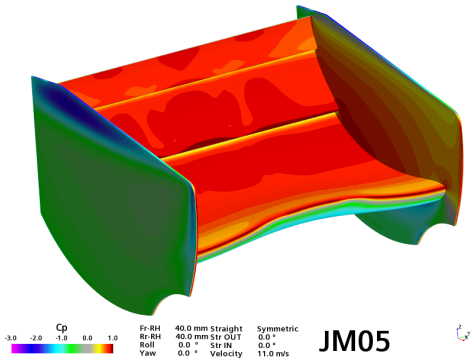


(c) Geometry 2 pressure side

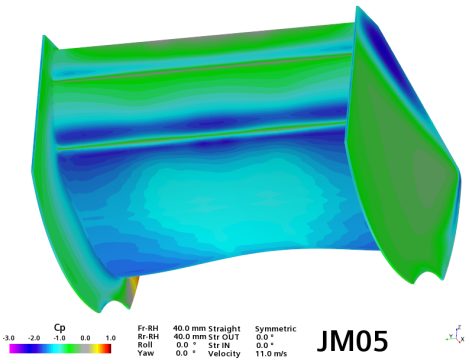


(d) Geometry 2 suction side

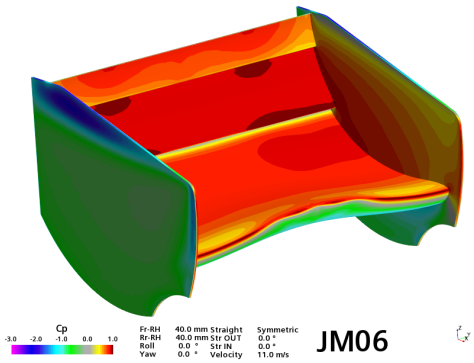


(e) Geometry 3 pressure side

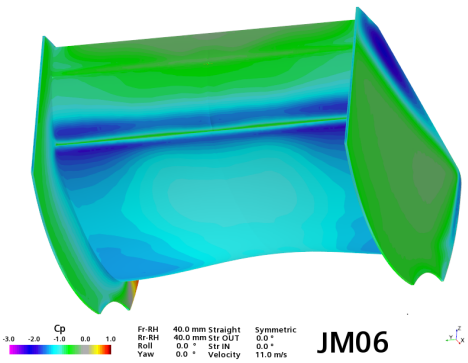


(f) Geometry 3 suction side

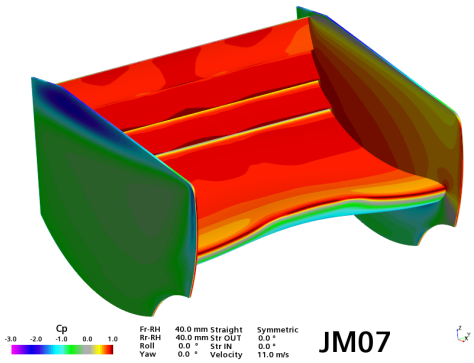


(g) Geometry 4 pressure side

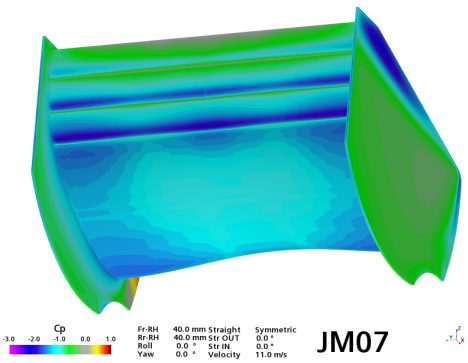


(h) Geometry 4 suction side

Figure 5.8: Initial set of geometries surface pressure coefficient.

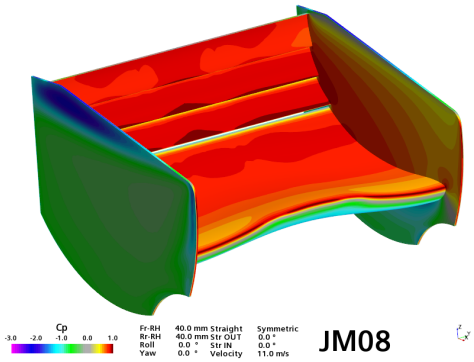


(a) Geometry 5 pressure side

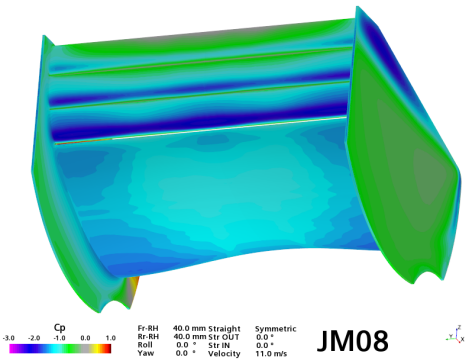


(b) Geometry 5 suction side

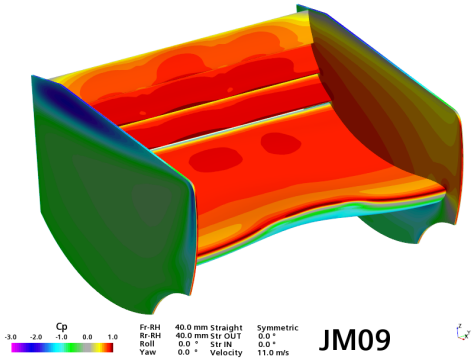


(c) Geometry 6 pressure side

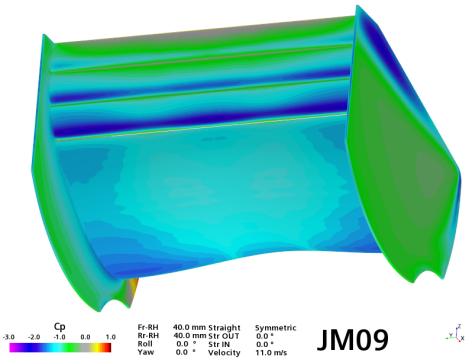


(d) Geometry 6 suction side

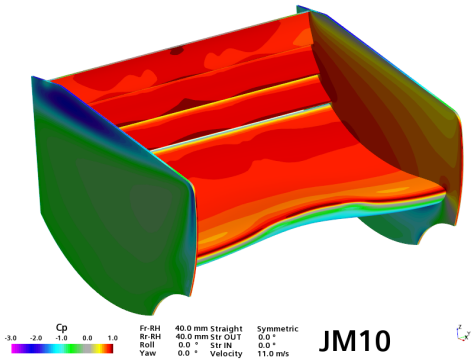


(e) Geometry 7 pressure side

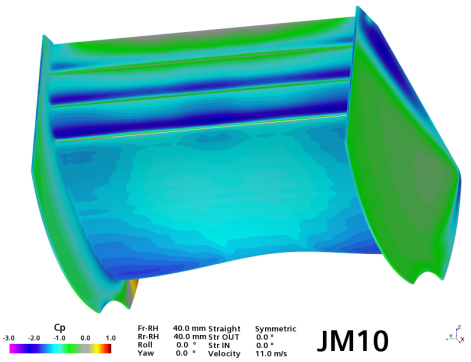


(f) Geometry 7 suction side

Figure 5.9: First part of the second set of geometries surface pressure coefficient.

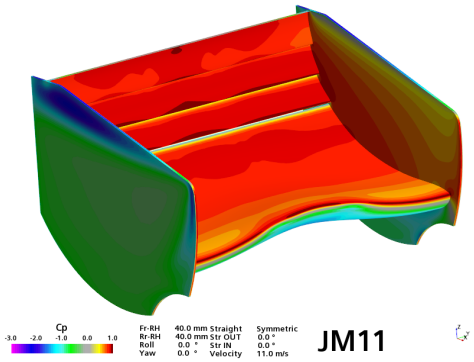


(a) Geometry 8 pressure side

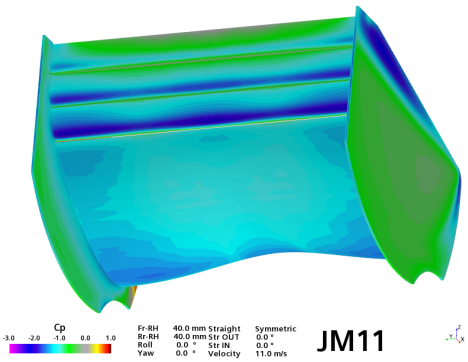


(b) Geometry 8 suction side

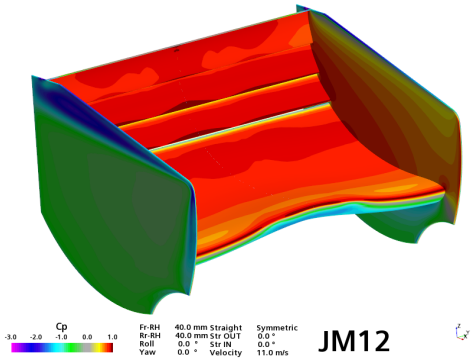


(c) Geometry 9 pressure side

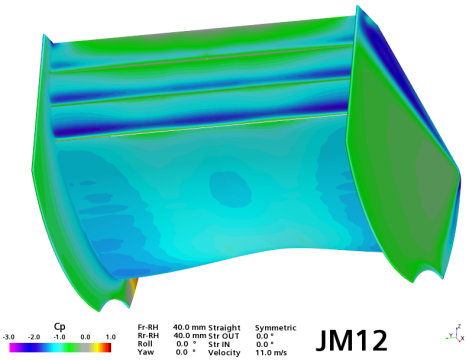


(d) Geometry 9 suction side

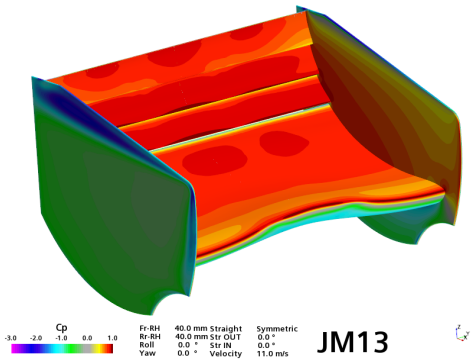


(e) Geometry 10 pressure side

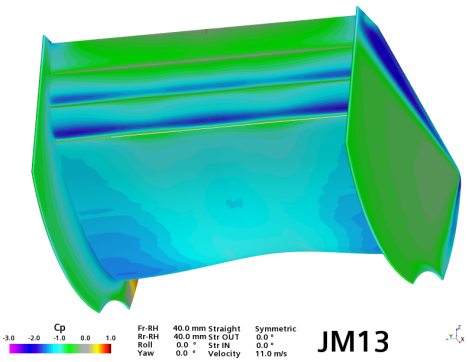


(f) Geometry 10 suction side

Figure 5.10: Second part of the second set of geometries surface pressure coefficient.


(a) Geometry 15

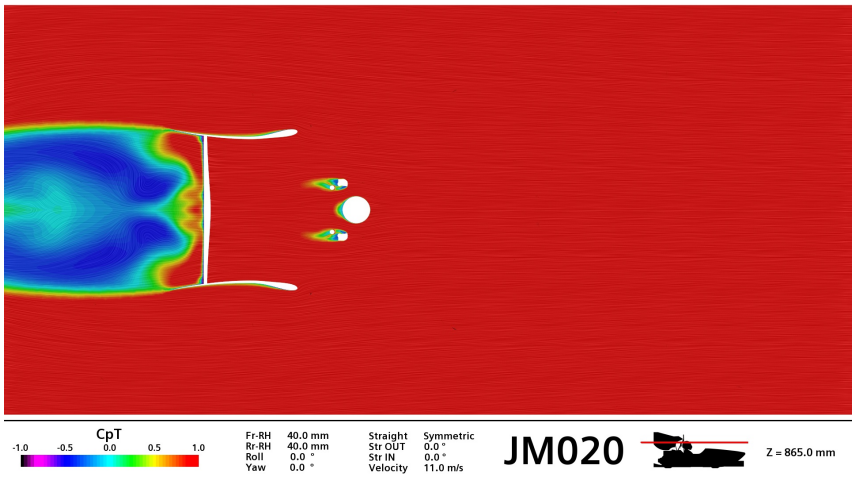


(b) Geometry 16

Figure 5.11: Total pressure coefficient at z = 875mm.

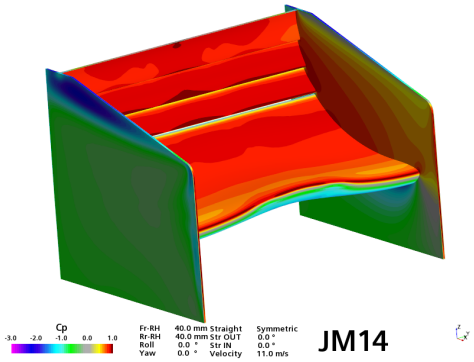


(a) Geometry 11 pressure side

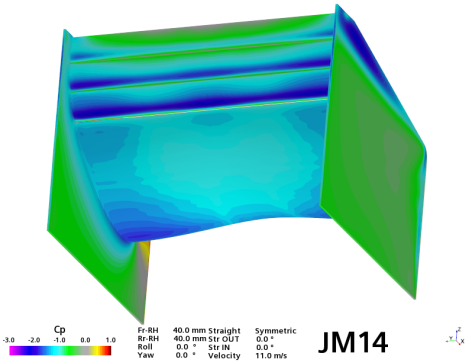


(b) Geometry 11 suction side

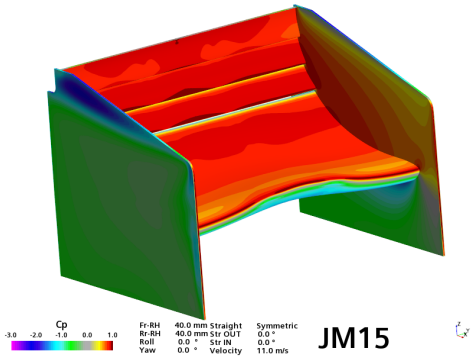


(c) Geometry 12 pressure side

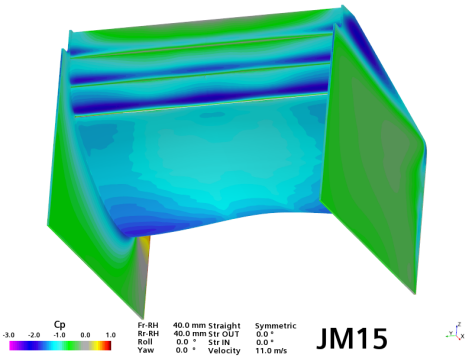


(d) Geometry 12 suction side

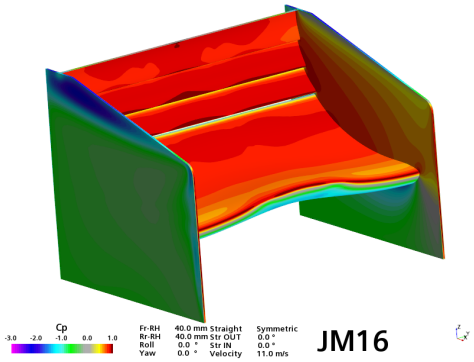


(e) Geometry 13 pressure side

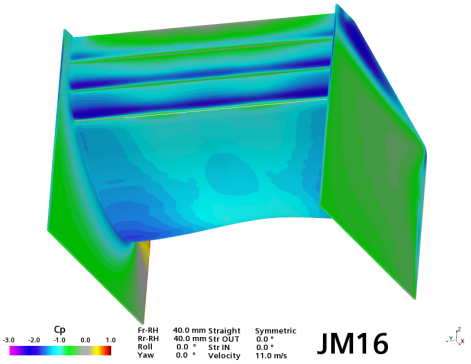


(f) Geometry 13 suction side

Figure 5.12: First part of the third set of geometries surface pressure coefficient.

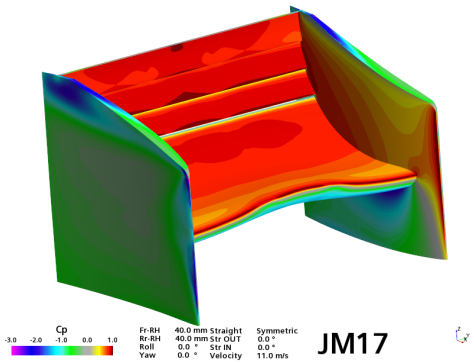


(a) Geometry 14 pressure side

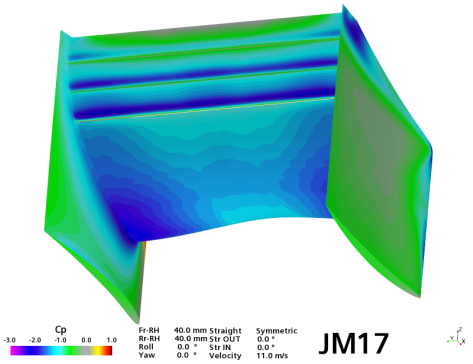


(b) Geometry 14 suction side

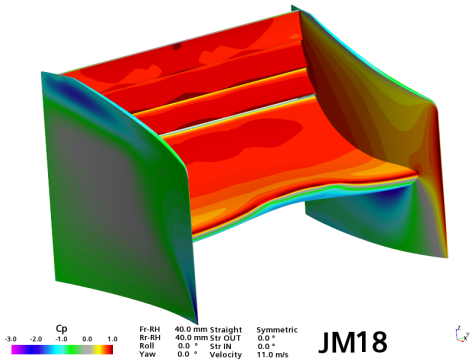


(c) Geometry 15 pressure side

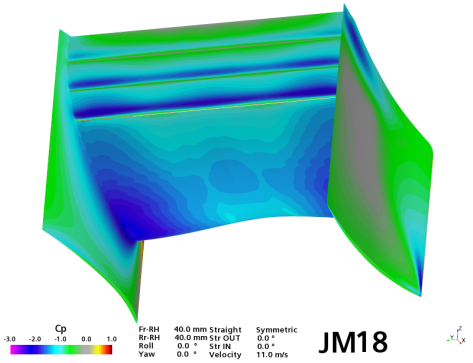


(d) Geometry 15 suction side

Figure 5.13: Second part of the third set of geometries surface pressure coefficient.

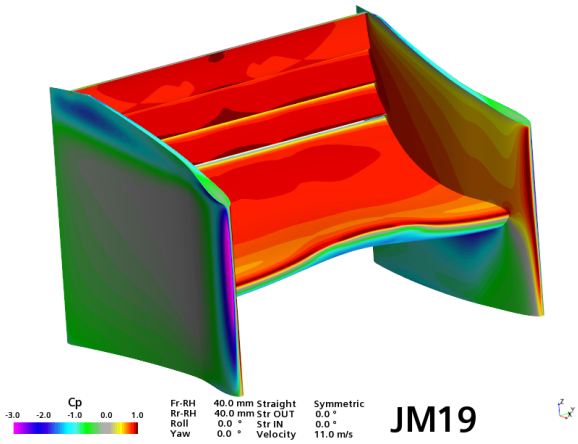


(a) Geometry 16 pressure side

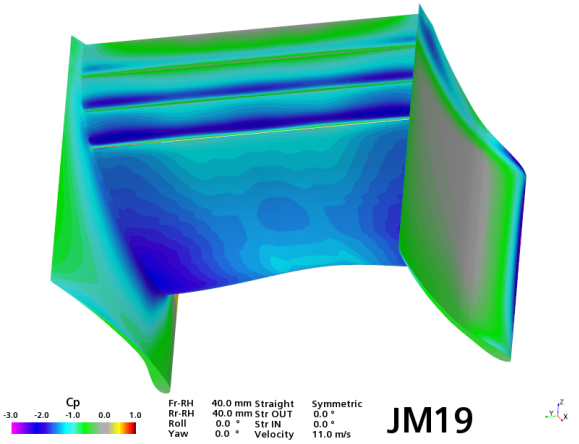


(b) Geometry 16 suction side

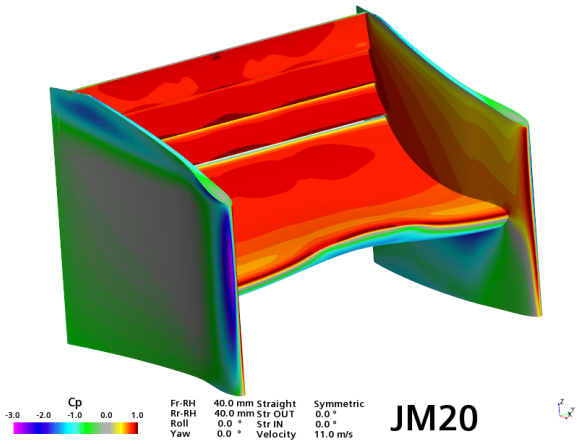


(c) Geometry 17 pressure side

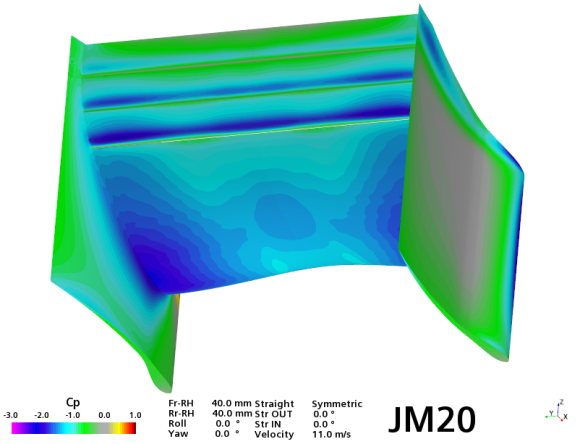


(d) Geometry 17 suction side

Figure 5.14: Final geometries surface pressure coefficient.

# Chapter 6

# Wind tunnel tests

In this chapter, a brief explanation of the wind tunnel testing procedure is given, followed by an analysis of the results, as well as a qualitative analysis through flow visualization. A comparison between the experimental and numerical results is also presented.

## 6.1 Experimental procedure

The experimental tests were executed in IST's aeroacoustic wind tunnel, located in the aerospace engineering laboratory. In order to best evaluate the performance difference between the two rear wings, a straight line case with lateral wind was chosen, which corresponds to the configuration where this component's performance varies the most.

The measurements were executed on the FST10e 1/3 scale model built in [29], using the same aerodynamic balance structure and measurement procedures. In order to preserve dynamic similarity between the real prototype and the scale model, a wind tunnel speed of $25m/s$ was chosen.

The first step in the experimental procedure was to screw the force balance to the wind tunnel ground and calibrate it. The process involved the usage of a calibration structure with movable pulleys, which is shown in Fig. 6.1. Weights were then suspended through these pulleys by a steel cable attached to the force balance in order to apply known loads and moments in all the axis.

Further optimizations were made from the calibration procedure used in [29]. The load cases used in the calibration of the moments were made using smaller values, as with this technique a higher sensitivity to small moment variations would be achieved. Additional weights were also used as preloads when placing the hooks, so that the steel cable would be completely stretched before placing the calibration loads, reducing the measurement error.

In order to execute the calibration, specific test cases were set, the tables with all the load cases that were used to calibrate the balance are available in Appendix A, as well as the order of when each weight was added. Three runs of each calibration case were made to reduce the measurement errors and have a more statistically significant amount of load cases. The procedure consisted of a waiting period of $30s$ followed by the addition of the hook to support the weights. These steps were then repeated while putting the desired weight on top of the hook until the maximum intended load was achieved. A correlation equation that relates all the forces and moments was created for each of the balance's bars. After this step, the model support structure was mounted inside the wind tunnel, replacing the calibration apparatus. The model

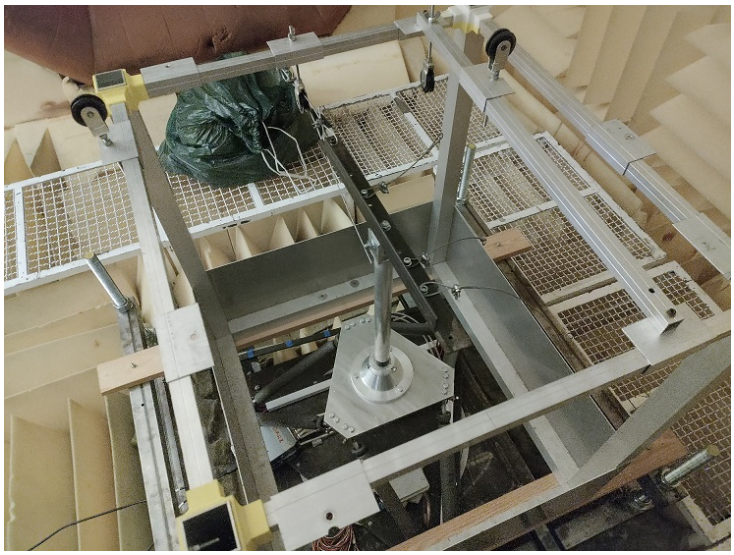

Figure 6.1: Force balance and its calibration structure mounted in the wind tunnel.

car was then placed on top of the balance and the structure was lifted into its final position, as seen in Fig. 6.2.

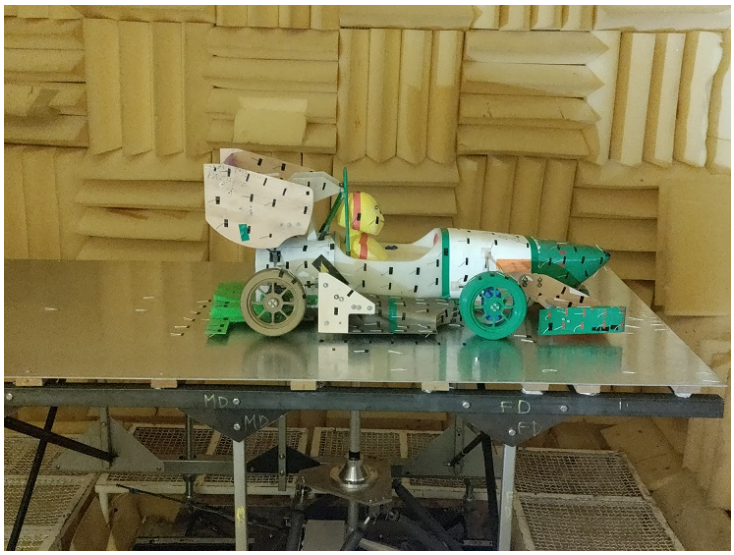

Figure 6.2: Model support structure and FST10e scale model placed inside the wind tunnel.

The extensometer data was acquired through two *NI 9237* DAQ modules into LabVIEW, where its change in extension was converted into the respective forces and moments. The final step was to process the measurement data. As the balance's measurements have a significant amount of noise, all presented data corresponds to the average of the values during a section of the $30s$ measurement period.

## 6.2 Baseline rear wing

The first measurement points were taken from the base FST10e in its maximum ride height configuration at $Yaw = 0°$, this step was meant to replicate the data from [29] and confirm that the calibration had been done correctly. After this confirmation, studies where the yaw

angle was changed from 2 to 10 degrees were made. The change in angle was made by rotating the aerodynamic balance in its rails and aligning the centerline of the nose of the car with a previously marked reference painted in the table, an example of the alignment process can be seen in Fig. 6.3.

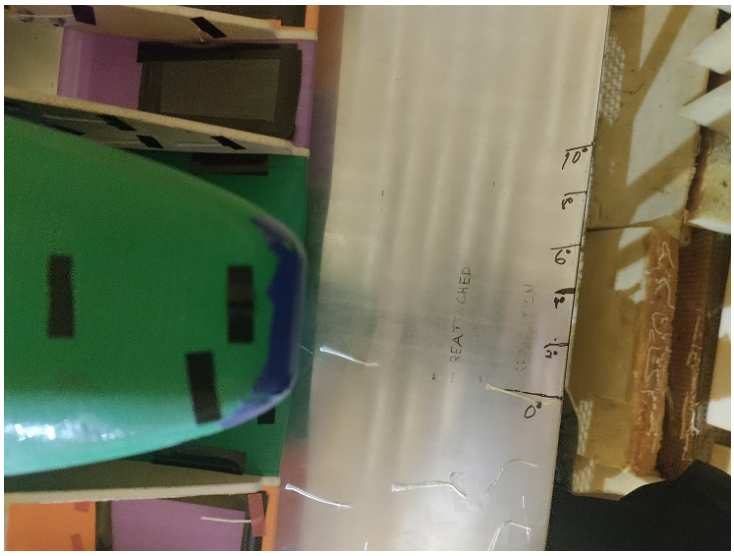


Figure 6.3: Yaw changing procedure.

The force and moment data from these measurements can be seen in Fig. 6.4. The force values experienced the same overall trend, however, as was also seen in previous measurements made in [29], the CFD data tends to overvalue $-C_LA$ and undervalue $C_DA$. The $C_YA$ plot also illustrates that the same trend was verified between the CFD results and wind tunnel measurements, although, in the $Yaw = 0°$ case, a larger then expected side force value was measured. As the car is placed in a straight line, the lateral loads from both sides are supposed to cancel each other out, leading to an almost null $C_YA$, this discrepancy in the results could be attributed to slight model or balance misalignments. A prevailing factor in this analysis was that at, $Yaw = 10°$, the offset between both cases tended to increase from approximately 6% to 10%, showing that the CFD model of the wind tunnel stops being reliable to assess the expected wind tunnel performance at higher yaw angles.

Regarding the moment values only the $CM_Y$ followed the CFD trend. The erratic behaviour from the roll and yaw moment coefficients matches with both the measurements made in [29] and the behaviour seen during the calibration of these components. During both cases, it was seen that some of the measurements were not large enough to leave the noise envelope of the previous calibration load. This hinders the balance's sensitivity, as the extensometer equations will be fed erroneous data, causing this behaviour.

## 6.3 New rear wing

When observing the measured data taken from the model with the new rear wing mounted, data which is illustrated in figs. 6.5, the same overall behaviours can be verified. The $-C_LA$ is still overestimated in the CFD, the $C_DA$ underestimated and the $C_YA$ also higher than expected, even at lower yaw values. Comparing the overall results with the base car model,

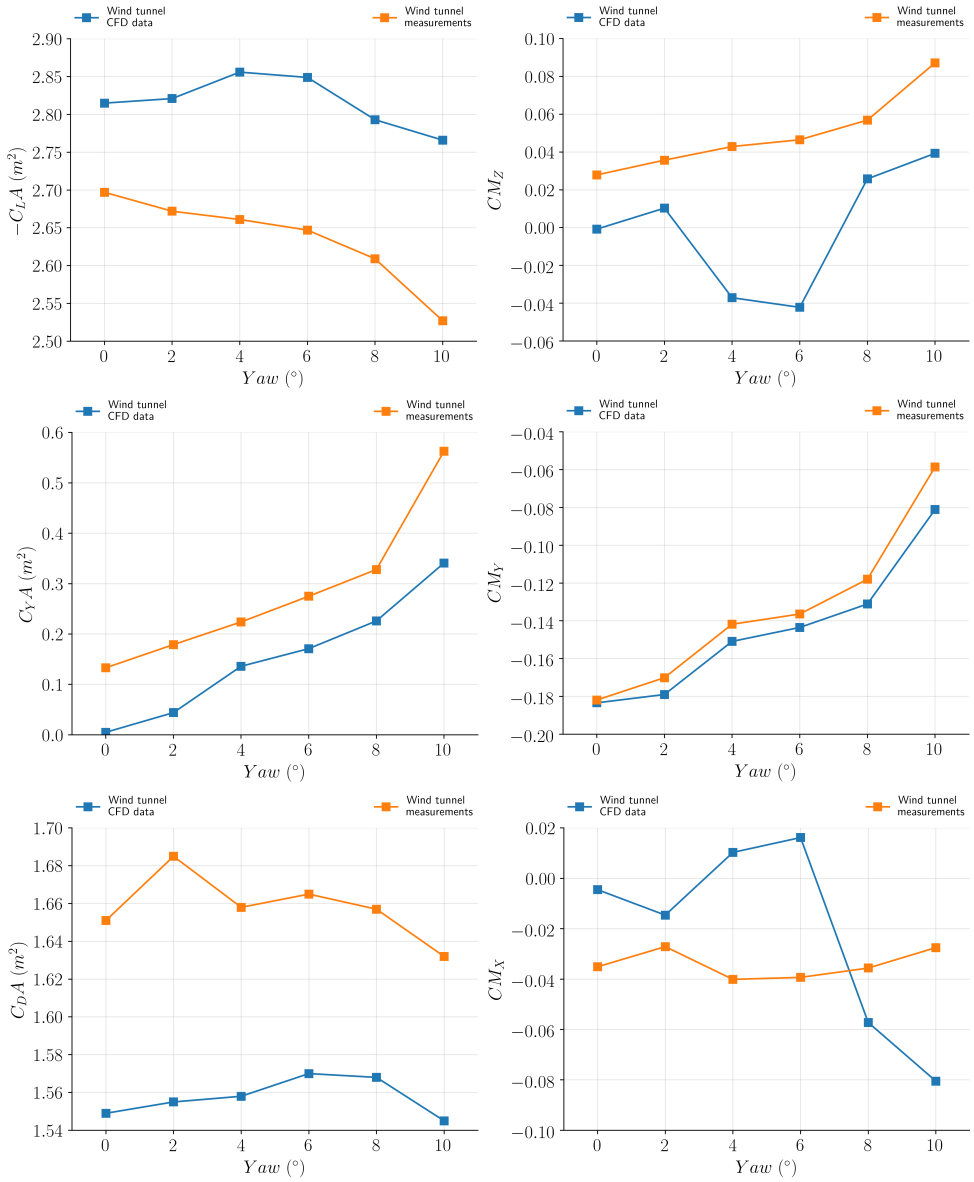


Figure 6.4: Base model force and moment comparison plots

the trend observed in Chap. 5 is also preserved, the new rear wing concept generates a higher vertical load and also higher drag.

The moment results presented a behaviour closer to what was expected, as opposed to the base model results. While the roll moment coefficient presented an inverse trend to what was observed in the simulations, the pitching moment and yaw moment coefficients showed a similar behaviour to the CFD trend. As no significant modifications besides changing the rear wing of the model were made, the shift in the results was unexpected, hinting that the calibration itself might not be such a large issue as aforementioned.

Comparing the wind tunnel experimental and CFD results to the track CFD results, it is clear that some large modifications still need to be done to the wind tunnel setup in order to better replicate the on-track conditions. Even though some of the force and moment trends still prevail from one type of study to the other, a discrepancy of up to 25% can still be verified in most of the measured parameters.

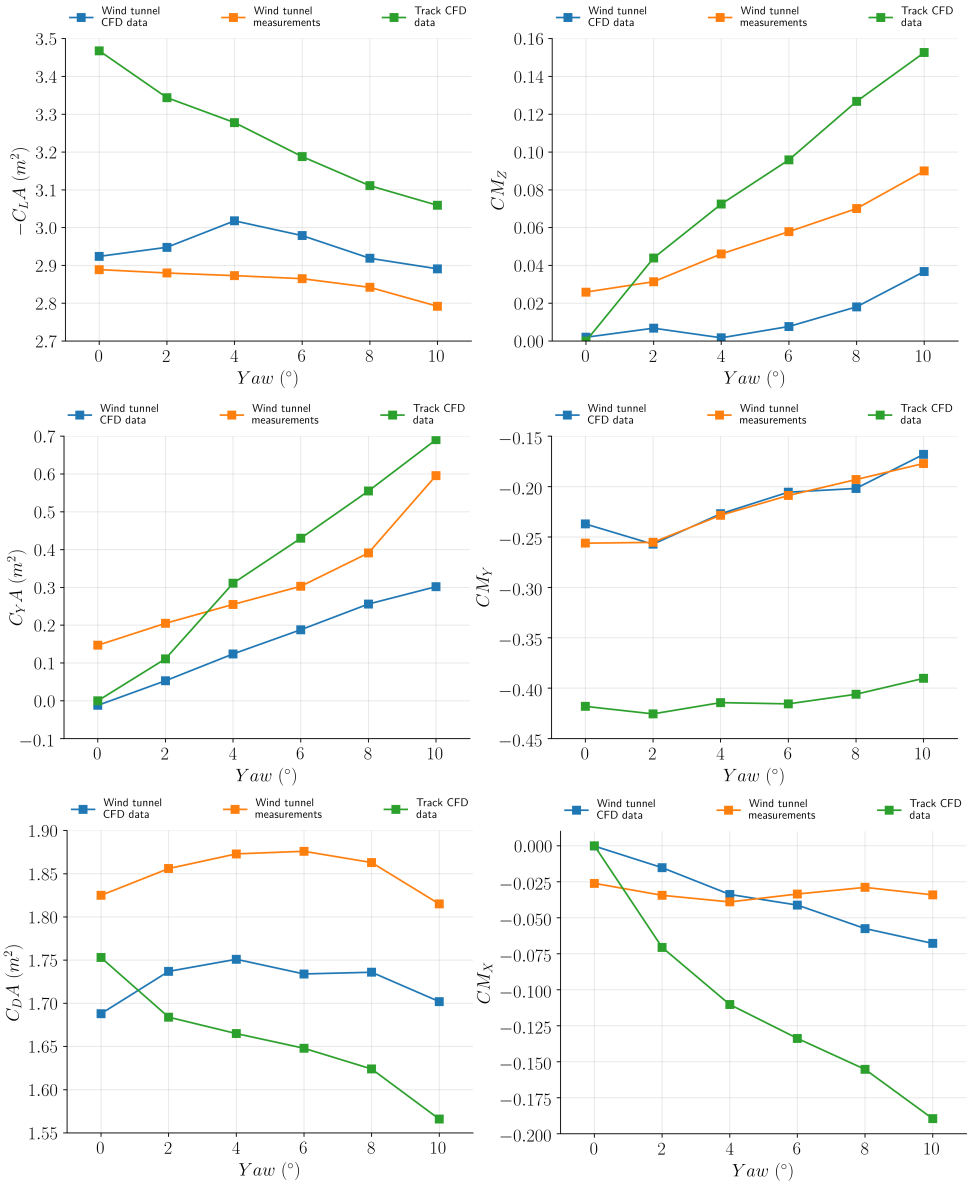


Figure 6.5: New rear wing force and moment comparison plots

## 6.4 Flow visualization

As the balance force data cannot yield the individual components contribution to the total aerodynamic loads, other methods are necessary to evaluate the performance of the rear wing. Wool tufts were glued to the wing's surface in order to visualize the airflow over it, as shown in Fig. 6.6. Following their placement, a video recording session where only the wool tufts were analysed was made. In order to not interfere with the force and moments measurements, due to the force balance being extremely sensitive to movement, this filming was made separately from the experiments shown in 6.3.

This method enables a qualitative evaluation of the behaviour of the boundary layer. However, it is highly limited in its scope as turbulence is a highly unsteady and multi-scale phenomenon which cannot be represented through a single image and can be filtered inadvertently by the size and placement of the tufts themselves.

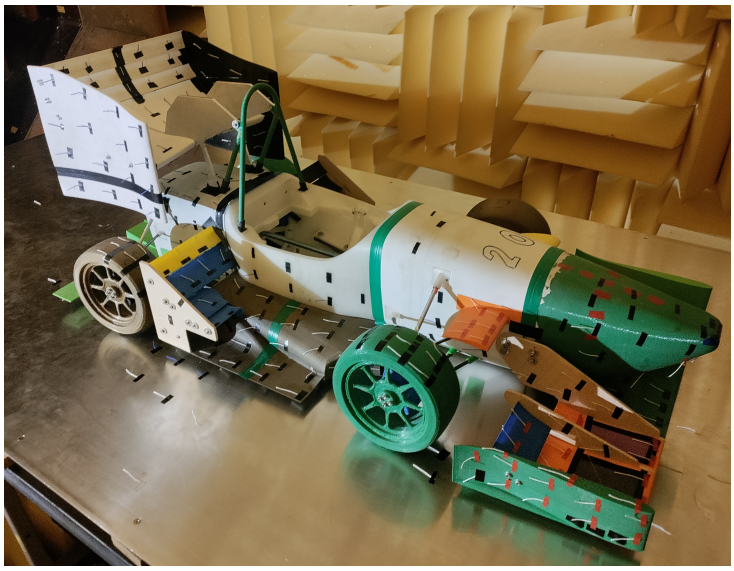

Figure 6.6: Wool tuft placement on the wind tunnel car model.

To compare these results to the numerical ones, images representing the skin friction over the longitudinal axis $x$ were made comprised of two high contrast colors: red, where $C_{fx} > 0$, representing the regions were the airflow was attached and blue, where $C_{fx} < 0$, showing the flow separation regions. Due to the limitations in comparison imposed by the wool tufts, only the longitudinal separation regions could be correctly assessed, as both 3D and transversal separations are exceptionally difficulty to spot through this method. Figures 6.7 to 6.10 depict the comparison between the EFD and CFD studies for 0° and 10° of yaw respectively.

### 6.4.1 0° Yaw

An initial analysis of the $Yaw = 0°$ results, as seen in the CFD plots, shows no significant separation regions within the cascade's suction side and the ones that were detected are too small to be seen with wool tufts. Turbulent boundary layers were clearly present in the whole rear wing, as even though attached to the surface, the wool tufts showed some movement, as can be seen in Fig. 6.7(a). When observing the endplate's airflow the same behaviour was captured in its inner region, marked as 1. A recirculation zone was created behind the first rear wing flap, causing the wool tuft to point backwards. The outer endplate region, marked as 2, did not present the same behaviour as anticipated, the separation region verified with the wool tufts was much larger than the one created in the numerical results. This discrepancy was probably caused by the higher turbulent intensity present in the oncoming wind tunnel jet, which tends to be dissipated in the CFD results due to its turbulence modelling.

Observing the pressure side of the wing, region number 2 and the extent of its associated separation region are much clearer. Comparing regions 3 and 4, the behaviour captured in the numerical simulations was not present in the experimental tests. As the rear wing is placed downstream of the vehicle, it is impacted by the flow structures generated by the components in front, as such, highly complex separation regions are commonly generated. This is exactly the case with the rear wing supports, as the pilot's head is placed directly in front of them, a large wake region is created which induces flow separation in the supports' inner section. This phenomenon could not be captured by the wool tufts and would require further flow visualization

tools to allow its study.

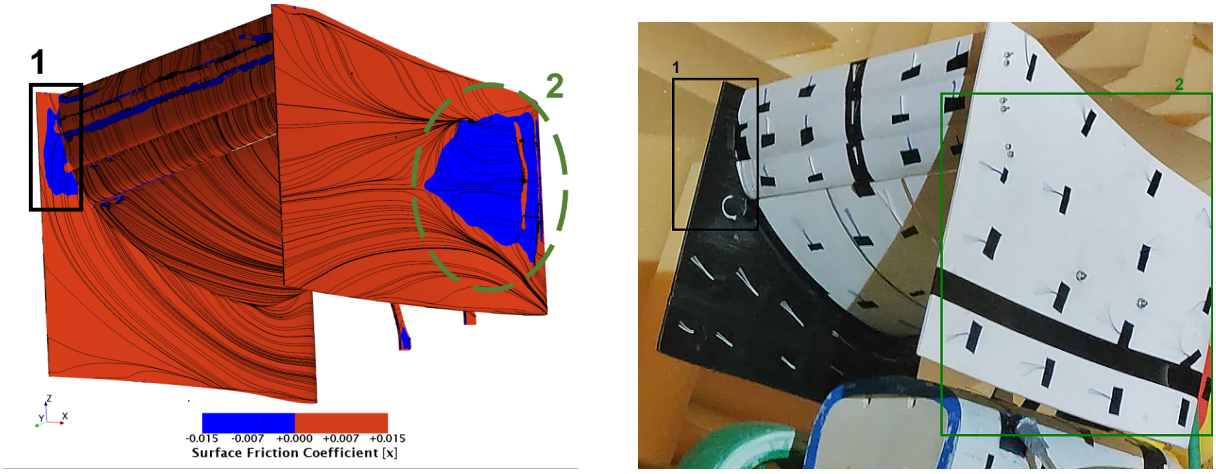


(a) CFD (b) EFD

Figure 6.7: Flow visualization of the suction side of the rear wing at $Yaw = 0°$.

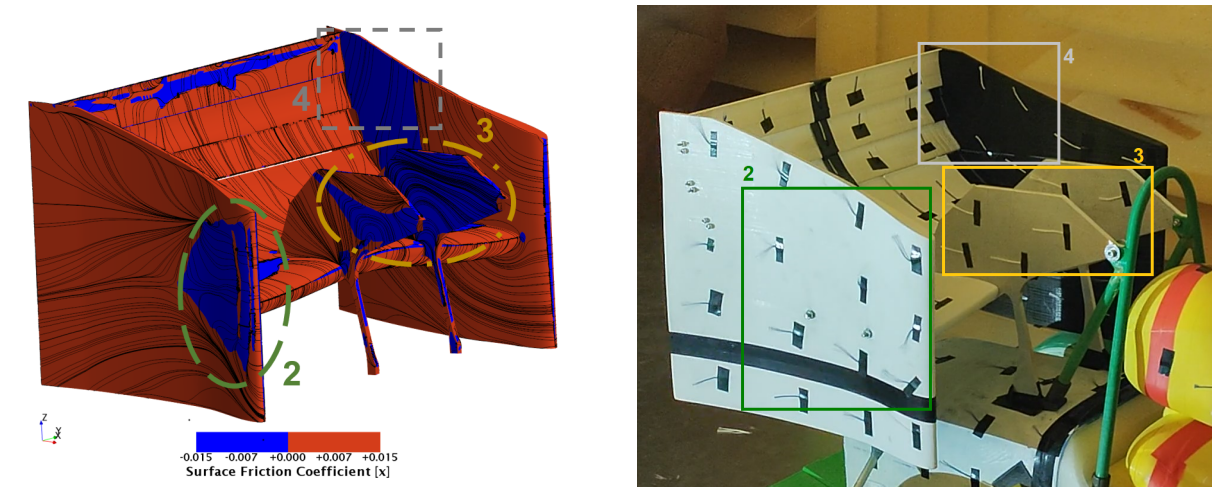


(a) CFD (b) EFD

Figure 6.8: Flow visualization of the pressure side of the rear wing at $Yaw = 0°$.

### 6.4.2 10° Yaw

As no significant changes in the rear wing's flow structures were present when doing small yaw steps, only the case with the largest yaw will be analysed. The comparison between the other CFD and EFD cases is available in Appendix B.

Comparing the previously mentioned separation regions, it can be seen in Fig. 6.9 that both regions 1 and 2 are smaller than what was verified in the $Yaw = 0°$ measurements. In the EFD results, shown in Fig. 6.9(b), neither of these two zones show any amount of separation. In region 1, this could be due to the separation area being too small to affect the movement of the wool tufts, however, in region 2, the lack of separation could be attributed to the aforementioned reason of the separations being transverse, which cannot be verified with wool tufts.

The small sections where separation is present on the rear wing cascade flaps were also not possible to detect as they were still too small.

Observing the pressure side of the wing in Fig. 6.10, it can be seen that, as in the suction side, much of the same behaviour was preserved. Region 4 still shows a behaviour too complex to assess with wool tufts. Region 3, however, shows a completely different behaviour in the CFD results as no significant separation regions were detected. The reason behind this trend shift was most likely due to the incoming airflow coming at angle with the vehicle, therefore reshaping the wake region created by the driver's head, which reduces the induced separation regions in the rear wing supports.

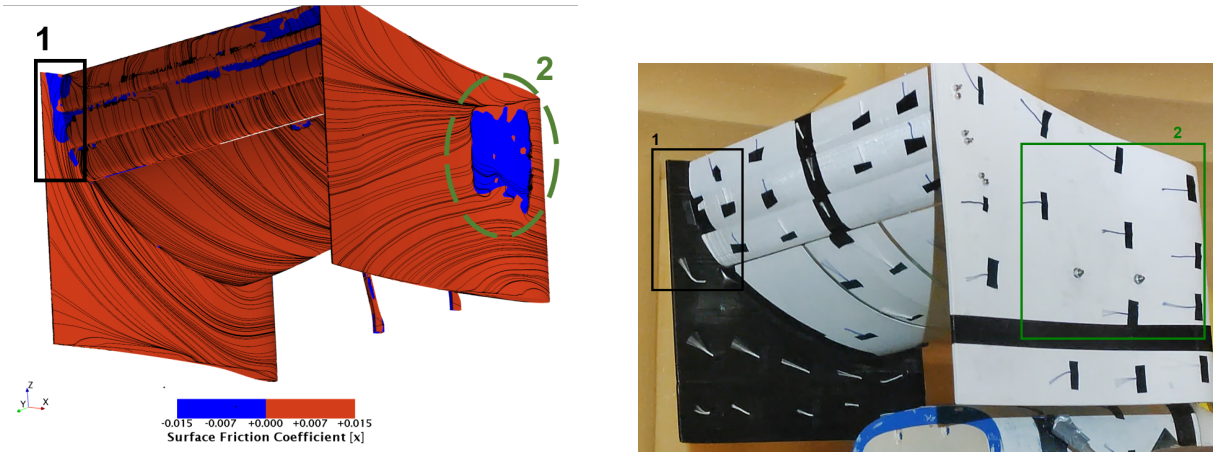


(a) CFD (b) EFD

Figure 6.9: Flow visualization of the suction side of the rear wing at $Yaw = 10°$.

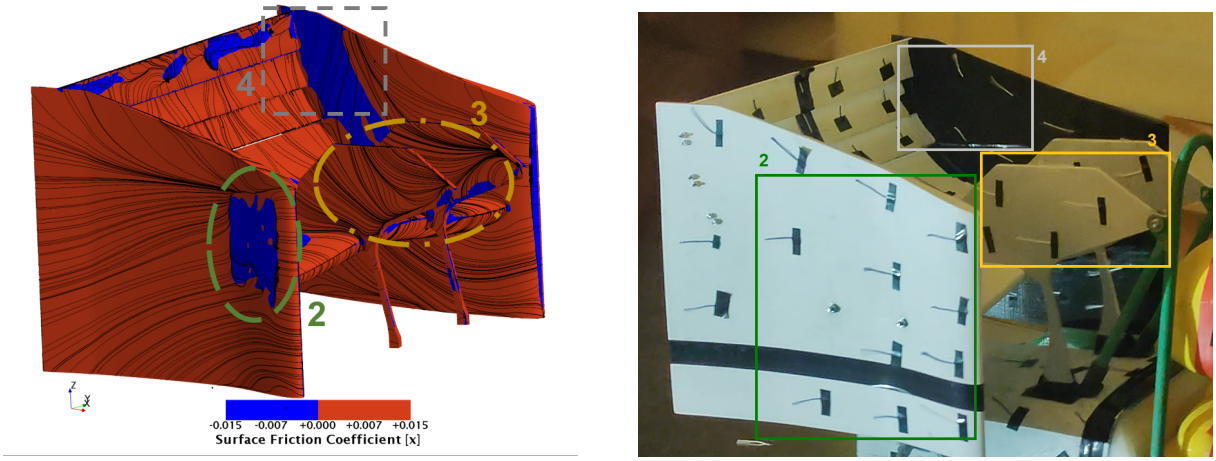


(a) CFD (b) EFD

Figure 6.10: Flow visualization of the pressure side of the rear wing at $Yaw = 10°$.

## 6.5 Test campaign main findings

From the testing campaign it was concluded that the new calibration procedure yielded better results, as the unpredictable moment behaviour seen in previous wind tunnel experiments was mostly eliminated.

The overall experimental trends were captured by the numerical results, however some limitations are still noticeable when comparing the wind tunnel results with the on-track CFD data.

The flow visualization methods applied were adequate at evaluating the surface streamlines of the rear wing main plane and outer section. However, the results obtained from the endplate inner section and flaps were inconclusive, meaning that other methods must be applied when analysis these zones in the future.

# Chapter 7

# Conclusions

## 7.1 Conclusions

The main goal of this thesis work was to develop and test a new rear wing concept based on a curved endplate design. To achieve this goal, initially, $C_LA$ and $C_DA$ targets were set with the aid of a point mass lap time simulator, which was upgraded in order to better fit this analysis and future aerodynamic models. This analysis showed that a Formula Student car's performance in a competition is predominantly influenced by its $C_LA$, due to the sinuous layout of the tracks.

A low drag rear wing concept was not a viable development option due to the high car mass. A much lighter car would need to built for this study, as the energy losses caused by the drag were not significant enough to yield any performance gains. A design approach based on this idea could still yield an increased score in the acceleration and efficiency events, but would it lose out on the remaining.

The high downforce rear wing concept yielded 20% increase in the rear wing's downforce, leading to a 8% increase in the overall vehicle vertical load. A 27% and 16% increase in rear wing and total car drag respectively was also verified. An expected increase in the Formula Student competition score of 6 points when compared to the baseline results would be expected when using this aerodynamic configuration.

This design showed to be even more efficient during cornering, as the yaw angle simulations showed 2% lower downforce losses than the baseline results. These result could still be further improved with better cascade and endplate interaction tuning.

Wind tunnel experiments of the rear wing exhibited the same overall force and moment trend that was observed in the numerical results. This, however, was not the case when comparing these with the track CFD results.

The wool tufts were not an optimal tool to visualize the separation and turbulent zones near the rear wing as they could not depict most of the behaviour that were present. It was still possible to verify that no longitudinal separation regions were created in the rear wing cascade. The outer section of the endplate does show a significant amount of separation at low angles of attack, while not affecting its downforce generating capabilities it does increase its drag.

## 7.2 Future work

A more complex vehicle dynamics model should be utilised for further studies. A 4-wheel lap time simulator would yield significantly better results, due to its capability to better model all the vehicle's dynamics. This new, more complex simulator would ease the implementation of any aerodynamic model, as car attitude is also considered and changed dynamically through the entirety of a lap.

Better modelling tools still need to be used both in the wind tunnel's numerical and experimental domains to better replicate the track results. Rotating wheels and a moving ground should be considered, as these changes to the boundary conditions will yield significant differences in the airflow surrounding the vehicle. Finer meshes should also be utilized in the computational domain, as some regions suffer from false diffusion and most of the vorticity is not correctly captured.

# Bibliography


[1] R. Li. *Aerodynamic Drag Reduction of a Square-Back Car Model Using Linear Genetic Programming and Physic-Based Control.* PhD thesis, ISAE-ENSMA Ecole Nationale Supérieure de Mécanique et d'Aérothécnique - Poitiers, 2017.

[2] M. Pfadenhauer. *Hochleistungsfahrzeuge*, pages 551–650. Springer Fachmedien Wiesbaden, Wiesbaden, 2013. ISBN 978-3-8348-2316-8. doi: 10.1007/978-3-8348-2316-8_9.

[3] S. Wordley and J. Saunders. Aerodynamics for formula sae: Initial design and performance prediction. In *SAE 2006 World Congress & Exhibition*. SAE International, April 2006. doi: 10.4271/2006-01-0806.

[4] Formula Student Germany's Website. 2022 rules v1.0. `https://www.formulastudent.de/fsg/rules/`, 2022. Last accessed $4^{th}$ of January 2022.

[5] Ecurie Aix's Website. eace09. `https://www.ecurie-aix.de/eace09`. Last accessed $4^{th}$ of January 2022.

[6] T. P. Rocha. Numerical and experimental study of wing tip endplates of a formula student car. Master's thesis, Instituto Superior Técnico, October 2020.

[7] J. Katz. *Race Car Aerodynamics: Designing for Speed.* Bentley Publishers, 2003. ISBN 0-8376-0142-8.

[8] C. B. Rasmussen. Race car aerodynamic design and optimization via cfd and the discrete adjoint method. Master's thesis, Aalborg University Esbjerg, June 2018.

[9] Tom Leach, Racingnews365. Mercedes looking into 'interesting' Red Bull design concept. `https://racingnews365.com/mercedes-looking-into-interesting-red-bull-design-concept`. Last accessed $09^{th}$ of March 2022.

[10] The Race, Gary Anderson. What 2022-style F1 ground effect looks like. `https://the-race.com/formula-1/gary-anderson-what-2022-style-f1-ground-effect-looks-like/`. Last accessed $09^{th}$ of March 2022.

[11] G. Abranted. Red Bull - F1 2011 Jerez Test Day 2. `https://www.flickr.com/photos/slitz/5437022653/`. Last accessed $1^{st}$ of February 2022.

[12] P. Soliman, M. Martins, and A. Schommer. Formula SAE Aerodynamics: Design process with focus on drivability. September 2015. doi: 10.4271/2015-36-0359.

[13] J. Iljaž, L. Škerget, M. Štrakl, and J. Marn. Optimization of sae formula rear wing. *Strojniški vestnik - Journal of Mechanical Engineering*, 62(5):263–272, 2016. ISSN 0039-2480. doi: 10.5545/sv-jme.2016.3240.

[14] AMZ Racing Website. Home page. `https://electric.amzracing.ch/`. Last accessed $9^{th}$ of February 2022.

[15] W. Toet. Aerodynamics and aerodynamic research in Formula 1. *The Aeronautical Journal (1968)*, 117(1187):1–26, 2013. doi: 10.1017/S0001924000007739.

[16] F1Technical, Steven De Groote. McLaren opts against racing new rear wing endplates. `https://www.f1technical.net/development/20908/mclaren-opts-against-racing-new-rear-wing-endplates`. Last accessed $9^{th}$ of February 2022.

[17] P. Doddegowda, A. L. Bychkovsky, and A. R. George. Use of computational fluid dynamics for the design of formula sae race car aerodynamics. *SAE Technical Paper*, 2006(01-0807): 10, 2006.

[18] Y. Zhiyin. Large-eddy simulation: Past, present and the future. *Chinese Journal of Aeronautics*, 28(1):11–24, 2015. ISSN 1000-9361. doi: 10.1016/j.cja.2014.12.007.

[19] C. Fureby. ILES and LES of Complex Engineering Turbulent Flows. *Journal of Fluids Engineering*, 129(12):1514–1523, 06 2007. ISSN 0098-2202. doi: 10.1115/1.2801370.

[20] S. Savadatti, C. Nair, and V. Gopalakrishnan. Turbulence models and model closure coefficients sensitivity of nascar racecar rans cfd aerodynamic predictions. In *SAE Technical Paper*, volume 2017, page 10. SAE International, 2017.

[21] D. C. Wilcox. Formulation of the k-w turbulence model revisited. *AIAA Journal*, 46(11): 2823–2838, 2008. doi: 10.2514/1.36541.

[22] W. Jones and B. Launder. The prediction of laminarization with a two-equation model of turbulence. *International Journal of Heat and Mass Transfer*, 15(2):301–314, 1972. ISSN 0017-9310. doi: 10.1016/0017-9310(72)90076-2.

[23] R. H. Bush, T. S. Chyczewski, K. Duraisamy, B. Eisfeld, C. L. Rumsey, and B. R. Smith. Recommendations for future efforts in rans modeling and simulation. In *AIAA Scitech 2019 Forum*, page 0317. American Institute of Aeronautics and Astronautics, 2019.

[24] A. Stefanescu. *RANS Turbulence Modelling for Motorsport Applications*. PhD thesis, University of Manchester, August 2018.

[25] J. B. Barlow, W. H. Rae, and A. Pope. *Low-Speed Wind Tunnel Testing*. John Wiley & Sons, 3 edition, 1999.

[26] R. Weingart. On-track testing as a validation method of computational fluid dynamic simulations of a formula sae vehicle. Master's thesis, University of Kansas, 2015.

[27] I. Preda, D. Covaciu, and G. Ciolan. Coast down test – theoretical and experimental approach. October 2010. doi: 10.13140/RG.2.1.4048.5925.

[28] B. Steinfurth, S. Feldhus, A. Berthold, and F. Haucke. Aerodynamic behavior of formula student open-wheel race car model with regard to head restraint/rear wing interaction. In *WCX World Congress Experience*. SAE International, April 2018.

[29] J. R. M. Pacheco. Wind tunnel testing of a complete formula student vehicle. Master's thesis, Instituto Superior Técnico, June 2022.

[30] M. M. Carreira. Aero map of a formula student prototype. Master's thesis, Instituto Superior Técnico, June 2022.

[31] D. L. Brayshaw and M. F. Harrison. A quasi steady state approach to race car lap simulation in order to understand the effects of racing line and centre of gravity location. *Proceedings of the Institution of Mechanical Engineers, Part D: Journal of Automobile Engineering*, 219 (6):725–739, 2005. doi: 10.1243/095440705X11211.

[32] B. Siegler, A. Deakin, and D. Crolla. Lap time simulation: Comparison of steady state, quasi- static and transient racing car cornering strategies. *SAE transactions*, 109:2575–2581, 2000.

[33] A. Rucco, G. Notarstefano, and J. Hauser. Optimal control based dynamics exploration of a rigid car with longitudinal load transfer. *IEEE Transactions on Control Systems Technology*, 22(3):1070–1077, 2014. doi: 10.1109/TCST.2013.2272402.

[34] J. D. J. Anderson. *Aircraft Performance and Design*. Cambridge: WCB/McGraw-Hill, 1999. ISBN 0-07-116010-8.

[35] International Organization for Standardization. Road vehicles — vehicle dynamics and road-holding ability — vocabulary. *ISO 8855:2011(en)*, 2011. URL `https://www.iso.org/standard/51180.html`.

# Appendix A

# Calibration load cases

| Load Case | Iteration | Fx [N] | Fy [N] | Fz [N] | Mx [Nm] | My [Nm] | Mz [Nm] |
|---|---|---|---|---|---|---|---|
| 1 Fx- | 0 | 0.00 | 0.00 | -8.29 | 0.00 | 0.00 | 0.00 |
| | 1 | -1.00 | 0.00 | -8.29 | 0.00 | 0.00 | 0.00 |
| | 2 | -11.00 | 0.00 | -8.29 | 0.00 | 0.00 | 0.00 |
| | 3 | -21.00 | 0.00 | -8.29 | 0.00 | 0.00 | 0.00 |
| | 4 | -31.00 | 0.00 | -8.29 | 0.00 | 0.00 | 0.00 |
| | 5 | -41.00 | 0.00 | -8.29 | 0.00 | 0.00 | 0.00 |
| | 6 | -51.00 | 0.00 | -8.29 | 0.00 | 0.00 | 0.00 |
| | 7 | -61.00 | 0.00 | -8.29 | 0.00 | 0.00 | 0.00 |
| | 8 | -71.00 | 0.00 | -8.29 | 0.00 | 0.00 | 0.00 |
| | 9 | -81.00 | 0.00 | -8.29 | 0.00 | 0.00 | 0.00 |
| 2 Fz- | 0 | 0.00 | 0.00 | -8.29 | 0.00 | 0.00 | 0.00 |
| | 1 | 0.00 | 0.00 | -10.29 | 0.00 | 0.00 | 0.00 |
| | 2 | 0.00 | 0.00 | -30.29 | 0.00 | 0.00 | 0.00 |
| | 3 | 0.00 | 0.00 | -50.29 | 0.00 | 0.00 | 0.00 |
| | 4 | 0.00 | 0.00 | -70.29 | 0.00 | 0.00 | 0.00 |
| | 5 | 0.00 | 0.00 | -90.29 | 0.00 | 0.00 | 0.00 |
| | 6 | 0.00 | 0.00 | -110.29 | 0.00 | 0.00 | 0.00 |
| | 7 | 0.00 | 0.00 | -130.29 | 0.00 | 0.00 | 0.00 |
| | 8 | 0.00 | 0.00 | -150.29 | 0.00 | 0.00 | 0.00 |
| | 9 | 0.00 | 0.00 | -170.29 | 0.00 | 0.00 | 0.00 |
| | 10 | 0.00 | 0.00 | -190.29 | 0.00 | 0.00 | 0.00 |
| | 11 | 0.00 | 0.00 | -210.29 | 0.00 | 0.00 | 0.00 |
| | 12 | 0.00 | 0.00 | -230.29 | 0.00 | 0.00 | 0.00 |
| 3 Fy+ | 0 | 0.00 | 0.00 | -8.29 | 0.00 | 0.00 | 0.00 |
| | 0.5 | 0.00 | 1.00 | -8.29 | 0.00 | 0.00 | 0.00 |
| | 1 | 0.00 | 6.00 | -8.29 | 0.00 | 0.00 | 0.00 |
| | 2 | 0.00 | 11.00 | -8.29 | 0.00 | 0.00 | 0.00 |
| | 3 | 0.00 | 21.00 | -8.29 | 0.00 | 0.00 | 0.00 |
| | 4 | 0.00 | 31.00 | -8.29 | 0.00 | 0.00 | 0.00 |
| 4 My- | 0 | 0.00 | 0.00 | -8.29 | 0.00 | 0.00 | 0.00 |
| | 0.5 | 0.00 | 0.00 | -8.29 | 0.00 | -0.24 | 0.00 |
| | 1 | 0.00 | 0.00 | -8.29 | 0.00 | -2.64 | 0.00 |
| | 2 | 0.00 | 0.00 | -8.29 | 0.00 | -5.04 | 0.00 |
| | 3 | 0.00 | 0.00 | -8.29 | 0.00 | -7.44 | 0.00 |
| | 4 | 0.00 | 0.00 | -8.29 | 0.00 | -12.24 | 0.00 |
| | 5 | 0.00 | 0.00 | -8.29 | 0.00 | -17.04 | 0.00 |
| 5 Mx+ | 0 | 0.00 | 0.00 | -8.29 | 0.00 | 0.00 | 0.00 |
| | 0.5 | 0.00 | 0.00 | -8.29 | 0.24 | 0.00 | 0.00 |
| | 1 | 0.00 | 0.00 | -8.29 | 1.44 | 0.00 | 0.00 |
| | 2 | 0.00 | 0.00 | -8.29 | 3.84 | 0.00 | 0.00 |
| | 3 | 0.00 | 0.00 | -8.29 | 6.24 | 0.00 | 0.00 |
| | 4 | 0.00 | 0.00 | -8.29 | 8.64 | 0.00 | 0.00 |
| | 5 | 0.00 | 0.00 | -8.29 | 11.04 | 0.00 | 0.00 |
| 6 Mx- | 0 | 0.00 | 0.00 | -8.29 | 0.00 | 0.00 | 0.00 |
| | 0.5 | 0.00 | 0.00 | -8.29 | -0.24 | 0.00 | 0.00 |
| | 1 | 0.00 | 0.00 | -8.29 | -1.44 | 0.00 | 0.00 |
| | 2 | 0.00 | 0.00 | -8.29 | -3.84 | 0.00 | 0.00 |
| | 3 | 0.00 | 0.00 | -8.29 | -6.24 | 0.00 | 0.00 |
| | 4 | 0.00 | 0.00 | -8.29 | -8.64 | 0.00 | 0.00 |
| | 5 | 0.00 | 0.00 | -8.29 | -11.04 | 0.00 | 0.00 |
| 7 Mz+ | 0 | 0.00 | 0.00 | -8.29 | 0.00 | 0.00 | 0.00 |
| | 0.5 | 0.00 | 0.00 | -8.29 | 0.00 | 0.00 | 0.14 |
| | 1 | 0.00 | 0.00 | -8.29 | 0.00 | 0.00 | 1.54 |
| | 2 | 0.00 | 0.00 | -8.29 | 0.00 | 0.00 | 2.94 |
| | 3 | 0.00 | 0.00 | -8.29 | 0.00 | 0.00 | 4.34 |
| | 4 | 0.00 | 0.00 | -8.29 | 0.00 | 0.00 | 5.74 |
| | 5 | 0.00 | 0.00 | -8.29 | 0.00 | 0.00 | 7.14 |

Figure A.1: Table with pure force and moments calibration

| Load Case | Iteration | Fx [N] | Fy [N] | Fz [N] | Mx [Nm] | My [Nm] | Mz [Nm] |
|---|---|---|---|---|---|---|---|
| 8 Fx-Fz- | 0 | 0.00 | 0.00 | -8.29 | 0.00 | 0.00 | 0.00 |
| | 0.5 | -5.00 | 0.00 | -10.29 | 0.00 | 0.00 | 0.00 |
| | 1 | -15.00 | 0.00 | -30.29 | 0.00 | 0.00 | 0.00 |
| | 2 | -15.00 | 0.00 | -50.29 | 0.00 | 0.00 | 0.00 |
| | 3 | -25.00 | 0.00 | -70.29 | 0.00 | 0.00 | 0.00 |
| | 4 | -25.00 | 0.00 | -90.29 | 0.00 | 0.00 | 0.00 |
| | 5 | -35.00 | 0.00 | -110.29 | 0.00 | 0.00 | 0.00 |
| | 6 | -35.00 | 0.00 | -130.29 | 0.00 | 0.00 | 0.00 |
| | 7 | -45.00 | 0.00 | -150.29 | 0.00 | 0.00 | 0.00 |
| | 8 | -45.00 | 0.00 | -170.29 | 0.00 | 0.00 | 0.00 |
| | 9 | -55.00 | 0.00 | -190.29 | 0.00 | 0.00 | 0.00 |
| | 10 | -55.00 | 0.00 | -210.29 | 0.00 | 0.00 | 0.00 |
| 9 Fx-My- | 0 | 0.00 | 0.00 | -8.29 | 0.00 | 0.00 | 0.00 |
| | 0.5 | -1.00 | 0.00 | -8.29 | 0.00 | -1.20 | 0.00 |
| | 1 | -11.00 | 0.00 | -8.29 | 0.00 | -3.60 | 0.00 |
| | 2 | -21.00 | 0.00 | -8.29 | 0.00 | -6.00 | 0.00 |
| | 3 | -31.00 | 0.00 | -8.29 | 0.00 | -8.40 | 0.00 |
| | 4 | -41.00 | 0.00 | -8.29 | 0.00 | -13.20 | 0.00 |
| | 5 | -51.00 | 0.00 | -8.29 | 0.00 | -18.00 | 0.00 |
| | 6 | -71.00 | 0.00 | -8.29 | 0.00 | -22.80 | 0.00 |
| 10 Fz-My- | 0 | 0.00 | 0.00 | -8.29 | 0.00 | 0.00 | 0.00 |
| | 0.5 | 0.00 | 0.00 | -14.29 | 0.00 | -0.15 | 0.00 |
| | 1 | 0.00 | 0.00 | -34.29 | 0.00 | -0.65 | 0.00 |
| | 2 | 0.00 | 0.00 | -54.29 | 0.00 | -1.15 | 0.00 |
| | 3 | 0.00 | 0.00 | -74.29 | 0.00 | -1.65 | 0.00 |
| | 4 | 0.00 | 0.00 | -104.29 | 0.00 | -2.40 | 0.00 |
| | 5 | 0.00 | 0.00 | -134.29 | 0.00 | -3.15 | 0.00 |
| | 6 | 0.00 | 0.00 | -164.29 | 0.00 | -3.90 | 0.00 |
| | 7 | 0.00 | 0.00 | -194.29 | 0.00 | -4.65 | 0.00 |
| | 8 | 0.00 | 0.00 | -214.29 | 0.00 | -5.40 | 0.00 |
| 11 Fx-Fz-My- | 0 | 0.00 | 0.00 | -8.29 | 0.00 | 0.00 | 0.00 |
| | 0.5 | 1.00 | 0.00 | -14.29 | 0.00 | -0.15 | 0.00 |
| | 1 | 11.00 | 0.00 | -34.29 | 0.00 | -0.65 | 0.00 |
| | 2 | 11.00 | 0.00 | -54.29 | 0.00 | -1.15 | 0.00 |
| | 3 | 21.00 | 0.00 | -74.29 | 0.00 | -1.65 | 0.00 |
| | 4 | 21.00 | 0.00 | -104.29 | 0.00 | -2.40 | 0.00 |
| | 5 | 31.00 | 0.00 | -134.29 | 0.00 | -3.15 | 0.00 |
| | 6 | 41.00 | 0.00 | -164.29 | 0.00 | -3.90 | 0.00 |
| | 7 | 51.00 | 0.00 | -194.29 | 0.00 | -4.65 | 0.00 |
| | 8 | 71.00 | 0.00 | -214.29 | 0.00 | -5.40 | 0.00 |
| 12 Fz-Mx+ | 0 | 0.00 | 0.00 | -8.29 | 0.00 | 0.00 | 0.00 |
| | 0.5 | 0.00 | 0.00 | -13.29 | 0.60 | 0.00 | 0.00 |
| | 1 | 0.00 | 0.00 | -23.29 | 1.80 | 0.00 | 0.00 |
| | 2 | 0.00 | 0.00 | -33.29 | 3.00 | 0.00 | 0.00 |
| | 3 | 0.00 | 0.00 | -43.29 | 4.20 | 0.00 | 0.00 |
| | 4 | 0.00 | 0.00 | -53.29 | 5.40 | 0.00 | 0.00 |
| | 5 | 0.00 | 0.00 | -63.29 | 6.60 | 0.00 | 0.00 |
| | 6 | 0.00 | 0.00 | -83.29 | 9.00 | 0.00 | 0.00 |
| 13 Fz-Mx- | 0 | 0.00 | 0.00 | -8.29 | 0.00 | 0.00 | 0.00 |
| | 0.5 | 0.00 | 0.00 | -13.29 | -0.60 | 0.00 | 0.00 |
| | 1 | 0.00 | 0.00 | -23.29 | -1.80 | 0.00 | 0.00 |
| | 2 | 0.00 | 0.00 | -33.29 | -3.00 | 0.00 | 0.00 |
| | 3 | 0.00 | 0.00 | -43.29 | -4.20 | 0.00 | 0.00 |
| | 4 | 0.00 | 0.00 | -53.29 | -5.40 | 0.00 | 0.00 |
| | 5 | 0.00 | 0.00 | -63.29 | -6.60 | 0.00 | 0.00 |
| | 6 | 0.00 | 0.00 | -83.29 | -9.00 | 0.00 | 0.00 |

Figure A.2: Table with combined force and moments calibration

# Appendix B

# Flow visualization - Additional cases

## B.1 2° Yaw

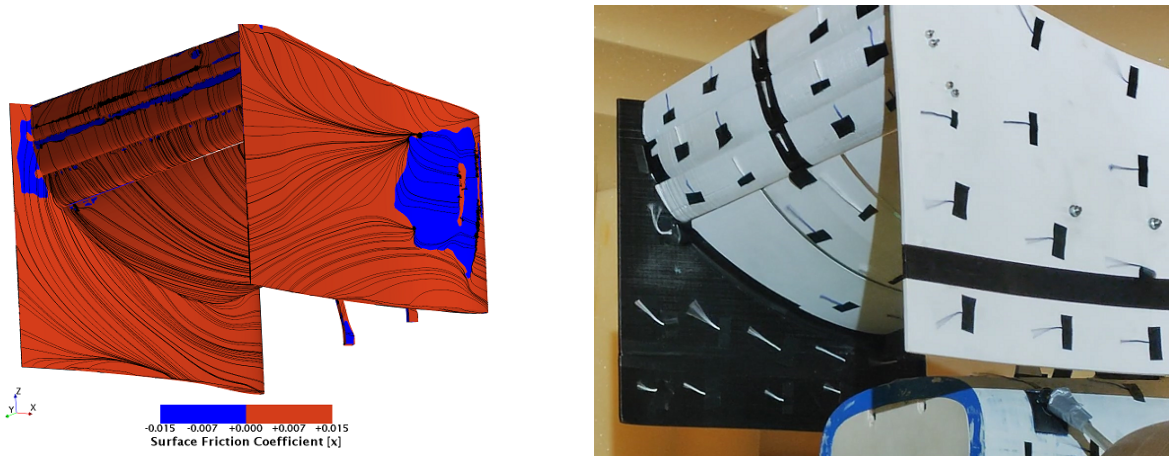


(a) CFD (b) EFD

Figure B.1: Flow visualization of the suction side of the rear wing at $Yaw = 2°$.

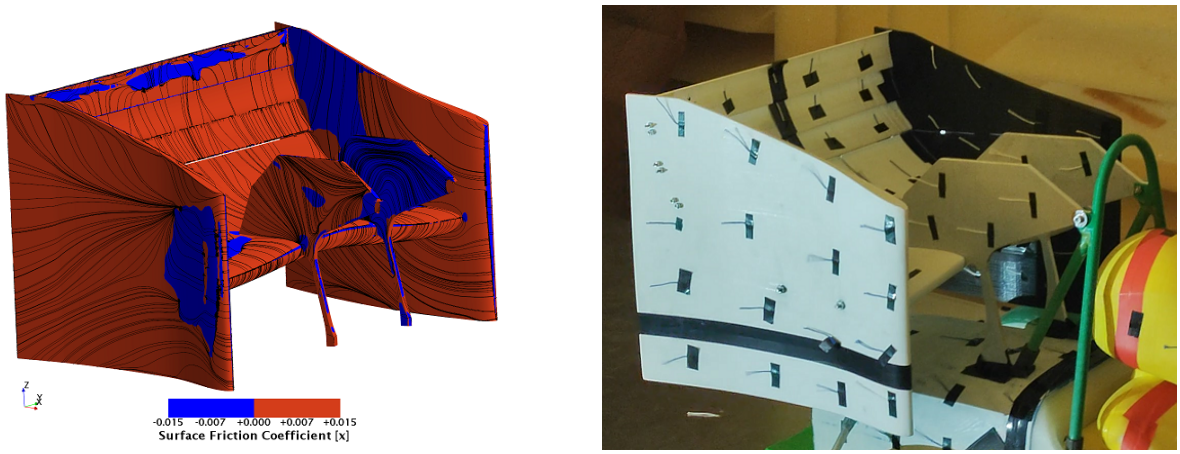


(a) CFD (b) EFD

Figure B.2: Flow visualization of the pressure side of the rear wing at $Yaw = 2°$.

## B.2 4° Yaw

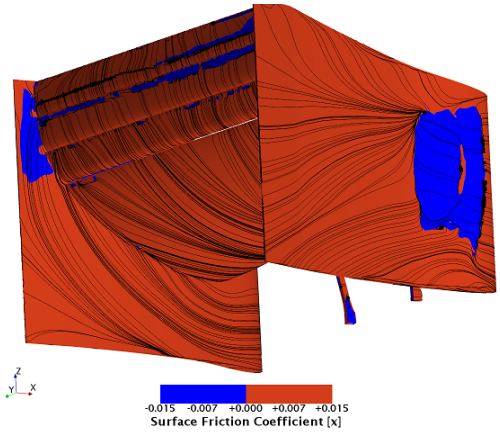


(a) CFD

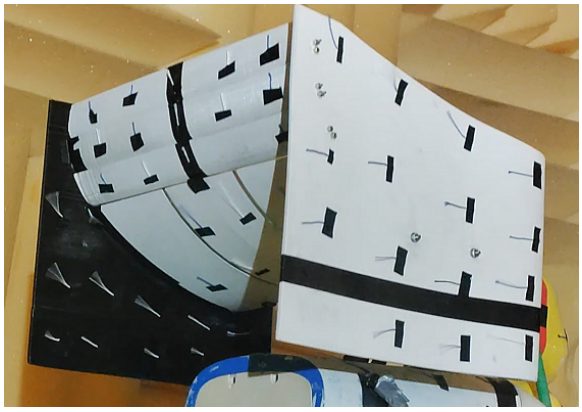

(b) EFD

Figure B.3: Flow visualization of the suction side of the rear wing at $Yaw = 4°$.

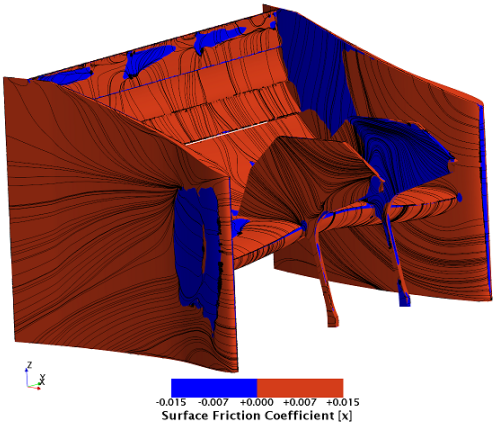


(a) CFD

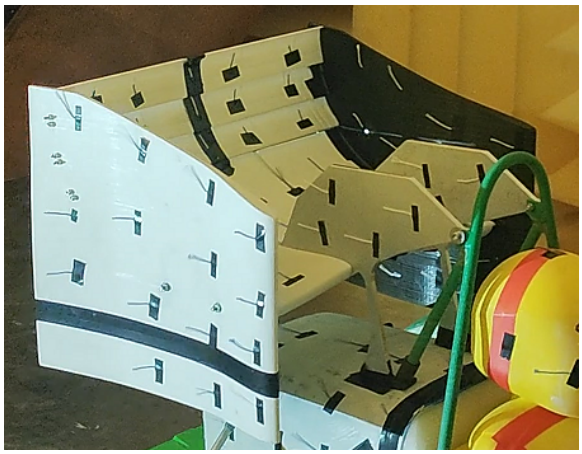

(b) EFD

Figure B.4: Flow visualization of the pressure side of the rear wing at $Yaw = 4°$.

## B.3 6° Yaw

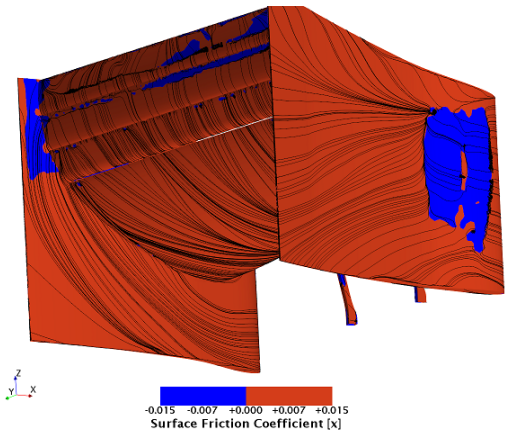


(a) CFD

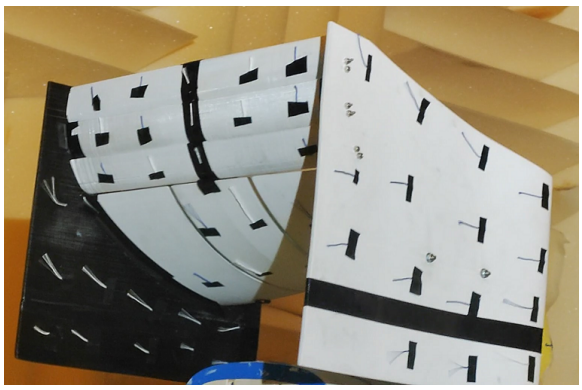

(b) EFD

Figure B.5: Flow visualization of the suction side of the rear wing at $Yaw = 6°$.

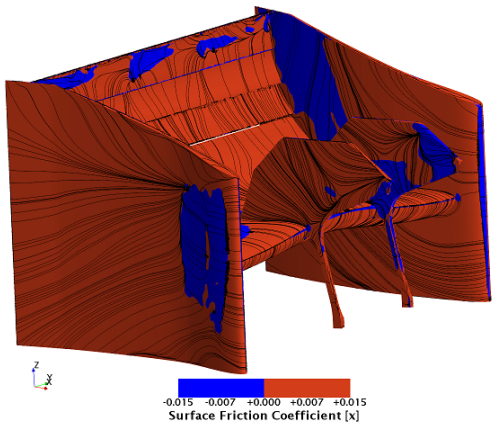


(a) CFD

(b) EFD

Figure B.6: Flow visualization of the pressure side of the rear wing at $Yaw = 6°$.

## B.4 8° Yaw

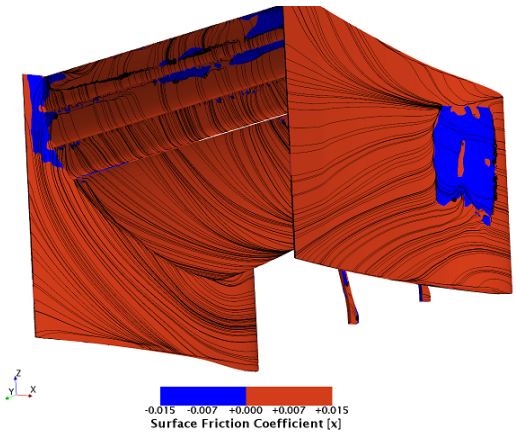


(a) CFD

(b) EFD

Figure B.7: Flow visualization of the suction side of the rear wing at $Yaw = 8°$.

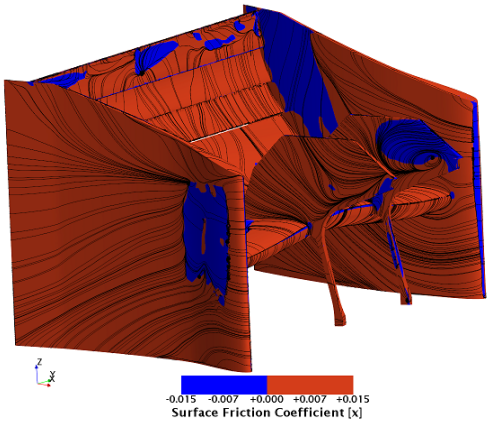


(a) CFD

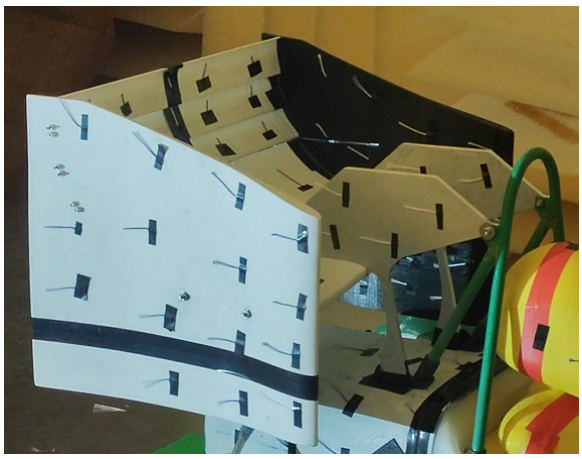

(b) EFD

Figure B.8: Flow visualization of the pressure side of the rear wing at $Yaw = 8°$.